Thesis advisor

Robert J. Wood

Author

Rebecca Krone Kramer

Soft Active Materials for Actuation, Sensing, and Electronics

Abstract

Future generations of robots, electronics, and assistive medical devices will include systems that are soft and elastically deformable, allowing them to adapt their morphology in unstructured environments. This will require soft active materials for actuation, circuitry, and sensing of deformation and contact pressure. The emerging field of soft robotics utilizes these soft active materials to mimic the inherent compliance of natural soft-bodied systems. As the elasticity of robot components increases, the challenges for functionality revert to basic questions of fabrication, materials, and design - whereas such aspects are far more developed for traditional rigid-bodied systems. This thesis will highlight preliminary materials and designs that address the need for soft actuators and sensors, as well as emerging fabrication techniques for manufacturing stretchable circuits and devices based on liquid-embedded elastomers.

Contents

Acknowledgments

First and foremost, I would like to thank my advisor, Professor Robert J. Wood, as the work presented in this thesis would not have been possible without his continual support, encouragement, and inspiration. It has been a privilege to work with him, and in result I have enjoyed an extremely positive and intellectually fulfilling experience as a graduate student. I would also like to thank the many faculty that I have had the pleasure of working with throughout my doctoral research, including Professor Howard Stone, Professor Joanna Aizenberg, Professor Katia Bertoldi, Professor David Weitz, Professor Robert Howe, and Professor George Whitesides, for their counsel and research support.

I wish to thank the members of the Harvard Microrobotics Lab, many of whom have served as fantastic collaborators and friends. A special thanks is due to Professor Carmel Majidi (CMU), Professor Jamie Paik (EPFL), and Dr. Yong-Lae Park, for their contributions to my research and knowledge. I would also like to thank my fellow lab-mates for the positive impact they have had on my research and graduate experience: Andrew Baisch, Pakpong Chirarattananon, Pierre-Emile Duhamel, Ben Finio, Katie Hoffman, Kevin Ma, Pratheev Sreetharan, Zhi Ern Teoh, Peter Whitney, Dr. Sawyer Fuller, Dr. Kevin Galloway, Dr. Frank Hammond, Dr. Mike Karpelson, Dr. Mirko Kovac, Dr. Nestor Perez-Arancibia, Dr. Ranjana Sahai, Dr. Mike Tolley, Dr. Mike Wehner, and many others. Other collaborators that I would like to thank include Dr. Robert Shepherd, Dr. Philseok Kim, and Dr. Jiandi Wan. In addition, I wish to thank Michael Smith and Hetchen Ehrenfeld for administrative and research support.

Finally, this dissertation would not have been possible without the loving support

of my family and friends. I want to thank my parents, Rita and Jeffrey Kramer, who have provided me with education and opportunity, as well as unconditional love, empathy, and inspiration. My brother, Matthew Kramer, has always been there for me with an unfailing sense of humor and a dose of perspective as I have gone through the ups and downs of the research process. And lastly, I wish to thank my boyfriend and best friend, Alex Bottiglio, who has stood by my side during these difficult months leading to my defense with unwavering love, support and an endless supply of pep-talks.

My doctoral research experience has been extremely rewarding, and would not have been possible without the academic and emotional support of those mentioned here, among many others. Once again, I thank all of my advisors, mentors, collaborators, family and friends for the contributions they have made to this dissertation. I hope this thesis does justice to the incredible wealth of knowledge and kindness that I have experienced on this academic journey.

To my parents

Rita Krone Kramer & Jeffrey Alan Kramer

who have loved and supported me unconditionally.

Chapter 1

Introduction and Motivations

1.1 Grand Challenges in Soft Robotics

Soft robotics is a new paradigm in robotics, which aims to mimic the inherent compliance of natural soft-bodied systems. For example, the octopus can squeeze its body through holes and cracks that are very small in comparison to the length scales of the octopus (Figure 1.1).

Traditionally, robots are thought of as precise and fast, in part due to structural

Figure 1.1: An octopus escapes a box through a one-inch hole [1].

rigidity, high force & torque actuators, and a large variety of available motors, sensors, and electronics. Creating soft-bodied robots requires a new class of *soft active materials*, with embedded electrical or mechanical functionality. Components made from soft active materials should maintain the functionality of traditional components (sensors, actuators, and electronics), yet without any rigid elements (characteristic modulus on the order of 100kPa to 1MPa). The work presented in this thesis addresses these grand challenges through common themes such as micro-fluidics, soft materials, and new composite micro-fabrication methods.

1.2 Prior Work

There have been several interesting approaches to soft robotics, including pneumatically actuated robots that exploit materials of various stiffnesses to control motion [2, 3], 3D-printed flexible robots actuated by shape memory alloy [4, 5], devices based on dielectric elastomers [6], devices based on particle jamming [7], and many more. Viable soft actuation technologies based on soft active materials include electroactive polymers [8], conducting polymers [9], and polymer gels [10]. Soft sensor and circuit approaches have included embedded carbon nanotubes in an elastomer matrix [11], conductive fabric [12], conductive micro-particle filler [13], and patterned conductive thin films on flexible substrates [14]. Given the broad range of soft active materials, a more in-depth literature review is provided throughout the chapters of this thesis.

1.3 Thesis Outline

This thesis has five major components that focus on different forms and uses of soft active materials.

Chapter 2 focuses on humidity-triggered swelling of a hydrogel unimorph for applications in soft actuation. The proposed unimorph is modeled with a quasi-static analytical model. In addition, finite element modeling is used to predict configurations for a free-swelling hydrogel and a hydrogel unimorph in both 2D and 3D.

Chapter 3 moves on to the challenge of soft sensing, beginning with a hyperelastic pressure transducer that is fabricated by embedding silicone rubber with microchannels of conductive liquid. Pressing the surface of the elastomer will deform the cross-section of underlying channels and change their electrical resistance. Change in electrical resistance is measured as a function of the magnitude and area of the surface pressure as well as the cross-sectional geometry. The pressure sensor is demonstrated via application to a hyperelastic tactile keypad. In addition, the fabrication techniques introduced in this chapter provide a framework for fabrication that is built upon in the remaining thesis chapters.

Chapter 4 discusses a hyperelastic liquid-embedded elastomer curvature sensor that uses a novel non-differential mechanism. In contrast to conventional curvature sensors that use a strain sensor offset from the neutral axis, this elastomer-based solution allows for curvature sensing directly on the bending plane. Analytical solutions serve as predictive models for the curvature sensor behavior. Building from this analysis, both strain and curvature sensing designs are applied to a joint angle proprioceptive sensor. Given the complex sensing and boundary conditions, calibration

techniques for bend angle sensors are introduced and employed to test to accuracy of the sensors. These sensors represent the first use of liquid-embedded elastomer electronics to monitor human or robotic motion.

In Chapter 5, liquid-embedded elastomers are proposed as stretchable power circuits. A conductive liquid-filled elastomer circuit is compared directly to a copper-mesh circuit embedded in a thermoplastic polyurethane. Each circuit design is applied to a two-tile folding module actuated by a shape memory alloy actuator. The circuits are compared in terms of strain to failure, mass, actuation time constant, power consumption, and change in trace resistivity.

Chapter 6 examines the liquid-embedded elastomer fabrication process and the geometric and scale limitations that the previously used process introduces. A new fabrication method, based on selective wetting of gallium-indium alloys, is proposed. Interfacial processes between gallium-indium alloys and surfaces of various composition and texture are exploited to encapsulate conductive liquid in an elastomer sheet. This work will serve as a foundation for future liquid-embedded-elastomer electronics that require miniaturized, densely-packed, or isolated features.

Finally, Chapter 7 discusses the impact of this research on future work with liquid-embedded elastomer electronics. Potential research topics in soft and stretchable electronics are reviewed, and the outlook for future development of soft robotics is discussed.

1.4 Contributions

This thesis presents several key building blocks for soft sensors and electronics based on liquid-embedded elastomer devices. The work described here serves as platforms for wearable computing, human-robot interaction, and sensory skins through the follow contributions:

1. The design and experimental verification of soft, hyperelastic pressure and curvature sensors using a liquid-embedded elastomer approach. Because the sensors are inherently soft and stretchable, they can be integrated with human and robotic systems without restricting motion of the host. Tuning the geometry of the sensors allows for a large range of sensitivities.

2. Characterization of liquid-embedded elastomers as stretchable power circuits, using metrics such as strain to failure, actuation time constant, power consumption, and change in trace resistivity.

3. The development of a manufacturing technique using selective wetting of gallium-indium alloys for liquid-embedded elastomer electronics. This process alleviates many former limitations for soft electronic devices, and enables soft electromechanical functionality.

1.5 Citations to Previously Published Work

Much of the work presented in this dissertation has been published in the following:

Yong-Lae Park, Carmel Majidi, **Rebecca Kramer**, Phillipe Berard, and Robert J. Wood. "Hyperelastic Pressure Sensing with a Liquid-Embedded Elastomer." Journal of Micromechanics and Microengineering, 2010, v. 20 pp. 125029.

Rebecca K. Kramer, Carmel Majidi, Robert J. Wood. "Wearable Tactile Keypad with Stretchable Artificial Skin." IEEE Int. Conference on Robotics and Automation, Shanghai China, May, 2010.

Carmel Majidi, **Rebecca Kramer**, Robert J. Wood. "Non-Differential Elastomer Curvature Sensor for Softer-than-Skin Electronics." Smart Materials and Structures, 2011, v. 20 pp. 105017.

Jamie K. Paik, **Rebecca K. Kramer**, Robert J. Wood. "Stretchable Circuits and Sensors for Robotic Origami." IEEE Int. Conference on Intelligent Robotics and Systems, San Francisco USA, 2010.

Rebecca K. Kramer, Carmel Majidi, Ranjana Sahai, Robert J. Wood. "Soft Curvature Sensors for Joint Angle Proprioception." IEEE Int. Conference on Intelligent Robotics and Systems, San Francisco USA, 2010.

Chapter 2

Humidity Induced Bending of a Hydrogel Unimorph

A hydrogel is a cross-linked polymer network that can be designed to change volume in response to a wide range of stimuli, including humidity. This chapter aims to model the behavior a composite hydrogel and non-swelling gel unimorph for applications in soft actuation. A finite element model (ABAQUS) of a partially constrained hydrogel film is implemented via a user-defined subroutine with three material parameter inputs. The model presented here estimates the free-energy of a hydrogel and the corresponding displacements and stresses of the polymer network. Numerical examples have shown that the model behaves intuitively and the effects of parameter inputs on swelling behavior have been studied. In the future, comparisons against empirically determined bilayer hydrogel actuator conformations will be used to the tune the parameters of the model.

2.1 Background on Soft Actuation

Soft actuators aim to mimic the inherent compliance of natural muscle as well as combine additional functionality, such as proprioception and active impedance control. By implementing soft active materials, or clever geometries of more rigid components that yield compliancy [15], it is possible to create entire mechanical systems that are soft and compliant. Soft mechanical systems present several advantages over traditional rigid-body systems. Non-compliant systems are limited in mobility and geometric configuration by factors such as segment length and component size. An ideal soft and flexible system combines all the necessary mechanisms into a single, tunable material that has an infinite number of degrees of freedom and may undergo drastic and reversible deformations.

Recent research has imitated biological actuators to develop polymer chemistry processes that translate chemical energy into mechanical motion [16]. Advancements in these 'artificial muscle' technologies may yield development of soft actuators capable of vast conformational changes. Material realization of soft actuation has been suggested via technologies such as gel-solid phase transitions, electro- and magneto-rheological materials, geometric transitions, and reversible chemical and/or particle association and dissociation [17]. Static and dynamic bending of soft materials has been demonstrated using pneumatics [18, 19], shape memory materials [20, 21], conducting polymers [22], and dielectric elastomers [23]. A wide range of adaptive responsive materials have been explored, the majority of which involve polymer gels [24]. Hydrogels are just one class of polymer gel, and have been designed to respond to stimuli including temperature [25, 26, 27, 28, 29], light [30], pH [31, 32, 33, 34],

electric field [35, 36, 10], ion strength [37, 34], and humidity [38, 39].

Previous experiments have tended towards an assessment of hydrogel swelling capabilities for applications in microfluidics, drug delivery, optics, and adaptive architecture. Only recently, however, have hydrogels been considered for actuation in soft robotics. Multi-functional structural materials and robots that may adapt to their environment, harvest energy and mechanically reconfigure require both tools and integration. Little attention has been paid to material compatibility with hydrogels and system integration in which local and controlled hydrogel swelling is achievable.

2.2 Previous Experimental Work with Hydrogels

Toyoichi Tanaka first discovered that a small change in environment can cause a hydrogel to abruptly swell to many times its original size, or collapse into a compact mass, in 1975. Since then, researchers have studied the physical, chemical, and mechanical properties of hydrogels, including various mixture ratios, "ingredients", curing techniques, and system integration with other polymeric materials.

Much work on hydrogel actuation has been done regarding microvalves for active microfluidic flow control [40]. In many of these studies, a hydrogel is positioned directly in a microfluidic channel, encapsulated by the channel floor and ceiling, such that when the hydrogel swells it forms a blockade [31, 37, 33]. Hydrogels are fabricated within channels using liquid-phase photo-polymerization techniques [35, 32]. As Beebe, et al., showed in 2000, fast polymerization of hydrogels within microchannels can be achieved in a variety of shapes by employment of a photolithographic mask. Two-dimensional shut-off microvalves consisting of hydrogel "jackets" around prefab-

ricated posts allow for uniform swelling in all directions in a microchannel without any concern that the hydrogel may move, as it is held in place by the posts [33]. This eliminates any need for chemical bonding steps between materials. A thermally responsive PDMS composite with embedded hydrogel microspheres was also developed for microfluidic applications [28]. The expansion of the composite material was shown to be an irreversible volume increase of up to 270%, which was implemented as an irreversible microvalve.

Improved response times of hydrogels, on the order of milliseconds, have been reported with a reduction in length scales [32, 25]. In 2007, a responsive hydrogel scaffold consisting of submicron-sized microgel particles was reported on [25], which successfully yielded a structure that swells and de-swells at a macroscopic level in much shorter times as compared to a bulk polymer gel.

In 1995, Hu, et al. [26] achieved the modulation of a temperature-sensitive and acetone concentration-sensitive hydrogel bimorph by interpenetration of part of one polymer gel network with another polymer gel. A layered structure fabricated from N-isoproplyacrylamide (NIPA) gel was grafted to an acrylamide (PAAM) gel. When actuated by both acetone concentration and temperature, the structure bent into a nearly perfectly circular configuration. Further structures were developed that bend or curl into a variety of interesting shapes such as a letter of the alphabet, a spiral, a square, or a fish. A similar system was reported on by Osada, et al., in 1992 [10]. In this system, a gel network is anionic, and positively charged surfactant molecules can bind to its surface, inducing local shrinkage by decreasing the difference in osmostic pressure within the gel. Using an electric field directs surfactant binding selectively

to one side of the gel, and reversing the direction of the electric field directs binding to the opposite side. The ends result is electrically driven gel curvature.

In 2005, a light-induced shape-memory polymer was reported on by Lendlein, et al. [30], in which polymers containing cinnamic groups were shown to deform by ultraviolet light illumination. Hydrogel applications in optics are another recent development. In 2006 it was reported by Dong, et al., that a ring shaped stimuli-responsive hydrogel could be used as a container for a liquid droplet, or a micro-lens [41]. By actuating the hydrogel, small changes to the liquid droplet would adjust the focal length of the micro-lens. Finally, soft reconfigurable hybrid surfaces [24, 39] have been developed in which polymer micro-bristles are embedded in a hydrogel layer. The dynamic and reversible passive bending of the micro-posts is achieved by active volume-phase transition of a humidity-sensitive hydrogel layer.

2.3 Hydrogels and Swelling Kinetics

A hydrogel is generally defined as a polymer network in which water is the dispersion medium. Prominent hydrogel properties include absorbency, flexibility and tunability. Hydrogels have the unique properties of both a solid and liquid - elastic deformation results from strong chemical crosslinking between long-chained polymers that are water insoluble, and viscous migration results from weak physical association between polymer and solvent molecules [42]. Many hydrogels undergo reversible, discontinuous volume changes in response to changes in the balance between repulsive intermolecular forces, which act to expand the polymer network, and attractive forces, which act to contract it [16]. Reversible gel swelling on the order of 1000%

has been observed [43].

Hydrogels also present some significant limitations, mostly related to considerable disorder at the molecular level and the complex diffusion processes inside the gel, which have been shown to be a collective diffusion process of the entire network. Hence, the kinetics of swelling and contraction are diffusion limited and proportional to the square of the dominant linear dimension of the gel [16].

A clear understanding of how a hydrogel swells has not yet been achieved in the literature. The common assumption of free swelling is rarely valid due to mechanical loads, geometric constraints and variation in chemical potential of the solvent, which may markedly influence the swelling process. From theory of elasticity [44, 45, 46], it known that an isotropic polymer gel network has a free energy, $\mathbf{F}$, which is a function of the gel body's strain tensor, and that this free energy is at a minimum when the system is at equilibrium with its environment. During swelling, a non-equilibrium state, the body of a hydrogel is changing in both volume and shape. In general, if the volume of a body is unchanged by deformation and only its shape is being altered, the deformation is referred to as pure shear. In the opposite case, if the deformation causes a change in the volume of a body but no change in its shape (each volume element of the body retains its shape), the deformation is called hydrostatic expansion. Hydrogel swelling can be represented as the sum of pure shear and hydrostatic expansion. Hence, the total free energy of the body is found in the sum of the free energy of the un-deformed body (a constant term, $\mathbf{F_0}$) and the elastic free energy of deformation, which is comprised of the bulk energy (related to volume change and characterized by the bulk modulus) and the shear energy (related to

deformation of the polymer network and characterized by the shear modulus).

A model of the swelling of gel networks was first proposed by Tanaka, Hocker, and Benedek in 1973 [42]. This model draws from principles of elasticity, fluids and dynamic light scattering to define a displacement vector, $u(r,t)$, representing the displacement of a point in the polymer network from its final equilibrium location after the gel is fully swollen. By this definition, $u = 0$ at $t = \infty$.

Consider the deformation of a unit cube of a polymer network with density, ρ. The forces acting on the cube are hydrostatic expansion stresses due to volumetric expansion, and shear force due to friction between the polymer network and the solvent. The net force on the cube is expressed as the difference of the divergence of the stress tensor and the shear force. The shear force is determined by analogy with Stokes' formula for the shear force caused by fluid flow over a sphere of radius R, $F_{shear} = -6\pi R\eta\frac{\partial u}{\partial t}$. Hence, the shear force on the unit cube is estimated by $f\frac{\partial}{\partial t}u$, where f is the friction constant and $\frac{\partial u}{\partial t}$ is the relative velocity between the polymer network and the solvent, respectively. The sum of all forces on the unit cube is equal to $\rho\frac{\partial^2}{\partial t^2}u$, and the displacement vector obeys the following linear equation:

$$\rho\frac{\partial^2}{\partial t^2}u = \nabla\cdot\sigma - f\frac{\partial}{\partial t}u. \tag{2.1}$$

Because there is essentially no relative motion between the polymer network and the solvent (this statement will be expanded on later), it is assumed in most polymer gel models that $\rho\frac{\partial^2}{\partial t^2}u = 0$ [47, 48]. Therefore,

$$f\frac{\partial u}{\partial t} = \nabla\cdot\sigma. \tag{2.2}$$

In small deformation theory for any elastic body, the stress tensor is given by [44]

$$\sigma_{ik} = K\nabla \cdot u\delta_{ik} + 2\mu\left(u_{ik} - \frac{1}{3}\nabla \cdot u\delta_{ik}\right), \tag{2.3}$$

where K and μ are the bulk modulus and shear modulus of the polymer network, respectively. The subscript ik denotes the force along the k-axis on a unit plane perpendicular to the i-axis [47]. The first term of the stress tensor denotes the stress produced by volume change to the unit cube (or more generally, polymer network); the second term represents the stress caused by shear deformation of the unit cube (polymer network) [44]. The strain tensor is given by [44]

$$u_{ik} = \frac{1}{2}\left(\frac{\partial u_k}{\partial u_i} + \frac{\partial u_i}{\partial u_k}\right). \tag{2.4}$$

These expressions give the change in length of an element when the body is deformed. Through substitution, an equation of motion is found [48]:

$$\frac{\partial u}{\partial t} = D_0\nabla^2 u + \frac{K + \frac{\mu}{3}}{f}\nabla \times (\nabla \times u), \tag{2.5}$$

where $D_0 = \frac{K+\frac{4\mu}{3}}{f}$ is the collective diffusion constant.

Further implementation of the model proposed by Tanaka, Hocker, and Benedek [42] to spherically-shaped gels was used to describe free swelling kinetics [47] under the assumption that the shear modulus of the gel is negligible compared with the osmotic bulk modulus. However, as first pointed out by Li and Tanaka in 1990 [48], this assumption is insufficient for gels with a non-spherical shape. By assuming that the shear modulus is equal to zero, the equation of motion becomes a pure diffusion

equation. However, experimental results indicate that the swelling and shrinking processes of a polymer gel are not purely diffusive. For example, in the case of a long, cylindrical polymer gel undergoing free swelling, the relative change of the diameter and the length are the same [48]. This indicates that the shear modulus of the network plays a significant role during swelling and shrinking processes and cannot be neglected.

The kinetics of swelling of arbitrary shapes can be understood by considering the free swelling of a long cylindrical gel. As pointed out by Li and Tanaka [48], free swelling can be thought of as the combination of two consecutive processes: pure diffusion followed by shear relaxation. When a long cylindrical gel is brought into contact with a solvent, a purely diffusive process causes the diameter to swell, but the change in length of the cylinder is negligible. During this process, the structure of the polymer network is "stretched" to accommodate the change in diameter, which causes a build-up of shear energy in the system. In response, the length of the cylinder will increase and the diameter will decrease to minimize the shear energy with the volume of the body kept constant. The key feature of shear relaxation is that the volume of the body and of each individual unit of the polymer network remains constant during this instantaneous change. In consequence, there is no relative motion between the polymer network and the solvent, and therefore no friction is created in this process.

The shear energy of a gel of arbitrary shape is [48]:

$$F_{shear} = \mu \int_V \left[\left(u_{xx} - \frac{T}{3} \right)^2 + \left(u_{yy} - \frac{T}{3} \right)^2 + \left(u_{zz} - \frac{T}{3} \right)^2 \right] dV, \tag{2.6}$$

where μ is the shear modulus, u_{xx}, u_{yy}, and u_{zz} are the principal strains of the strain

tensor, respectively, and $T = (u_{xx} + u_{yy} + u_{zz})$ is the trace of the strain tensor, i.e. the sum of the principal strains. Because the shear relaxation process is instantaneous and continuous, it is assumed that $\delta F_{shear} = 0$. For the singular case of a spherical polymer gel, the process of shear relaxation does not occur because the minimum energy shape of a sphere is automatically maintained through uniform diffusion-induced swelling [48].

Several recent comments in the literature have expressed the necessity of including motion of the solvent in polymer gel models of non-spherical shape [49, 50]. The solvent motion is thought to aid the system in minimizing the total free energy, and can be accounted for in the equation of motion derived by Tanaka, Hocker and Benedek by adding a term for the velocity of the solvent, $\frac{\partial w}{\partial t}$, such that

$$\frac{\partial u}{\partial t} = \frac{\partial w}{\partial t} + \frac{1}{f}\nabla \cdot \sigma. \tag{2.7}$$

It is clear that the kinetics of swelling presents a difficult set of mathematical relations that cannot be easily solved without simplification or numerical methods. The literature [42, 47, 48, 51, 49, 52, 50, 53, 54] presents the governing equations and direct solutions given by the theories discussed above for a polymeric sphere, cylinder, and disk. In each case, the direct solution yields little intuition for the how a swelling and shrinking polymer gel of arbitrary shape will behave.

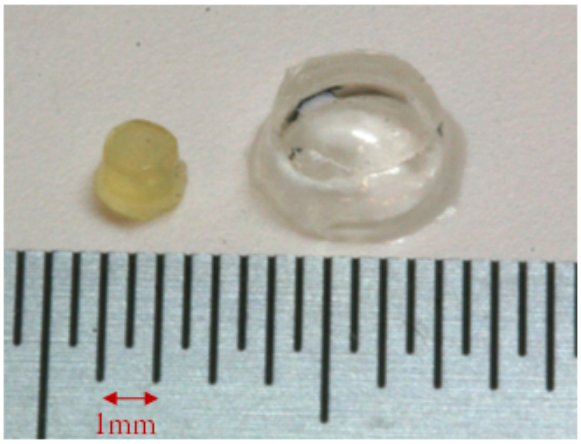

(a)

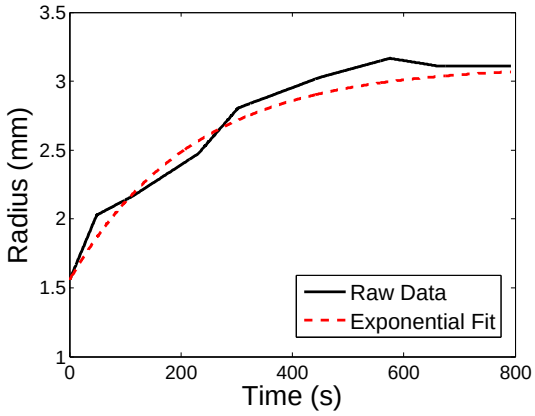

(b)

Figure 2.1: (a) The swollen configuration for an actual free swelling PEG hydrogel. The swelling ratio of the hydrogel is $Q = 11$. (b) Swelling radius of the cylindrical hydrogel pictured in (a) as a function of time. The data is fit to an exponential curve of the form $R(t) = R_0(1 - e^{-t/\tau}) + R_0$, where $\tau = 220$ seconds. In general, τ is dependent on both the geometry and the diffusion coefficient of the gel.

2.4 Composite Poly(ethylene glycol)-based Hydrogel and Poly(dimethylsiloxane) Actuators

This study serves the specific application of modeling composite hydrogel and poly(dimethylsiloxane) (PDMS) actuators. Poly(ethylene glycol) (PEG)-based hydrogel is one of the polymers that swells in water and most organic solvents and has shown impressive swelling capability in the literature [55, 56]. A hydrogel/PDMS composite device can be reversibly actuated by exposure to changes in humidity. In air, a unimorph PEG/PDMS device will remain flat. When it is brought into contact with a solvent, the hydrogel imbibes the solvent and swells, causing volumetric expansion of the hydrogel layer and forcing the inactive elastomeric PDMS layer to bend.

Table 2.1: Example hydrogel unimorph geometries and corresponding curvatures.

	Sample 1	**Sample 2**
Length	7 cm	5.7 cm
Width	1.3 cm	1.1 cm
PEG Thickness	0.35 mm	0.35 mm
PDMS Thickness	1.25 mm	0.95 mm
Curvature	4.08 cm	3.75 cm

The geometry of the unbent unimorph and the ratio of hydrogel thickness to PDMS thickness each play a key role in the final curvature of the actuator. Table 2.1 gives the geometries of two hydrogel unimorphs and the resulting curvatures after submersion in deionized water. For unimorph assemblies with similar length:width aspect ratios, the role of the PEG:PDMS thickness ratio can be further analyzed. The curvature results given in Table 2.1 confirm the intuitive notion that for a constant hydrogel thickness, a reduction in PDMS thickness yields lessened stiffness and increased curvature.

The hydrogel mixture is 20% (by volume) poly(ethylene glycol)(PEG) with a molecular weight of 2000. This powder hydrogel base is combined with 79% PBS buffer solution and 1% photo-initiator (Irgacure 2959, Ciba). Figure 2.1(a) denotes the swelling ratio of the final volume to the initial volume, $Q = V_f/V_i$, for the experimental hydrogel is equal to approximately 11. Adjustments to the volume ratios may yield different swelling results. It has been found empirically that an increase in percent PEG by volume yields additional stiffness to the polymerized hydrogel. In contrast, an increase in molecular weight of the PEG yields a decrease in hydrogel stiffness.

A pliable self-folding actuator, driven by environmental changes in humidity, is

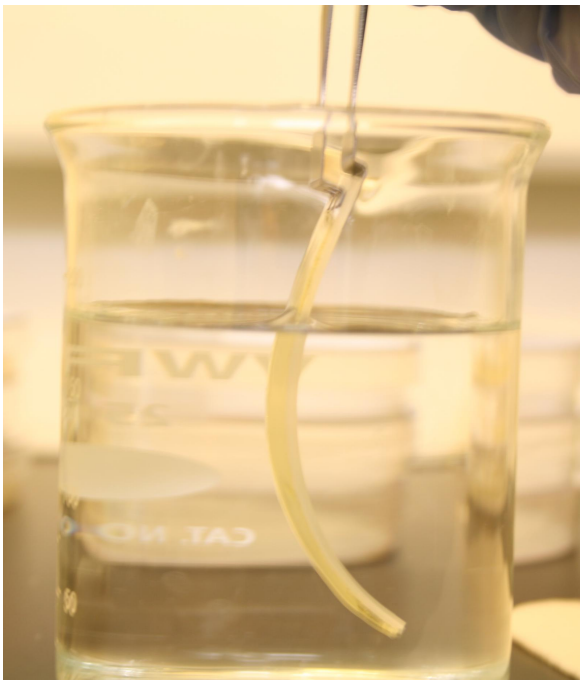

Figure 2.2: A film of PEG diacrylate-based hydrogel grafted to a PDMS film via a PGMA anchoring layer. The length of the composite hydrogel actuator is approximately 6cm.

fabricated from layers of cross-linked PEG diacrylate -based hydrogel and PDMS (Sylgard 184, 10:1 base:curing agent ratio by weight). Polyglycidyl methacrylate (PGMA) dissolved into a mixture of MEK (2-butanone) : DMSO (dimethyl sulfoxide) (10:1 v:v), when applied to a thin plasma-treated PDMS substrate, forms a surface layer that is rich in reactive glycidyl groups allowing for the grafting of acrylate-based hydrogels [24]. A layer of PEG (MW 2000) gel grafted to the substrate via PGMA is formed by photo-initiated crosslinking of PEG-diacrylate and the glycidyl anchoring groups.

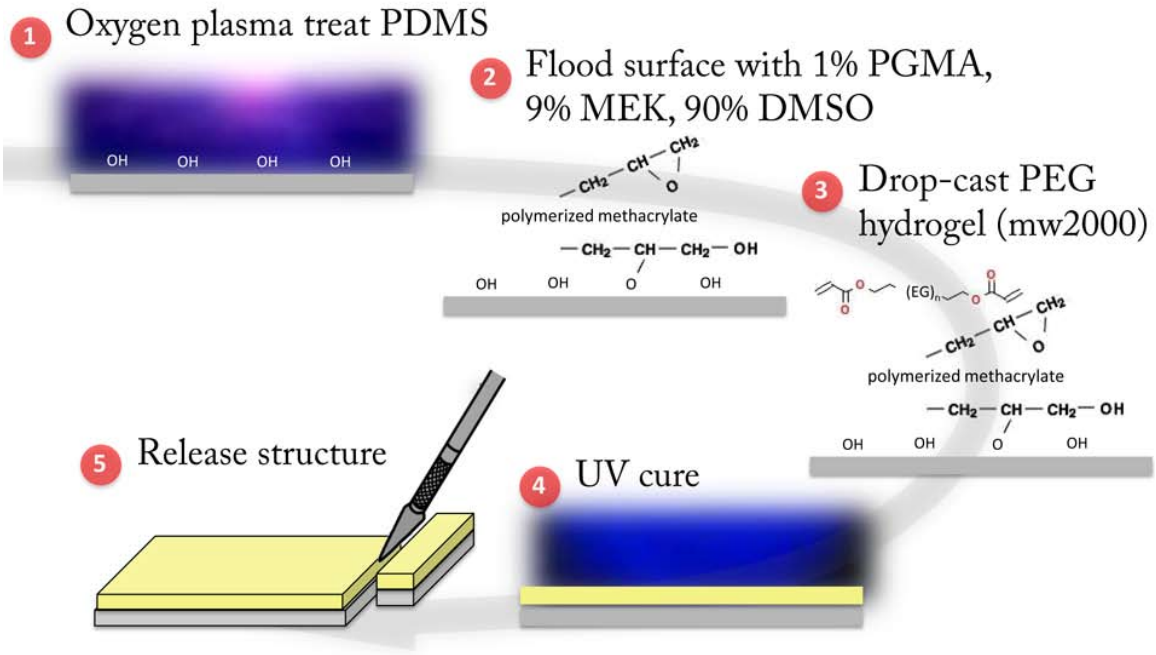

Figure 2.3: Chemical fabrication process for hydrogel actuators.

2.4.1 Bonding Process

Sufficient bonding between poly(ethylene glycol)(PEG) diacrylate- based hydrogel and poly(dimethylsiloxane)(PDMS) is achieved through surface modification to the PDMS substrate, as shown in Figure 2.2. The fabrication process can be seen in Figure 2.3.

A PDMS surface is oxygen-plasma treated for approximately 30 seconds (65 watts), which yields hydroxyl groups at the surface. The sample is then immersed (or the surface is flooded) with a 1% glycidyl methacrylate based polymer (PGMA) solution (1% PGMA, 9% methyl ethyl ketone (MEK), 90% dimethyl sulfoxide (DMSO)) for a minimum of 15 minutes. DMSO was chosen as the base solvent because solvents such as MEK and chloroform caused non-uniform swelling to the PDMS surface in ex-

periments. DMSO is among the organic solvents that does not cause notable swelling of PDMS [57]. During immersion in PGMA solution, the polymerized methacrylate bonds to the PDMS substrate via the gylcidyl groups, while also leaving exposed glycidyl groups.

After the resting step in PGMA solution, the surface is rinsed thoroughly with DMSO and dried with a nitrogen stream to remove any excess solution and prepare the surface for the next binding step. PEG-diacrylate hydrogel is then drop-casted onto the surface, allowing the exposed glycidyl groups on the surface to bond to the acrylate groups in the hydrogel solution. Finally, UV-exposure enables complete curing of the hydrogel and completes the grafting process.

Several other composite hydrogel grafting processes have been reported in the literature, such as electrochemically driven deposition [58], direct hydrogel growth [59], interpenetration of polymer networks [36, 26], and silane vapor deposition for surface modification [55]. In each of these methods, there is very little capability to pattern hydrogels. The key advantage of the chemical PDMS surface modification described above is that the hydrogel is deposited in the liquid phase and must be photo-cured as the final synthesis step. The use of a mask allows for direct photo-patterning of liquid phase hydrogel for simple discriminatory patterning and fabrication [32], which is favorable for actuator design.

2.5 Quasi-Static Stress Analysis

A hydrogel unimorph may be considered as a composite beam composed of two layers: (1) an elastomer of width w, thickness H_e, length L_e, and elastic modulus

E_e and (2) a hydrogel of width w, thickness $H_h = H_h(t)$, length $L_h = L_h(t)$, and elastic modulus $E_h = E_h(t)$. Here, t denotes time and it is assumed that at time $t = 0$, $L_h(0) = L_e$. However, as the hydrogel swells, its natural length becomes $L_h(t) = L_e e^{t/\tau}$. The time constant τ is related to the swelling kinetics and should be treated as a system parameter. Similarly, both the thickness H_h and elastic modulus E_h will also change by prescribed amounts as the hydrogel swells.

For convenience, we select a reference configuration in which the hydrogel is compressed to have the same length as the elastomer. This means that the hydrogel has a residual strain $\epsilon_0 = (L_h - L_e)/L_e$. The elastomer and hydrogel obey the following constitutive laws:

$$\sigma_e = E_e\epsilon \qquad \text{and} \qquad \sigma_h = E_h(\epsilon - \epsilon_0), \tag{2.8}$$

where σ is the internal stress acting along the lengthwise direction. That is, in the reference configuration, the hydrogel is under compressive residual stress.

Geometric compatibility requires that ϵ has the form

$$\epsilon = \alpha - \kappa z. \tag{2.9}$$

The coordinate z is defined as zero at the interface and positive in the direction of the hydrogel. Therefore, the hydrogel occupies the space $[0, H_h]$ while the elastomer corresponds to $[-H_e, 0]$. The unknown parameter κ corresponds to bending curvature of the composite in the positive z direction (i.e. towards the hydrogel). The neutral axis z_N is defined as the plane in which ϵ is zero, i.e. $z_N = \alpha/\kappa$.

Since there are no external loads, the net stress and moment acting on the cross-section of the composite must be zero:

$$\begin{aligned} \int_{-H_e}^{0} \sigma_e \, \mathrm{d}z + \int_{0}^{H_h} \sigma_h \, \mathrm{d}z = 0 \\ \int_{-H_e}^{0} \sigma_e z \, \mathrm{d}z + \int_{0}^{H_h} \sigma_h z \, \mathrm{d}z = 0. \end{aligned} \tag{2.10}$$

Substituting the expressions for σ and ϵ into the above balance equations and solving for α and κ yields:

$$\begin{aligned} \alpha &= \frac{(4E_e{H_e}^3 + 3E_e{H_e}^2H_h + E_h{H_h}^3)E_hH_h\epsilon_0}{{E_e}^2{H_e}^4 + 4E_eH_eE_h{H_h}^3 + 4E_hH_hE_e{H_e}^3 + {E_h}^2{H_h}^4 + 6E_e{H_e}^2E_h{H_h}^2} \\ \kappa &= -\frac{6E_eH_eE_hH_h\epsilon_0(H_h + H_e)}{{E_e}^2{H_e}^4 + 4E_eH_eE_h{H_h}^3 + 4E_hH_hE_e{H_e}^3 + {E_h}^2{H_h}^4 + 6E_e{H_e}^2E_h{H_h}^2} \end{aligned} \tag{2.11}$$

It is clear from the above solution that the bending curvature is linearly proportional to the residual strain ϵ_0. This, in turn, is linearly proportional to the change $\Delta L_h = L_h(t) - L_h(0)$ in the natural length of the hydrogel as it swells. The curvature also depends on the parameters H_h and E_h, which are expected to change with swelling.

Although derived from the static stress balance, the above solutions are valid for dynamical analysis when the time constants for swelling kinematics (like τ) are much longer than elastic relaxation time constants associated with mechanical damping. In this respect, the solution is quasi-static. This analysis was largely contributed by Professor Carmel Majidi.

2.6 Finite Element Formulation

We now seek to define the deformation of free swelling and geometrically constrained hydrogels by a finite element method implemented in ABAQUS. Note that the work presented here was done in collaboration with Professor Katia Bertoldi. The numerical method is based on a theory developed by Flory and Rehner [60], in which the free-energy function for a gel incorporates the effects of the entropy of stretching the network, the entropy of mixing the network polymers and the solvent molecules, and the enthalpy of mixing. The free-energy of the gel is thus converted to physical deformation by the finite element method, as was demonstrated by Zhang et al. [61].

2.6.1 Material Model

We take thermodynamic equilibrium of the hydrogel to be the steady-state configuration. A material model [61] for a gel with a Flory-Rehner free-energy function is defined by a hyperelastic material subroutine (provided by Dr. Shengqiang Cai) in ABAQUS. According to the kinetics of migration [60], the material deformation is mainly defined by the free-energy function, $W(\mathbf{F}, \mu)$, and the mobility tensor, $M_{KL}(\mathbf{F}, \mu)$. Following Zhang et al. [61], we write the free energy of Flory and Rehner in the form

$$W(\mathbf{F},\mu) = \frac{\mathbf{1}}{\mathbf{2}}\mathbf{NkT}\big[\mathbf{F_{iK}F_{iK}} - \mathbf{3} - \mathbf{2log(detF)}\big] \tag{2.12}$$
$$-\frac{kT}{\nu}\big[(det\mathbf{F}-\mathbf{1})\mathbf{log}(\frac{\mathbf{detF}}{\mathbf{detF}-\mathbf{1}}) + \frac{\chi}{\mathbf{detF}}\big] - \frac{\mu}{\nu}(\mathbf{detF}-\mathbf{1})$$

where N is the number of polymer chains in the gel divided by the volume of the gel in the reference state, kT is the temperature in units of energy, ν is the volume per solvent molecule, and χ is a dimensionless parameter characterizing the enthalpy of mixing. In Equation 2.12, the reference state is taken to be the dry network, for which $\mu \to -\infty$. Similarly, when the environment is in a purely liquid state, the gel is consequently swollen and $\mu = 0$. For the purpose of this study, we take the reference state of the gel to be partially swollen ($-\infty < \mu < 0$). In ABAQUS, temperature is used to represent chemical potential of the solvent. Hence, we define a state variable, $T_{abaqus} = \mu/kT$, such that when the gel is in a completely dry state $T_{abaqus} \to -\infty$ and when the gel is in a completely swollen state $T_{abaqus} = 0$.

There are three material properties of the hydrogel that must be passed to ABAQUS: $N\nu$, χ, and λ_0. The property $N\nu$ is related to the shear modulus of the gel. The dry network has a shear modulus NkT under small-strain conditions, with representative values $NkT = 10^4 - 10^7$ N/m^2. A representative value of the volume per solvent molecule is $\nu = 10^{-28} m^3$. At room temperature, $kT = 4 \times 10^{-21}$ J. Therefore, it can be seen that $kT/\nu = 4 \times 10^7$ Pa, and $N\nu$ has a range of $N\nu = 10^{-4} - 10^{-1}$. The parameter χ is a dimensionless measure of the enthalpy of mixing, with representative values $\chi = 0 - 1.2$, where gels with large swelling ratios tend towards lower values of χ. Lastly, λ_0 is a measure of the initial swelling, which is dependent on the other parameters of the system.

The initial value of chemical potential should agree with the initial swelling, given

as follows:

$$T_{abaqus} = \frac{\mu_0}{kT} = N\nu\big(\frac{1}{\lambda_0} - \frac{1}{det\mathbf{F_0}}\big) + ln\big(1 - \frac{1}{det\mathbf{F_0}}\big) + \frac{1}{det\mathbf{F_0}} + \frac{\chi}{det\mathbf{F_0}^2} \qquad (2.13)$$

where $det\mathbf{F_0} = \lambda_\mathbf{0}^\mathbf{3}$.

This material model outputs the free-energy function and its derivatives. All free-energy densities and stresses given by the model are normalized by kT/ν, and the chemical potential by kT, such that all outputs yield the units of the inputs. Hence, the theory has no intrinsic length scale.

2.6.2 Free Swelling of a Hydrogel

The free swelling of a rectangular shaped hydrogel is studied here. The hydrogel is 10 x 10 x 1 units in volume, composed of 100 equally sized cubic elements, and it is constrained from displacement at one node. For input material parameters set to $N\nu = 10^{-3}$, $\chi = 0.1$, $\lambda_0 = 1.86$ and $T_{abaqus} = -0.01$, the distribution of dimensionless true displacement for the swollen configuration is shown in Figure 2.4. By noting the maximum displacement in the x, y and z directions, respectively, a swelling ratio of the final volume to the initial volume $Q = V_f/V_i$ is obtained. For example, for the chosen parameters resulting in Figure 2.4, the swelling ratio Q is equal to 1.6.

The above method yields information about how the parameters passed to ABAQUS effect the final swollen configuration of the gel. Several parameter combinations have been implemented, and the results are given in Table 2.2. It should be noted that the parameter combinations given in Table 2.2 are listed in order by increasing swelling ratio.

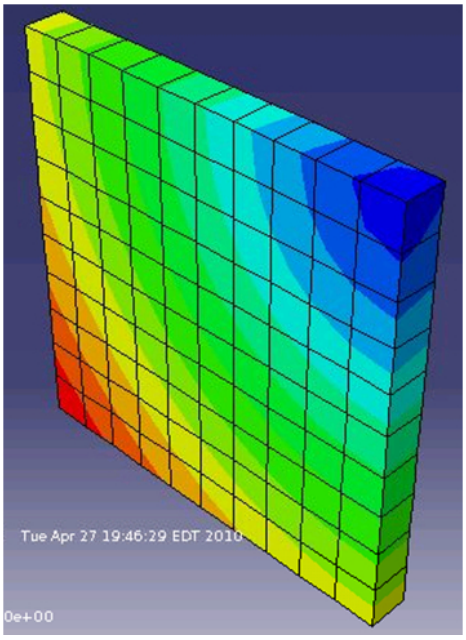

Figure 2.4: The swollen configuration for a free swelling rectangular hydrogel that is spatially fixed at one node. The color scale denotes dimensionless displacement distribution, such that blue indicates small displacements and red indicates large displacements.

Table 2.2: Design parameters of a free swelling hydrogel.

$N\nu$	χ	λ_0	T_{abaqus}	Q
10^{-3}	0.1	1.86	-0.01	1.63
10^{-3}	0.001	1.86	-0.013	1.90
10^{-3}	0	1.86	-0.013	1.90
10^{-3}	0.1	1.5	-0.046	3.25
10^{-4}	0.1	1.86	-0.011	6.05
10^{-3}	0.1	1.01	-2.46	10.66
10^{-3}	0.1	1.0001	-7.01	10.97

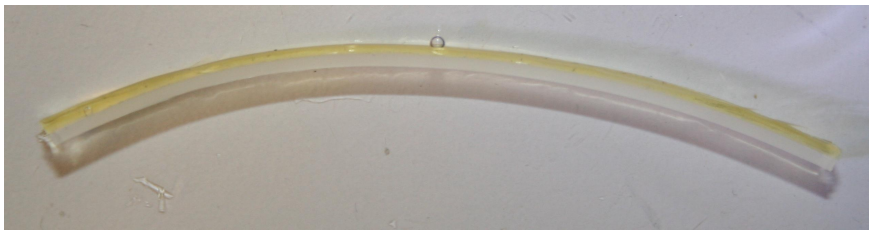

Figure 2.5: PEG-based hydrogel grafted to PDMS acting as an actuator. The width:length ratio is approximately 0.2 and the PEG:PDMS thickness ratio is about 0.3. Complete submersion in deionized water yields a radius of curvature of about 4 cm.

From empirical data (partially shown in Table 2.2), it is determined that increasing the value of λ_0 results in an increased swelling ratio. Similarly, decreasing the value of χ increases the swelling ratio. Note that both λ_0 and χ are bound at a minimum value of zero. It should be noted in Equation 2.13, for $\lambda_0 \leq 0$ the corresponding chemical potential contains imaginary parts. Furthermore, reduction in the value of $N\nu$ results in an increased swelling ratio. For $N\nu > 10^{-3}$, the gel has a swelling ratio of less than one.

2.6.3 Swelling Behavior of a Partially Constrained Hydrogel

Here, a finite element model of a hydrogel unimorph (partially constrained swelling system) is implemented. The method is implemented in ABAQUS via a user-defined subroutine. As described by Zhang et al. [61], a humidity-sensitive hydrogel will deform and exchange solvent molecules with the environment when immersed in a solvent and subjected to external forces. If both the applied forces and chemical potential of the solvent are time-independent, the hydrogel will eventually reach a state of thermodynamic equilibrium, in which the chemical potential of the solvent inside the gel becomes homogeneous and takes the same value as that of the environment.

A hydrogel bonded to a non-swelling gel provides a platform system on which to study the effect of geometric constraints on swelling. The problem is modeled by considering two equally sized gel films (1cm x 4cm x 1mm) that are assumed to be perfectly bonded. The non-swelling gel is defined as a Neo-Hookean hyperelastic solid for which the shear modulus G and bulk modulus B are 1 and 10^5, respectively. The initial chemical potential of the solvent is programmed in ABAQUS as an initial condition temperature, $T_{abaqus} = -0.01$, which is only applied to the elements assigned as hydrogel material. For this analysis, T_{abaqus} increases to zero value, or to the equilibrium fully swollen state, as described in §2.6.1. The analysis considers non-linear geometry.

Both two-dimensional and three-dimensional models are explored. For each case, the input parameters for the material model of the hydrogel are given as $N\nu = 10^{-3}$, $\chi = 0.1$, $\lambda_0 = 1.86$ and $T_{abaqus} = -0.01$.

Figure 2.6 shows the undeformed mesh, deformed mesh, and stress field (von-Mises) for a two-dimensional finite element model of a hydrogel unimorph. It should be noted that the greatest magnitude of stress is concentrated at the center of the non-swelling gel, which is being compressed during swelling. This is intuitive, because the hydrogel layer is in fact not being elongated, but rather is changing in material properties to be at a different equilibrium volume. However, the bonded interface between the gels does cause some stress to build in the hydrogel film.

Figure 2.7 shows the undeformed mesh, deformed mesh, and distribution of dimensionless stress (von-Mises) for a three-dimensional finite element model of a hydrogel unimorph. The three-dimensional model confirms the results of the two-dimensional

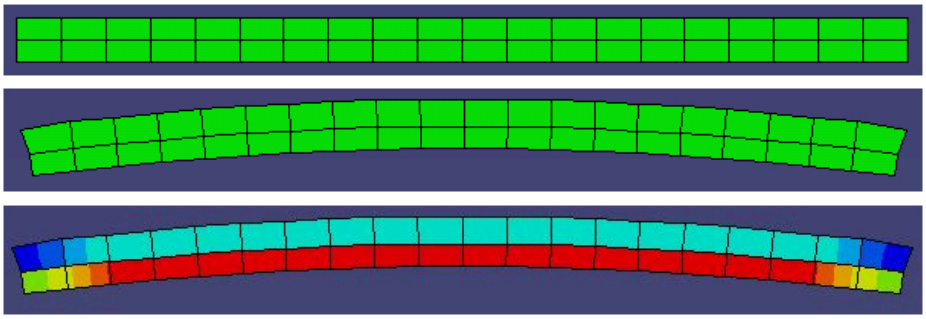

Figure 2.6: Undeformed mesh (a), deformed mesh (b), and stress field (von-Mises) (c) for a two-dimensional finite element model of a hydrogel unimorph. The system is 4cm in length and 2mm in height. Input hydrogel material parameters are $N\nu = 10^{-3}$, $\chi = 0.1$, $\lambda_0 = 1.86$ and $T_{abaqus} = -0.01$, and the swelling ratio of the hydrogel is $Q = 1.6$.

model, yet contributes the realization that increased width of the composite film yields omni-directional bending, as opposed to unidirectional bending.

2.7 Conclusions and Future Work

The ABAQUS finite element model implemented in this study has the potential to yield valuable predictive information about the final configuration of a geometrically constrained swelling hydrogel. The model presented here implements a user-element subroutine to define the important parameters that govern the swelling of a hydrogel.

Numerical examples have shown that this model behaves intuitively. However, simulation results have not yet been experimentally verified. In the future, the model presented here will be compared against empirically determined hydrogel unimorph conformations and used to tune the parameters of the model. For example, varying the thickness of the hydrogel and/or non-swelling gel layer changes the stiffness of the bilayer system and provides a simple set of experiments to which the model may be compared against. In addition, the finite element model should be modified to study

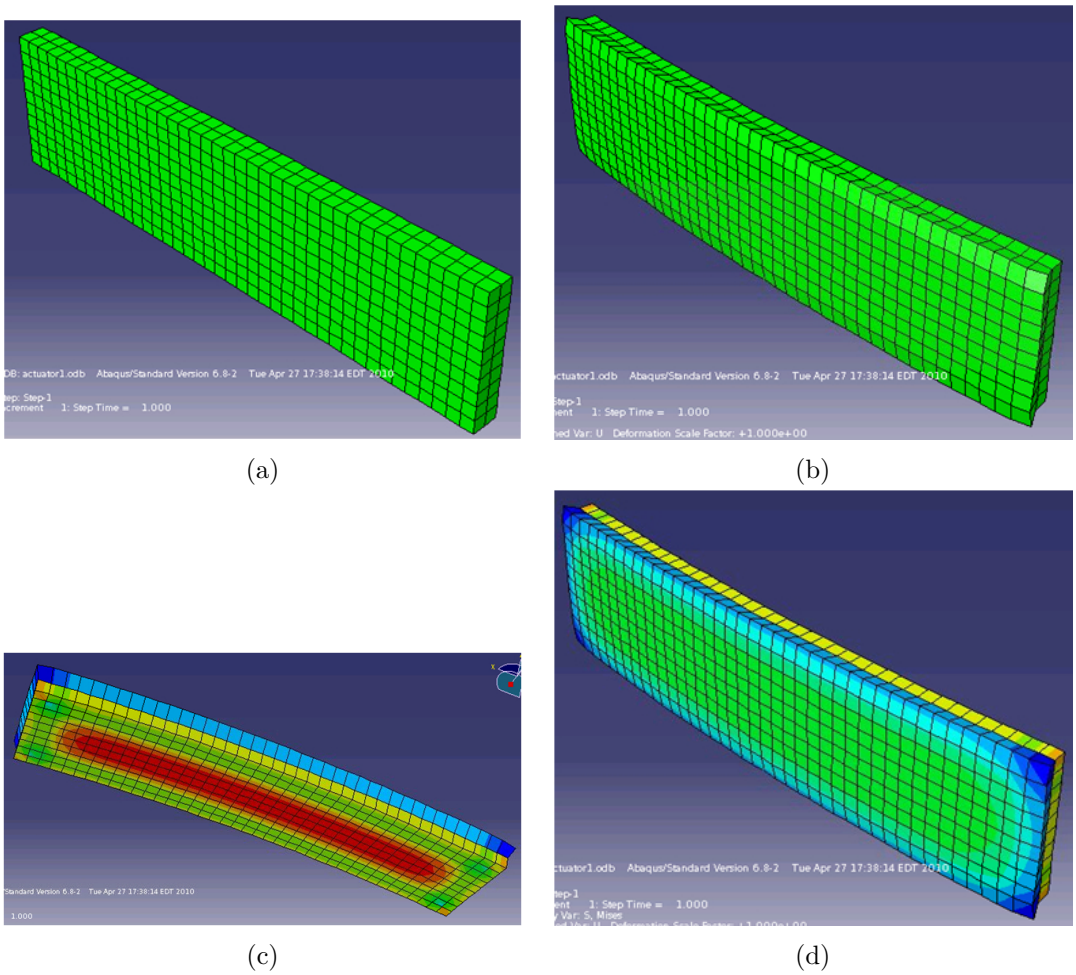

(a) (b)

(c) (d)

Figure 2.7: Undeformed mesh (a), deformed mesh (b), and distribution of dimensionless stress (von-Mises) (c-d) for a three-dimensional finite element model of a hydrogel unimorph. The system is 4cm in length, 1cm in width and 2mm in height. Input hydrogel material parameters are $N\nu = 10^{-3}$, $\chi = 0.1$, $\lambda_0 = 1.86$ and $T_{abaqus} = -0.01$, and the swelling ratio of the hydrogel is $Q = 1.6$.

time-dependence of swelling gels, and applied to more complex configurations to aid in prediction of final configuration, output forces and moments.

Chapter 3

Hyperelastic Pressure Sensing with Liquid-Embedded Elastomers

The previous chapter discussed one possible approach to soft actuation. This chapter will now introduce concepts and designs related to soft sensing. For a novel soft pressure sensor design, this chapter details fabrication and characterization, as well as a demonstrative hyperelastic tactile keypad device composed of a soft pressure sensor array.

3.1 Background on Soft Pressure Sensors

Recent developments in wearable computing [62], as well as flexible pressure sensors and circuits [63, 14], have brought the robotics community closer towards the realization of skin-like tactile sensing. Flexibility and stretchability will significantly expand the scope of applications of sensors, particularly towards wearable sensing for

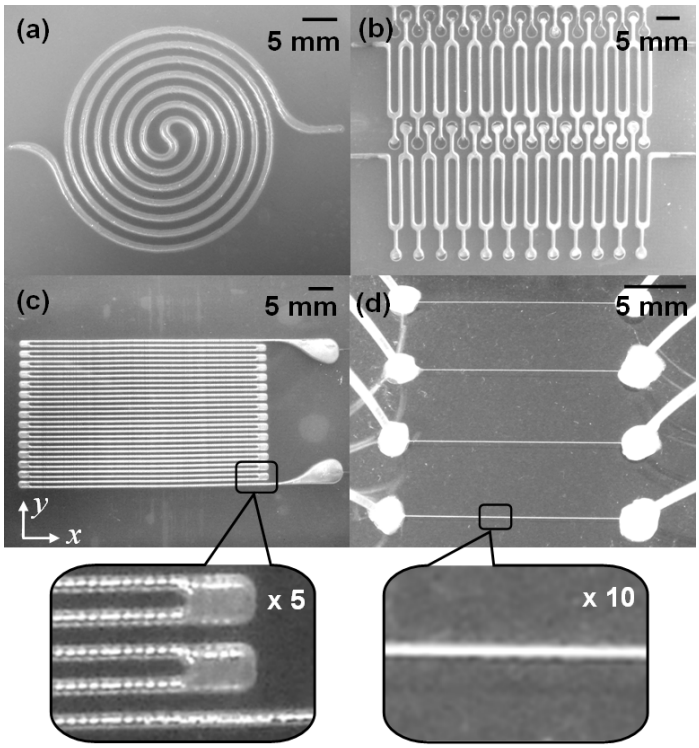

Figure 3.1: Liquid-embedded elastomer pressure and in-plane strain sensors. (a) Spiral shaped channel for pressure sensing only. (b) Serpentine shape channels with reservoirs for increased sensitivity. (c) Strain gauge for both pressure and directional strain sensing. (a,b,c) Silicone rubber (EcoFlex® 0030) embedded with channels of cross-sectional dimensions ($h \times w$) of 1 mm^2, 750 μm^2, and 300 μm^2, respectively. Devices fabricated by Dr. Yong-Lae Park. (d) Embedded PDMS microchannels with 20 μm height and (from top) 25, 30, 35, and 40 μm width are produced with a maskless soft lithography process.

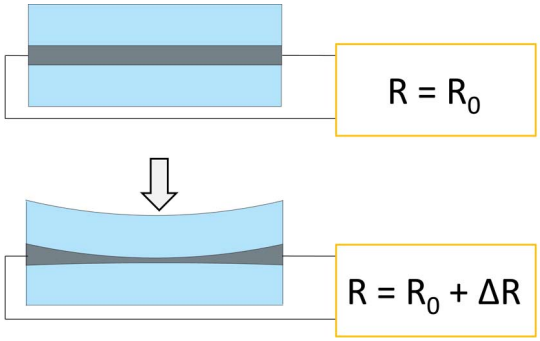

Figure 3.2: Pressing the surface of the elastomer reduces the cross-sectional area of the embedded liquid channel and increases its electrical resistance.

which surfaces are arbitrary and dynamic. Pressure sensors and tactile interfaces for wearable electronics and soft robots must be elastically soft and remain functional when stretched to several times their natural length.

Stretchable capacitive pressure sensors for tactile sensing and humanoid robots have recently been demonstrated with elastic insulator layered between conductive fabric [64, 65, 66] and a silicone rubber sheet embedded with thin gold film [67]. Such sensors also operate by continuously supplying electrostatic charge and measuring the electrostatic induction brought on by surface pressure [68]. Other recent efforts include resistive sensors composed of an elastomer embedded with conductive microparticle filler [69, 70, 71] or an ionic liquid [72].

Various types of highly conductive stretchable materials have been developed for stretchable electronic applications. Many exploit structures such as waves and nets, as in the case of wavy thin metals [73, 74, 75, 76, 77, 78], graphene films [79], and single-walled carbon nanotubes [80]. Stretchable electronics consisting of elastomers embedded with channels of conductive liquid have also been investigated and can operate as a stretchable, mechanically tunable antenna [81] or as strain sensors [82] for measuring stretches of as much as 200%. Liquid conductors eliminate the need for rigid electronics and preserve the natural hyperelasticity of the embedded elastomer, which allows for mechanical durability and stretches as great as 1000%. Thus, this technology offers a vast range of applications for which large deformations and pressures might be sustained.

This chapter introduces a stretchable, softer-than-skin pressure transducer (Figure 3.1) composed of a silicone rubber (EcoFlex® 0030, SmoothOn; PDMS, Dow

Corning) sheet embedded with conductive liquid microchannels of non-toxic eutectic gallium-indium (eGaIn, BASF). Pressing the surface of the elastomer deforms the cross-section of nearby channels and changes their electrical resistance, as illustrated in Figure 3.2. Change in electrical resistance is measured as a function of the magnitude and area of the surface pressure as well as the cross-sectional geometry of the embedded channel.

This design for pressure sensing is adapted from the Whitney strain gauge, which was introduced in 1949 to measure the change in circumferential girth of muscles and limbs [83, 84]. The original Whitney strain gauge was composed of a rubber tube filled with mercury and employed a Wheatstone Bridge to measure the change in electrical resistance of the mercury channel corresponding to stretch. Recently, this principle has been extended to stretchable microelectronics, composed of eGaIn-filled microchannels embedded in polydimethylsiloxane (PDMS) rubber [85]. In this work, it is shown that embedded eGaIn channels can also operate as pressure sensors with 1 kPa resolution and 0-100 kPa range, with contact localization resolution on the order of 100s of microns.

3.2 Fabrication Methods

Soft pressure sensors may be fabricated in several ways, all of which involve a replica molding process. In the following sections, fabrication techniques for molds by which to construct soft structures will be detailed.

3.2.1 3D-Printer-Based Replica Molding

Sensors with channel dimensions greater than 250 μm are shown in Figure 3.1(a-c). These are produced by casting uncured silicone rubber into 3D-printed (Connex 500, Objet Geometries Ltd.) molds. 3D-printing presents a highly convenient approach to mold fabrication, however even current state-of-the-art printers begin to sacrifice feature definition at sub-500 μm length scales.

After casting and degassing, the elastomer is then cured in the molds. Curing conditions depend on the elastomer; as an example, we consider EcoFlex® 0030. After curing in ambient conditions for approximately four hours, the elastomer layers are removed from the molds and bonded together with a thin, uncured layer of elastomer via a process detailed here. To avoid filling the exposed microchannels, the unpatterned elastomer mold is first spin-coated with the thin, uncured layer (1100 rpm for 45 seconds), which is then partially cured for 30 seconds at 60°C in a convection oven. The patterned elastomer mold is then gently bonded to the unpatterned surface. The two elastomer layers (the smooth sheet and the sheet containing the exposed microchannels) are then cured together in ambient conditions for several hours. After the molds are sufficiently bonded together, a syringe is used to fill each channel with eGaIn. Lastly, the ends of the channel are sealed with a final coating of uncured elastomer.

3.2.2 SU-8 Molds with a Maskless Lithography Process

Sensors with channel dimensions less than 250 μm, shown in Figure 3.1(d), may be fabricated by casting liquid-form elastomer onto an SU-8 mold that is patterned

via a maskless lithography process, which combines direct laser writing [86, 87] with soft lithography [88, 89] to produce micron-order feature sizes. Photoresist (SU-8 2050) is spun onto a clean silicon wafer at 500 rpm for 10 seconds (spread), followed by 4000 rpm for 30 seconds (spin). The wafer is then placed on a hot plate at 65°C for 3 minutes and 95°C for 6 minutes. Next, the coated wafer is patterned via direct-write laser exposure using a diode-pumped solid-state (DPSS) 355 nm laser micromachining system. The system was previously calibrated to expose a 20 μm thick SU-8 coating to produce channels with 25 to 1000 μm width and $\geq$50 μm spacing. The wafer is post-baked on a hot plate at 65°C for 1 minute and 95°C for 6 minutes, and consequently developed for several minutes in SU-8 developer.

3.2.3 SU-8 Molds with Standard Photolithography

SU-8 photoresist may be patterned onto silicon wafers by means of a standard photolithography process. A mask is used to determine the lateral geometry of molded structures, and choice of photoresist and spin rate determine the subsequent depth of the features. Although other recipes may be used to obtain a similar result, one exact method is given here. Photoresist (SU-8 2010) is spun onto a clean wafer at 500 rpm for 5 seconds (spread), followed by 1000 rpm for 33 seconds (spin). The wafer is then placed on a hot plate at 65 °C for 1 minute and 95 °C for 3 minutes. The wafer is then exposed under a mask with a collimated UV-light source, and post-baked for 4.5 minutes at 95 °C. Finally, the mold is developed in SU-8 developer. Recipes for SU-8 photolithography can be found on the Microchem Corp webpage [1].

[1] http://www.microchem.com

3.2.4 Molds with Laser-Cut Adhesive Films

Microchannel molds may also be fabricated by patterning kapton film on glass. Adhesive-backed polyimide film (McMaster-Carr) is adhered to a clean glass slide (Electron Microscopy Sciences) and the outline of the desired pattern is transferred to the film via a laser micro-machining system (VersaLaser, Universal Laser Systems). After patterning, excess film is peeled away, and the pattern is rinsed with isopropyl alcohol and deionized water to remove residue. Patterning microchannels with kapton films presents a simple and fast fabrication method; however, these properties compromise edge definition and design flexibility of the microchannels.

3.2.5 Replica Molding of Microchannels with Silicon Molds

In order to discourage bonding between the elastomer and silicon mold in subsequent replica molding steps, a hydrophobic monolayer is introduced to the silicon molds through vapor deposition. The molds are placed in an evacuated chamber ($<$100 mTorr) with an open vessel containing a few drops of Trichloro(1H,1H,2H,2H-perfluorooctyl)silane (Aldrich) for $\geq$3 hours.

The silicone-based elastomer is spin-coated in liquid form against the silicon molds to result in a thin elastomer film of tunable thickness. For PDMS, the base and curing agents are mixed in a 10:1 mass ratio, and partially cross-linked in the mold by oven-curing at 60°C for 30-40 minutes. Microchannels are constructed by bonding patterned elastomer to unpatterned elastomer via oxygen plasma treatment (Technics Plasma Stripper/Cleaner; 65 watts for 30 seconds). The sealed microchannels are then completely cured at 60°C overnight. The microchannels are filled with eGaIn using

conventional tubing and syringe dispensing. Finally, wire is inserted into the ends of the microchannels, which are then sealed with a drop of uncured elastomer.

3.3 Sensor Behavior as a Function of Pressure

The change in electrical resistance ΔR of the embedded, conductive liquid-filled channels is measured as a function of the applied pressure using the experimental setup shown in Figure 3.3(b). Both experimentally measured values (open circles) and theoretical predictions (solid curve) are plotted in Figure 3.4 for an elastomer containing a straight channel that is $w = 2$ mm wide, $h = 1$ mm high, and has a top face that is a distance $z = 2$ mm from the surface of the elastomer. Pressure is applied over an area of length $L = 27$ mm and width $a = 25$ mm. For this set of measurements, the major axis of the contact area (which has length L) is aligned with the centerline of the channel. The plot contains data points from multiple loading and unloading cycles, demonstrating significant repeatability and low hysteresis.

As shown in the plot, the change in electrical resistance ΔR increases exponentially with applied pressure. This curve closely matches the theoretical prediction, which is represented by the solid line. It is important to note that no data fitting is used and the theoretical curve is derived entirely from the prescribed geometry, the prescribed pressure, the known resistivity $\rho = 29.4\times10^{-8}$ Ω/m of eGaIn [85] and the elastic modulus $E = 125$ kPa of the elastomer (Ecoflex®), which is independently measured by comparing the pressure with the depth of indentation.

The mechanics of the microchannel embedded elastomer are complex and can only be modeled with an approximate mathematical analysis. For the sake of simplicity,

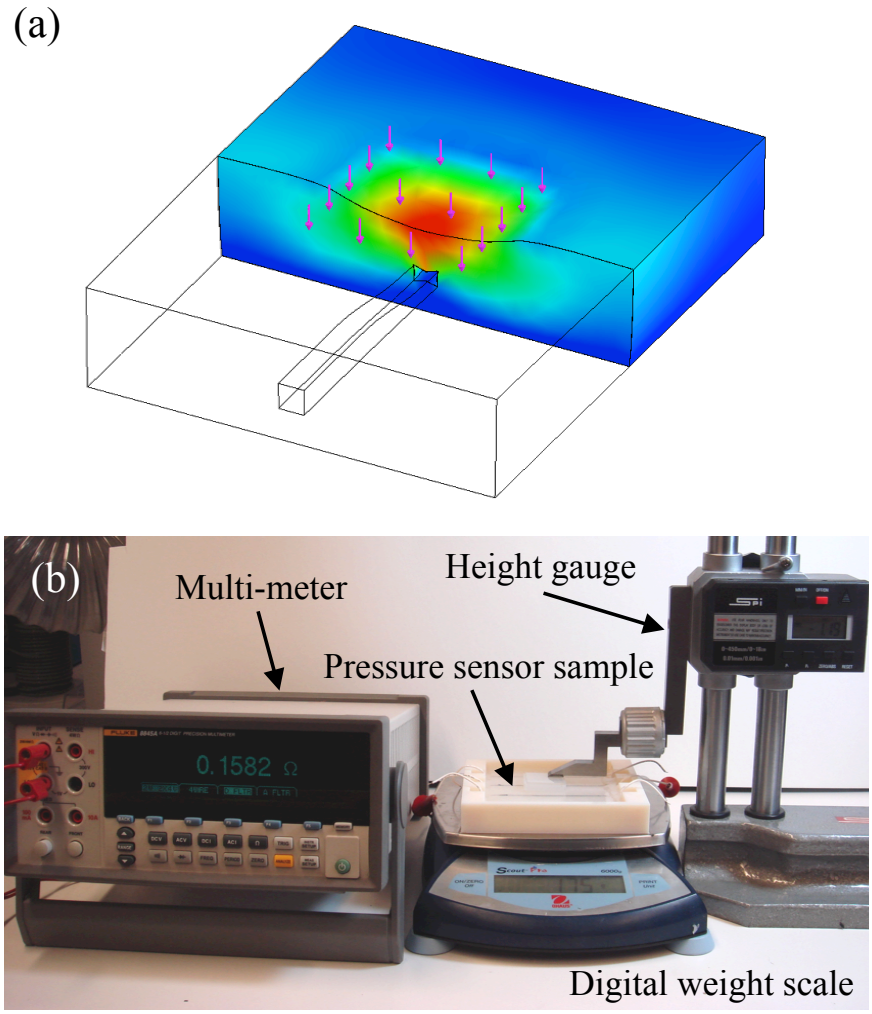

Figure 3.3: (a) Pressing the surface of the elastomer reduces the cross-sectional area of the embedded liquid channel and increases its electrical resistance. Contours represent the vertical displacement of the silicone rubber. (b) The experimental setup for simultaneously measuring applied pressure and electrical resistance. The ends of the eGaIn filled channels are wired to a precision multimeter (Fluke 8845A). A rigid glass rectangle of width a and length L is pressed into the sensor with a digital height gauge (Swiss Precision Instruments, Inc.). In order to distribute the pressure more uniformly and better simulate tactile or elastic contact, a 5 mm thick sheet of elastomer with the same area as the glass rectangle is inserted between the glass and the sensor surface. The sensor is supported by an electronic scale (6000g OHAUS Scout Pro) that measures the total force F exerted on the surface. The average pressure exerted over the area of contact is calculated as $p = F/aL$. (a-b) Figures contributed by Professor Carmel Majidi.

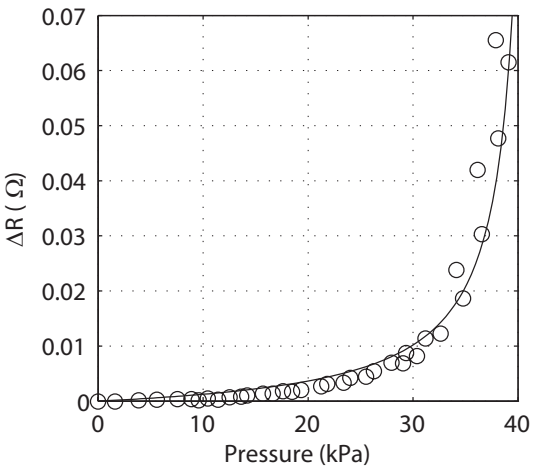

Figure 3.4: Experimental (open circles) and theoretical results (solid line) for the change in electrical resistance ΔR as a function of applied pressure for a contact area of width a = 25 mm and length L = 27 mm. The channel has a width w = 2 mm, height h = 1 mm, and top face that is a distance z = 2 mm from the surface. The theoretical prediction (3.2) is based on an electrical resistivity of $\rho = 29.4\times10^{-8}$ Ω/m and an independently measured elastic modulus of E = 125 kPa. Figure contributed by Professor Carmel Majidi.

consider a two-dimensional representation of a straight channel with rectangular cross-section embedded in an elastomeric matrix. As illustrated in Figure 3.5, the channel has width w, height h, and a top wall that is a distance z from the surface of the elastomer.

A uniform external pressure p is applied to the surface of the elastomer over an area of width a. As shown in Figure 3.5, the center of the channel and area of applied pressure are offset horizontally by a distance x. For channels close to the center of the applied pressure (i.e. $|x| < a/2$ and $z < a$), elastic deformation will reduce the cross-sectional area and hence increase electrical resistance.

Several assumptions are necessary in order to obtain a closed-form theoretical solution. First, we assume that the pressure distribution at the surface of the elastomer is uniform, which is consistent with the experimental setup detailed in Figure 3.3.

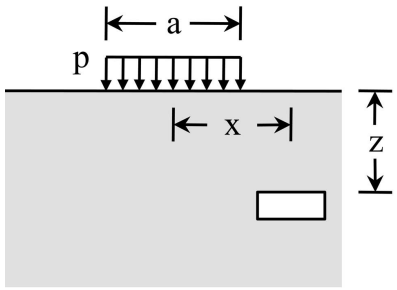

Figure 3.5: Two-dimensional, plane strain representation of elastomer embedded with a microchannel of width w and height h. The surface of the elastomer is subject to a pressure p uniformly distributed over a width a. Figure contributed by Professor Carmel Majidi.

Second, we assume that the cross-section of the microchannel will deform uniformly under pressure, such that the channel maintains a uniform height h. Therefore, the change is resistance across the deforming channel is given by the following relationship:

$$\frac{\triangle R}{R_0} = \frac{\frac{\rho L}{w}\left(\frac{1}{h_f} - \frac{1}{h_0}\right)}{\frac{\rho L}{w h_0}} = \frac{1}{1 + \frac{\triangle h}{h_0}} - 1. \tag{3.1}$$

Finally, we assume that we can treat the microchannel as an internal crack in a material undergoing uniform stress. According to Linear Elastic Fracture Mechanics, an average vertical stress σ_z applied in the vicinity of a crack will increase the gap between the crack faces by an amount $\Delta h = 2(1-\nu^2)w\sigma_z/E$, where ν is Poisson's ratio and E is the elastic modulus [90]. Because the microchannel is small compared to the dimensions of the elastomer, its influence on the stress distribution will be negligible except in the immediate vicinity of the channel. Therefore, for channels below the area of contact ($|x| < a/2$ and $z < a$), the average stress in the neighborhood of the channel may be approximated as $\sigma_z = -p$. Substituting this expression for Δh into Equation 3.1 implies that the total change in electrical resistance will be

approximately

$$\Delta R = \frac{\rho L}{wh}\left\{\frac{1}{1-2(1-\nu^2)wp/Eh} - 1\right\}. \tag{3.2}$$

3.4 Sensor Dynamic Range

Sensor dynamic range is controlled by a characteristic pressure $\hat{p} = Eh/w$ and thus depends only on the elastic modulus E of the elastomer and the aspect ratio h/w of the microchannel cross-section. Noting that $R_0 = \rho L/wh$ is the natural resistance of the channel, it follows from Equation 3.2 that for a channel embedded near the surface of the elastomer, $\Delta R/R_0 = 1/(1-2(1-\nu^2)p/\hat{p})$. Depending on the ratio $p/\hat{p}$, the relative change in electrical resistance can range from fractions of a percent to orders of magnitude. Consider, for example, EcoFlex® ($E = 125$ kPa) embedded with a microchannel of width $w = 100$ μm and thickness $h = 20$ μm. In response to a typical keystroke pressure in the range of 1-10 kPa, the electrical resistance of the embedded microchannel would change by approximately 1%. In contrast, peak pressures in foot-ground contact during walking are on the order of 100 kPa, which would result in a change in electrical resistance of approximately 50%. For all applications, the design parameters E and h/w should be selected such that the characteristic pressure $\hat{p}$ is comparable to the range of anticipated pressure p.

An in-depth analysis of change in electrical resistance as a function of channel depth and relative lateral position of the embedded channel has also been conducted, and is detailed in [91]. The results demonstrate the ability to mechanically decouple pressure sensing and strain sensing. A microchannel embedded deep within an

elastomer will only measure stretch and not pressure. Alternatively, a spiral shaped microchannel embedded close to the elastomer surface, as shown in Figure 3.1(a), will detect pressure but not uniaxial stretching. This is because increased electrical resistance in one direction is balanced by reduced resistance in the perpendicular direction.

3.5 Wearable Tactile Keypad with Stretchable Artificial Skin

To demonstrate one use of the soft pressure sensor design, a hyperelastic, thin, transparent pressure sensitive keypad is fabricated by embedding a silicone rubber film with conductive liquid-filled microchannels. Applying pressure to the surface of the elastomer deforms the cross-section of underlying microchannels and changes the electrical resistance across the affected channels. Perpendicular conductive channels form a quasi-planar network within an elastomeric matrix that registers the location, intensity, and duration of applied pressure. Serpentine channel patterns allow sensitivity to pressure over a larger area and simultaneously reduces channel deformation due to strain. Pressing channel intersections of the keypad triggers one of twelve keys, allowing the user to write any combination of alphabetic letters. A 5% change in channel output voltage must be achieved to trigger a key. It is found that approximately 100 kPa of pressure is necessary to produce a 5% change in voltage across a conductive microchannel that is 20 μm in height and 200 μm in width. Sensitivity of the keypad is tunable via channel geometry and choice of elastomeric material.

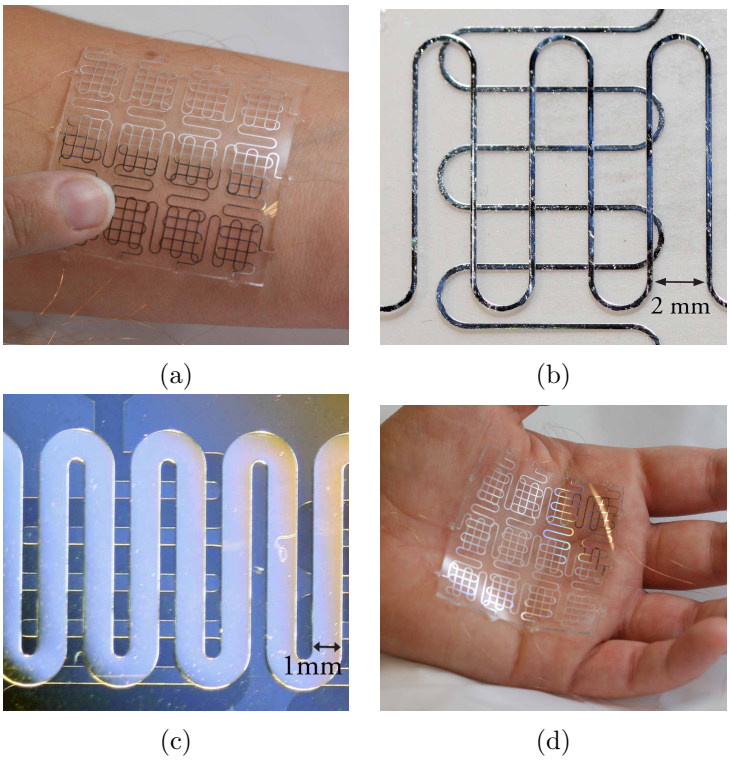

(a) (b)

(c) (d)

Figure 3.6: Thin sheets of polydimethylsiloxane (PDMS) silicon rubber embedded with conductive liquid-filled (eGaIn) microchannels for pressure sensing applications. (a) A twelve-key keypad resting on a wrist. The channels are 20 μm in height and 200 μm in width. The entire device thickness is approximately 700 μm. (b) A single key of the keypad shown in subfigure(a). (c) Conductive liquid-filled channels with dimensions of 10 μm in height and 1000 μm in width, for a channel aspect ratio equal to 0.01. (d) A twelve-key keypad resting in the palm of a hand, demonstrating its conformability.

3.5.1 Fabrication

Silicon wafers patterned with SU-8 photoresist are used to mold three PDMS layers that result in the keypad device. After vapor deposition of a hydrophobic silane, PDMS (Sylgard 184, Dow Corning) is spin-coated in liquid form (10:1 mass ratio of elastomer base to curing agent) onto a silicon mold to result in a thin elastomer film of tunable thickness.

As shown in Figure 3.7, the keypad device is comprised of two patterned PDMS

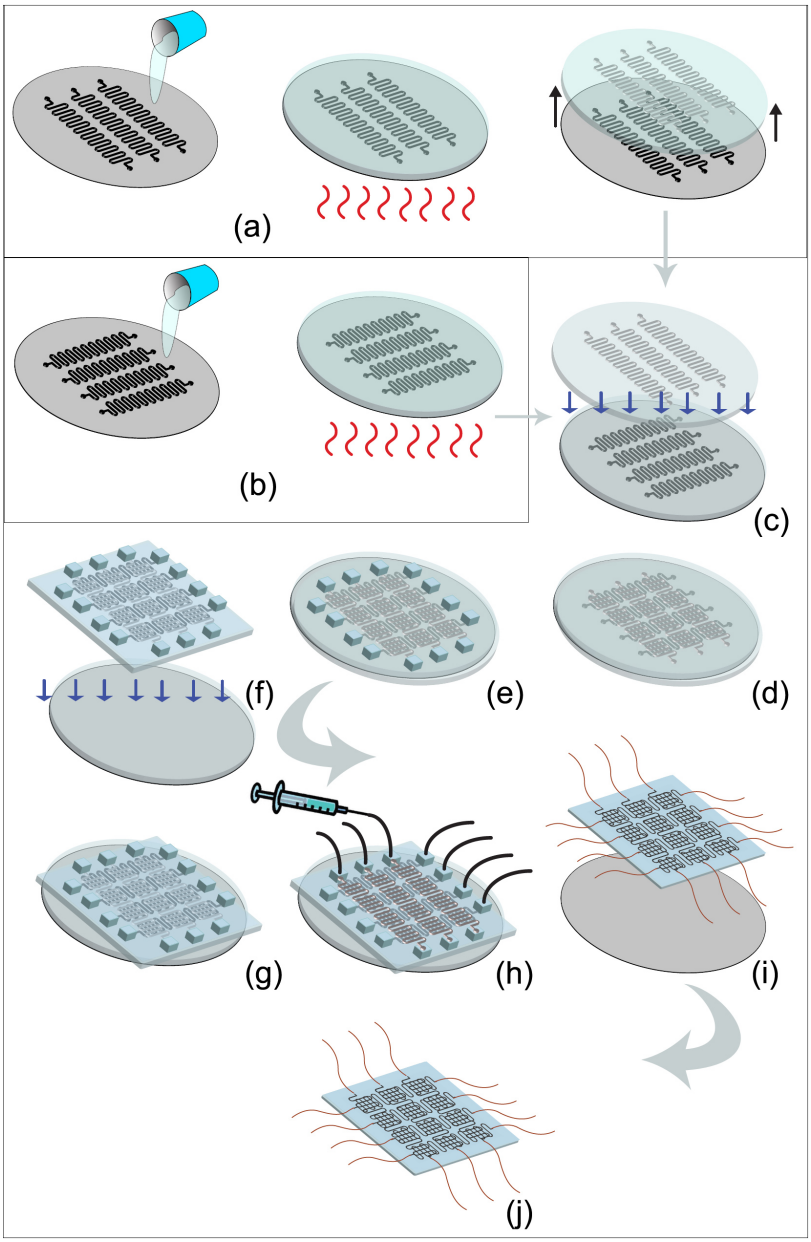

Figure 3.7: Keypad fabrication process. (a-b) Thin films of PDMS are spun onto silicon molds and thermally cross-linked. (c-d) PDMS layers are bonded via oxygen plasma treatment. (e) Blocks of PDMS are adhered to the channel pattern inlet and outlet locations. (f-g) The existing structures are manually cut and peeled from the silicon wafer, and holes are stamped through the PDMS blocks at the channel inlets and outlets. The channels are then bonded to a final, unpatterned PDMS film by means of oxygen plasma treatment. (h) A syringe is used to fill the microchannels with conductive liquid eGaIn at the inlets. (i) The PDMS blocks are cut and removed from the device, and conductive wires are placed into the channel ends. The channels are sealed with a final coating of PDMS. (j) The final device is peeled from the silicon wafer.

layers with a thickness of approximately 250 microns. The third and bottom layer of the device is unpatterned and approximately 200 microns in thickness. Each of the PDMS layers are cross-linked in the molds by oven-curing at $\sim 60\,^{\circ}\mathrm{C}$ for 30-40 minutes. Layers are manually removed from the molds and bonded together via oxygen plasma surface treatment, conducted at 65 watts for 30 seconds. Patterned layers are bonded together first, overlaying the channel patterns with the desired alignment.

In order to accommodate subsequent filling of the channels within such a thin device using conventional tubing and syringe dispensing, small blocks of PDMS are adhered to the device inlet and outlet locations on top of the cured PDMS. Adhesion is achieved by heating the cured PDMS on a hot plate at $100\,^{\circ}\mathrm{C}$, applying a small amount of uncured PDMS onto the inlet and outlet locations, and then pressing the PDMS blocks into the uncured droplets. These blocks are then allowed to fully cure on the hotplate for approximately 30 minutes. Lastly, small holes are introduced to the adhered inlet and outlet blocks, and the thin films are bonded to the unpatterned layer. Sealed microchannels are filled with eGaIn and the filling blocks are manually cut off. This step is largely enabled by the high surface energy of eGaIn, which allows a channel to be filled and remain in tact even if the channel inlet and outlet are exposed (assuming no external pressure is applied). The eGaIn-filled channels are then wired and re-sealed with a final coating of PDMS. The final device thickness is approximately 700 microns.

3.5.2 Experimental Setup

The keypad design tested in this work is a display of perpendicular serpentine channels for which the feature height is 20 microns and the width of the channels is 200 microns, yielding an aspect ratio of AR = 0.1. The serpentine pattern was chosen to increase the effective width of the sensing channels, hence allowing a change in local pressure to be detected over a larger area. As discussed in §3.4, pressure sensitivity of conductive liquid microchannels embedded in a silicon elastomer matrix is determined by the elastic modulus of the matrix and the aspect ratio of the channels. That is, the lower the aspect ratio of a rectangular microchannel, the greater the sensitivity of the pressure sensor. In the experimental keypad device tested here, a channel height of 20 microns was chosen to increase repeatability of the fabrication process, and a channel width of 200 microns increases transparency and overall aesthetics of the device.

The ends of the eGaIn-filled channels are wired to a DAQ breadboard (Measurement Computing USB-1208LS) for keypad device usage. As shown in Figure 3.8, the experimental circuit is composed of voltage dividers, where the applied voltage is 2 V and the initial voltage read by the DAQ is 0.9-1.1 V (depending on the channel). Because each of the conductive channels, or sensors, are in series with a 10 Ω resistor, it is implied that the sensors start out with a resistance of approximately 10 Ω.

Pressing each sensor increases the output voltage, V_{out}, across that channel. In order to eliminate noise in the voltage signal, a threshold of 5% was set, such that when the output voltage of the channel increases by 5% the key is interpreted to have been pressed. For example, for an initial voltage readout of 1 V, the key gets triggered when the voltage increases to 1.05 V or greater. According to this example

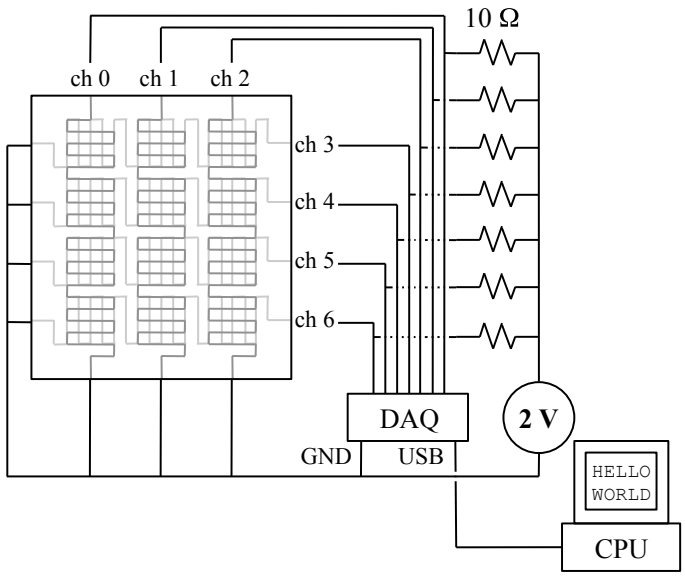

Figure 3.8: Wiring schematic for experimental testing of the twelve-key keypad.

and the governing equation of a voltage divider,

$$V_{out} = \frac{R_{out}}{R_{initial} + R_{out}} \cdot V_{initial} \tag{3.3}$$

a 5% increase in voltage corresponds to approximately a 10% increase in resistance.

An experimental code was developed with the Data Acquisition Toolbox in MATLAB R2010a (The Mathworks). In this setup, the twelve-key keypad was made to perform similarly to a mobile phone keypad. The functionality of the keypad is shown in Figure 3.9. By putting pressure on a key, two perpendicular channels each output a change in resistance, thus registering that the key was pressed and displaying the corresponding letter on a computer screen. Keys were able to produce multiple letters; by either holding down a key or pressing it in succession ($\leq$2 seconds) one could toggle through the available letter options. By waiting for a period greater than two

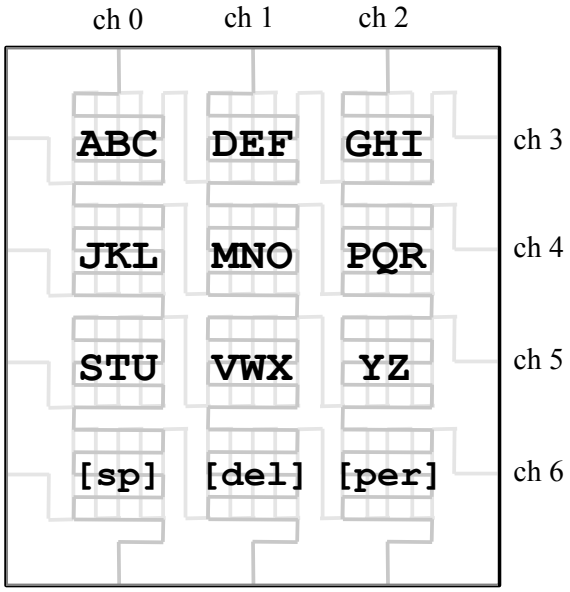

Figure 3.9: Schematic demonstrating the functionality of the keypad device (similar to a mobile-phone keypad). Each of the upper nine keys has the ability to toggle between three alphabetic letters. Sustaining pressure on a key, or pressing the key in succession, will toggle to the next letter. If the key is not pressed for a duration of two seconds, a new letter placeholder is realized.

seconds, a new letter could be inscribed.

3.5.3 Keypad Performance

Changes in electrical resistance and output voltage of the embedded, liquid-filled conductive microchannels was sensed and registered, resulting in real-time display of an alphabetic message on a computer monitor. One representative experiment is shown in Figure 3.10. The base voltage of each channel was normalized after data collection, such that only a relative change in voltage is relevant to the plot. The keypad was used in this trial to type the phrase 'HELLO WORLD'. One should note that the change in voltage, and hence applied pressure, lasts over varying durations and denotes the toggling of letters specific to the key being pressed. For example, to

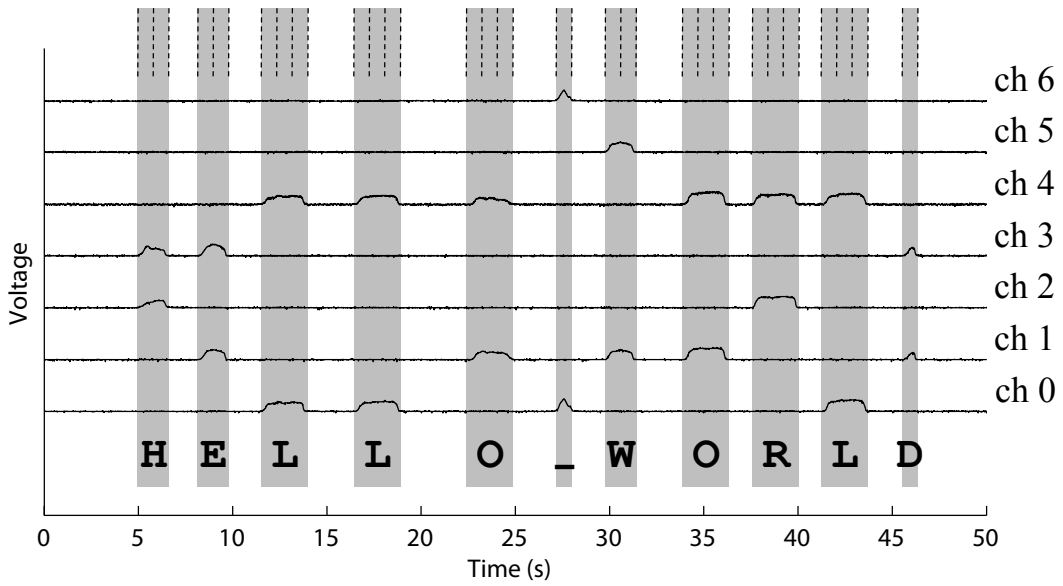

Figure 3.10: Representative results displaying signal as a function of time for each channel in the keypad device. Base voltage for each channel was normalized after data collection. A change in voltage denotes that a key has been pressed. Given the location and duration of pressure, the message 'HELLO WORLD' was typed using the keypad.

achieve the letter 'L', which is the third letter for a key as seen in Figure 3.9, pressure must be maintained on the key for approximately three seconds. Alternatively, to obtain the letter 'D', which is the first letter for a key, the pressure duration is less than one second.

Using a scale (ScoutPRO 6000g, OHAUS), we measured that about 10 N of force is necessary to increase V_{out} by 5%-10% and trigger a key. A typical fingerprint area is $\sim$1 cm^2, and thus the total necessary pressure to be applied is approximately 100 kPa. In contrast, normal keyboard typing is on the order of 5 - 10 kPa [92]. Trigger pressure, or the pressure required to change the output voltage of a channel by 5%, can be reduced by decreasing the aspect ratio of the channels or implementing softer materials. For example, EcoFlex® silicon rubber (0030, SmoothOn) has an

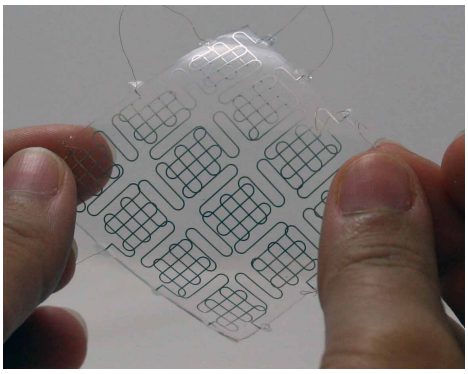

(a)

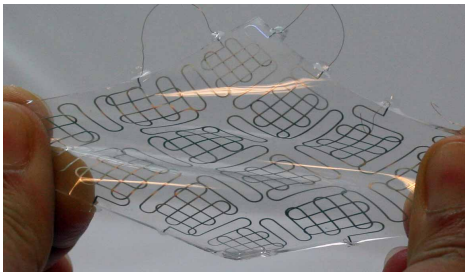

(b)

Figure 3.11: (a) An elastomeric keypad at a minimum energy configuration. (b) An elastomeric keypad under tensile deformation.

elastic modulus of ∼125 kPa, as opposed to 1 to 2 MPa for PDMS. Alternatively, the threshold value may be decreased based on the signal/noise ratio of the sensors and the resolution of the analog/digital converter used during experimentation.

Figure 3.6(c) displays a microchannel with a height of 10 microns and a channel width of 1000 microns, yielding an aspect ratio of 0.01. In Equation 3.2, it is seen that by reducing the aspect ratio by an order of magnitude (i.e. from 0.1 to 0.01), the relative change in electrical resistance is nearly 300%. Thus, it is clear that a lower aspect ratio increases the sensitivity of the channels' pressure sensing capabilities dramatically.

The mechanical limits of stretchability for both functionality and failure of the keypad were also investigated. The keypad device was stretched with pure tensile

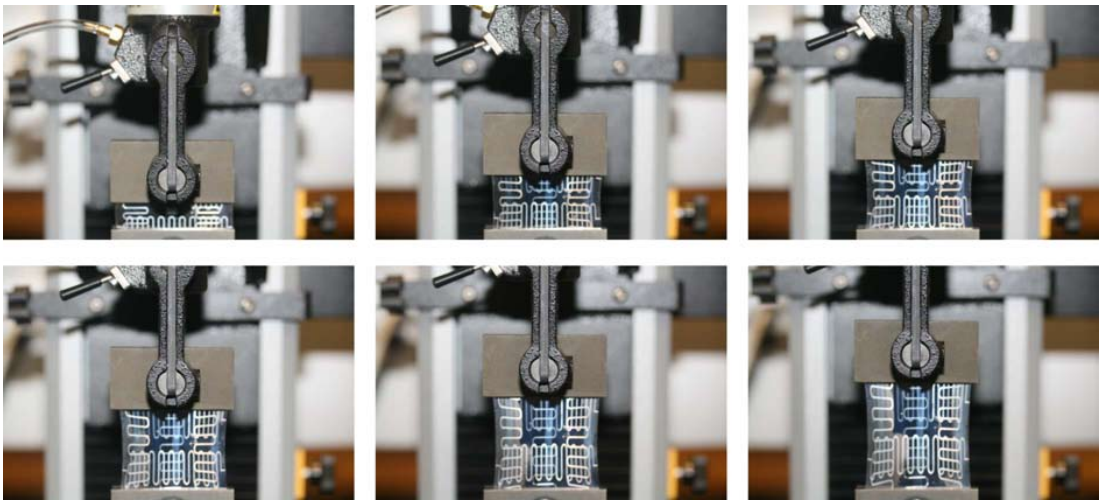

Figure 3.12: A keypad device undergoing tensile strain is shown to remain functional when stretched to over 350%. The device shown here is approximately 700 μm in thickness.

loading using an Instron Materials Testing System (model 5544A) in tensile extension mode. Functionality was considered to be maintained as long as all of the channels remained conductive. By this standard, the keypad was found to fail mechanically before failing in functionality. In fact, sensors became slightly more responsive to pressure under the stretched condition. Lastly, the keypad device was stretched to greater than 350% before mechanical failure.

3.6 Spatial Resolution

To determine spatial resolution of the soft pressure sensors for applications in micro-manipulation, a soft tactile sensor array for sub-millimeter contact localization and contact force measurement has been fabricated. The geometry and placement of conductive liquid embedded channels within the sensor array are optimized to provide adequate sensitivity for representative micro-manipulation tasks (the cross-

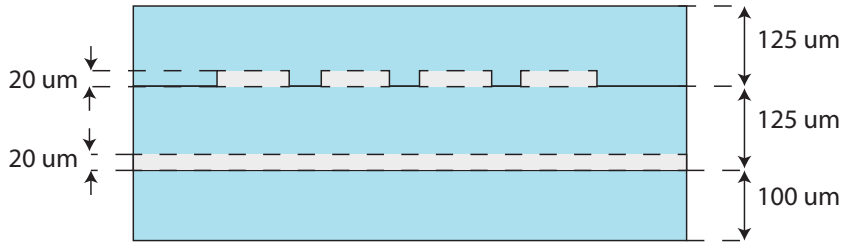

Figure 3.13: Cross-section of the soft tactile sensor array for sub-millimeter contact localization.

section geometry is shown in 3.13). Channels are 400 μm in width and 20 μm in height, with 200 μm of space for channel walls/septum. Mechanical testing of the sensor demonstrates a sensitivity of less than 50 mN (applied with a 500 μm diameter cylindrical indenter) and contact localization resolution on the order of 100's of microns.

3.7 Summary of Soft Pressure Sensors

The stretchable sensors and fabrication technology presented in this chapter may be applied to create other types of functional electronics and sensing. A pressure sensitive keypad is only one of many applications for this all-compliant sensing technology. Other soft sensor technologies, such as curvature and angle sensors, are necessary for the development of soft robotics, artificial skin, soft orthotics, and many more applications. Several designs for curvature and bend angle sensors are introduced in the next chapter.

Chapter 4

Non-Differential Curvature Sensing with Liquid-Embedded Elastomers

In this chapter, soft lithography microfabrication and design methods are extended to introduce a curvature sensor that is soft (modulus 0.1-1 MPa) and stretchable (100-1000% strain). In contrast to existing curvature sensors that measure differential strain, this new class of sensors measures curvature directly. Moreover, the sensor is composed entirely of soft elastomers (PDMS or EcoFlex®) and conductive liquids (eutectic gallium-indium, eGaIn) and thus remains functional even when stretched to several times its natural length. Electrical resistance in the embedded eGaIn microchannel is measured as a function of bending curvature for a variety of sensor designs.

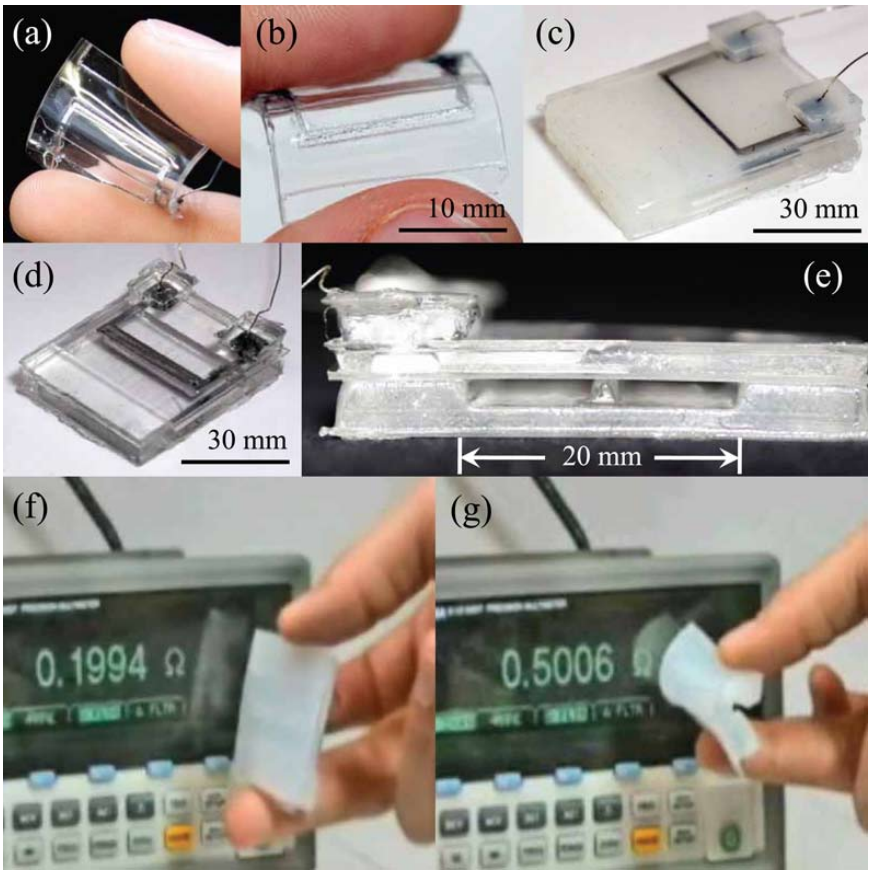

Figure 4.1: Bending a micropatterned elastomer changes the electrical resistance of an embedded conductive liquid microchannel; Experiments are performed on a (a,b) 1.3 mm thick PDMS sensor, a 6 mm thick (c) EcoFlex®, and (d,e) PDMS sensors; (f,g) bending the EcoFlex® sensor.

4.1 Soft Curvature Sensor Design

For hyperelastic strains of 100-1000%, electronic functionality is achieved by embedding microchannels of conductive liquid in a thin elastomer film [85]. This approach builds on the manufacturing techniques [93] developed for elastomer-based microfluidics [94] and has been utilized for strain sensing [82, 95], pressure sensing (discussed in Chapter 3), and a mechanically tunable antenna [81, 96].

Here, liquid embedded elastomers are employed to introduce a hyperelastic and

non-differential curvature sensor (Figure 4.1). The sensor is composed of two coplanar elastic films that are attached at opposite edges and at the center by a parallel strut. One of the films contains a microchannel of conductive liquid (eutectic gallium-indium, eGaIn) that is oriented along the strut. Bending the sensor induces a compressive force in the strut, which consequently exerts a pressure on the embedded microchannel. This pressure causes the cross-section of the channel to elastically deform and, following Ohm's law, leads to a change in electrical resistance. Bending curvature is inferred from the relative change in electrical resistance of the embedded microchannel.

4.2 Theoretical Predictions for Sensor Behavior

Referring to Figure 4.2(a), two elastomer films of thickness h are separated by a gap of height g and length L. As shown in Figure 4.2(b), the top film contains an embedded channel with a width w, height H, length λ, and a bottom wall thickness t. The two plates are connected along both their edges as well as along a strut of width s, height g, and a length λ that is co-linear with the embedded channel.

A free body diagram of the plates and strut is presented in Figure 4.3. During bending, an axial force f induces a compressive force P in the strut. If the channel is wider than the strut ($s < w$), then this bending-induced compression will cause the strut to pierce into the channel as illustrated in Figure 4.2(d). Alternatively, if the strut is wider ($s > w$), then the elastomer will deform around the channel. In either case, the force P will reduce the cross-sectional area A of the embedded channel and cause the electrical resistance R to decrease by an amount ΔR.

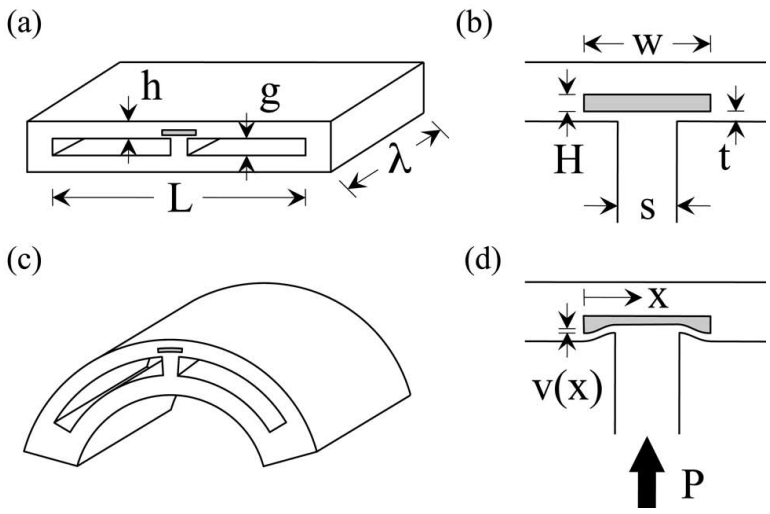

Figure 4.2: (a) The curvature sensor is composed of two thin films with thickness h, length L, and width d that are separated by a gap g and bonded along their two ends as well as along their midline by a strut of width s. (b) One of the films contains a microchannel of height H and width w located a distance t above the strut. (c) Bending induces a compressive force P that (d) causes the embedded channel to collapse. Figure contributed by Professor Carmel Majidi.

Mechanical coupling between plate bending and internal pressure allows the curvature magnitude $|\kappa|$ to be estimated from the corresponding change ΔR within the embedded channel. The sensor output ΔR is proportional to the electrical resistivity ρ of the conductive liquid. eGaIn has a resistivity of $\rho = 29.4\times10^{-8}$ Ω/m [85] that is comparable to other metal alloys and several orders of magnitude lower than the resistivity of conductive inks and carbon-based liquids.

4.2.1 Pressure mode (s >w)

When the strut is wider than the channel, pressure from the strut will be distributed around the channel and compress the surrounding elastomer. This loading condition is similar to that previously addressed in Chapter 3, in which pressure p

is exerted on the surface of an elastomer embedded with a microchannel of conductive liquid. According to that analysis, the relative change in electric resistance is approximately

$$\Delta R = \frac{\rho L}{wh}\left\{\frac{1}{1-2(1-\nu^2)wp/Eh}-1\right\}. \tag{4.1}$$

For a thin plate, stress is restricted to the plane of the plate and strain is restricted to the plane of bending. Hence, the bending modulus B is defined as the tensile (Young's) modulus E divided by $1-\nu^2$, where ν is Poisson's ratio. Substituting $E = B(1-\nu^2)$ into Equation 4.1, we find:

$$\frac{\Delta R}{R_0} = \left\{1-\frac{2wp}{BH}\right\}^{-1} - 1\,, \tag{4.2}$$

where $R_0 = \rho\lambda/wH$ is the original (undeformed) electrical resistance and ρ is the electrical resistivity of the liquid. The pressure p is estimated by simply dividing the strut force P by its cross sectional area: $p = P/s\lambda$.

A full analysis for this configuration was derived by Professor Carmel Majidi and is included in [97], however the end result of the analysis is given here:

$$\Delta R = \frac{\rho\lambda}{wH}\left\{\frac{1}{1-\alpha\kappa h\sin(\kappa L/2)}-1\right\}, \tag{4.3}$$

where

$$\alpha = \frac{2w(g+h)}{Hs}\,. \tag{4.4}$$

The constants w and H correspond to the original dimensions of the embedded channel, prior to bending, and are thus independent of the curvature. The approxi-

mation (4.3) is only valid when $\alpha\kappa h \sin(\kappa L/2) < 1$, which follows from the constraint $2wp/BH < 1$ [91]. Physically, this bound arises from the unilateral constraint that prevents the collapsing channel walls from interpenetrating.

As expected, the electrical resistance increases monotonically with increasing absolute curvature $|\kappa|$ and increases by the same amount regardless of whether κ is positive or negative. Moreover, the solution suggests that ΔR increases with increasing film thickness h, gap height g, and gap length L and decreasing strut width s. Interestingly, ΔR is invariant to B, although the bending modulus will control how much moment is required to reach a prescribed curvature κ.

4.2.2 Collapse mode (s <w)

When $s < w$, the strut is modeled as a rigid link supported by two flexible plates. Compression in the strut will cause the plates to deflect into the channel by an amount $v(x)$, where x is the distance from the channel side-wall (see Figure 4.1(d)). By evaluating $v(x)$, the total change in channel cross-section ΔA may be derived, thus allowing calculation of the change in electrical resistance.

A full analysis for this configuration is included in [97], however the end result of the analysis is given here:

$$\Delta R = \frac{\rho\lambda}{wH}\left\{\frac{1}{1-\beta\kappa h\sin(\kappa L/2)} - 1\right\}, \tag{4.5}$$

where

$$\beta = \frac{(g+h)(3s+w)(w-s)^3}{64wHt^3}. \tag{4.6}$$

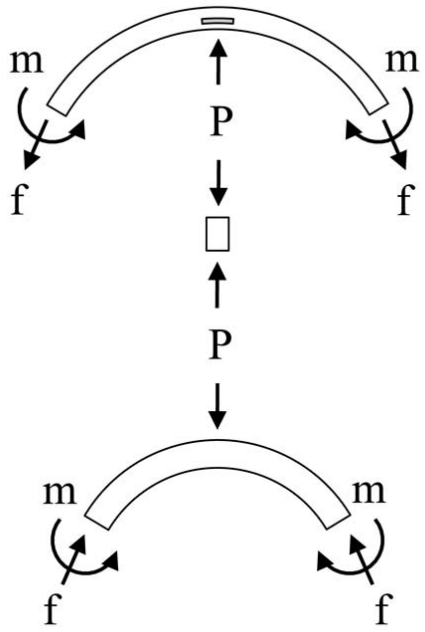

Figure 4.3: Free body diagram of plates and strut. Figure contributed by Professor Carmel Majidi.

As in Equation 4.3, ΔR monotonically increases with increasing curvature $|\kappa|$, plate thickness h, gap height g, and gap length L. However, it is no longer monotonically dependent on strut width s.

4.2.3 Non-linear Plate Deflection

For large bending curvatures, the compressive membrane force f induced within the inner film will exceed its critical buckling strength f_{cr} and the film will buckle. It is important to note that in addition to the axial load f, the plates are subject to an internal bending moment. This combined loading leads to non-linear deflection even when $f < f_{\text{cr}}$ (see Figure 4.4). This premature subcritical plate buckling can

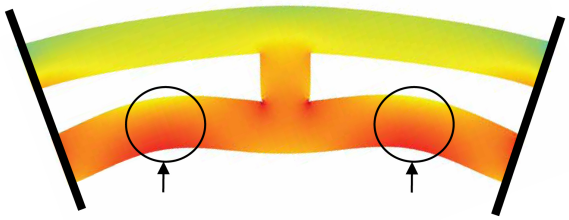

Figure 4.4: For large bending curvatures, the compressive membrane force f induced within the inner film will exceed its critical buckling strength f_{cr} and the film will buckle, which may cause the gap to collapse and redirects compressive stress away from the strut and towards the new plate contacts. Figure contributed by Professor Carmel Majidi.

cause the gap to collapse and redirects compressive stress away from the strut and towards the new plate contacts. Therefore, the critical curvature κ_{cr} at which the inner film will reach its critical buckling strength f_{cr} represents an upper bound of the corresponding theoretical predictions for ΔR. Hence, for $\kappa > \kappa_{\text{cr}}$, the theory may overestimate the true change in electrical resistance. κ_{cr} is noted by vertical dashed lines in Figure 4.5.

4.3 Description of Experiment

Curvature measurements are performed on three elastomer sensors, two that are 6 mm thick and a third that is 1.3 mm thick. The 6 mm thick samples are produced by pouring uncured PDMS (Dow Corning) or soft silicone rubber (EcoFlex® 0030, SmoothOn) into a 3D-printed mold (Connex 500, Objet Ltd.) (as in §3.2.1). The 1.3 mm samples are produced by spin coating uncured PDMS on glass slides that are patterned with laser-cut (VersaLaser system, Universal Laser Systems) adhesive films (as in §3.2.4). After curing, the elastomer sheets are released, bonded, and a syringe

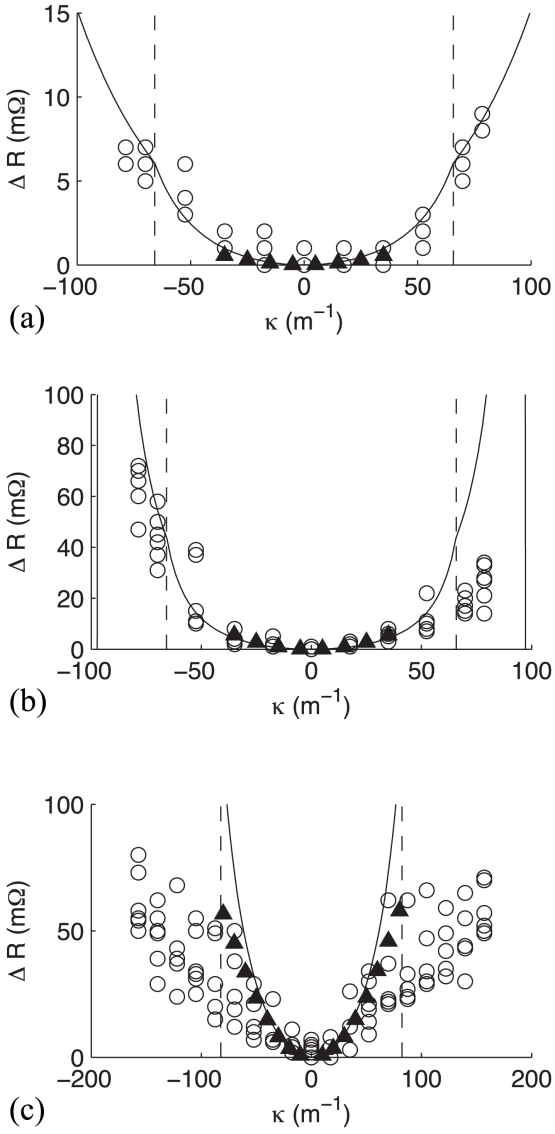

Figure 4.5: Change in electrical resistance ΔR as a function of pure bending curvature κ. Experimental measurements (open circles) and theoretical prediction (solid curve) for 6 mm thick (a) PDMS and (b) EcoFlex® sensors and (c) a 1.3 mm thick PDMS sensor. The vertical dashed lines correspond to $\kappa = \kappa_{\text{cr}}$. For the 6 mm sensors, $L = 20$ mm, $g = 2$ mm, $\lambda = 26$ mm, $H = 0.5$ mm, $h = 2$ mm, $s = 2$ mm, $t = 0.4$ mm, $w = 3$ mm (PDMS), and $w = 1$ mm (EcoFlex®). For the 1.3 mm sensor, $L = 10$ mm, $g = 0.3$ mm, $\lambda = 16$ mm, $H = 50$ μm, $h = 0.5$ mm, $s = 1$ mm, $t = 0.1$ mm, $w = 0.8$ mm. The closed triangle markers correspond to theoretical predictions based on FEM solutions for f.

is used to fill the embedded channels with eGaIn. Wire is inserted into the ends of the channels, which are then sealed with a drop of uncured rubber.

The change in electrical resistance ΔR is measured as a function of bending curvature κ. Rigid plastic clamps are fitted around the bonded edges of the elastomer. Pure bending is induced by positioning the base of the plastic clamps at various geometrically-defined orientations. These positions and orientations are carefully selected so that the sensor bends into a circular arc of radius $r = 1/\kappa$ without stretching. The clamps are sequentially oriented from 0^o to 90^o, back to 0^o, then to -90^o, and lastly back to 0^o. The change in electrical resistance (ΔR) is measured with a precision multimeter (Agilent 34401A). The scatter in data is attributed to the manual rotation of the clamps and can be mitigated with an automated testing platform.

4.4 Comparison of Empirical, Analytical, and FEM Results

Experimentally measured values of ΔR are plotted versus κ for 6 mm thick PDMS (Figure 4.5(a)) and EcoFlex® (Figure 4.5(b)) sensors and a micropatterned 1.3 mm thick PDMS sensor (Figure 4.5(c)). The sensors demonstrate the expected monotonic dependency of electrical resistance on absolute bending curvature. Nonetheless, there appears to be considerable scatter in the experimental data. This is predominately caused by the motion of the wires that connect the liquid microchannels with the multimeter. Because eGaIn has low electric resistivity, the external wiring and electrical connections contribute significantly to both the total resistance and resistance

fluctuations. This may also explain why the more rigid 6 mm PDMS sample exhibits less scatter, since the embedded wires have less relative mobility. Other sources of scatter may include manual reorientation of the clamps and fluidic or viscoelastic effects in the sensor itself.

Theoretical predictions are also plotted in Figure 4.5 and appear to be in reasonable agreement with the experimental measurements. Solutions based on a finite element (FEM) solution for f (COMSOL Multiphysics 4.0a) are plotted with closed triangle markers. These FEM solutions account for subcritical buckling induced by combined axial and moment loading in the plates and hence provide a more accurate estimate of the bending resistance. For the 6 mm thick PDMS sensor, the embedded channel is wider than the strut and so the collapse mode solution in Equation 4.5 is used to predict ΔR. For the other two samples, the strut is wider and so the pressure mode solution in Equation 4.3 is used. The theoretical curves for $|\kappa| > \kappa_{\mathrm{cr}}$ are obtained by replacing the axial load f with f_{cr}, as described in §4.2.3. These curves do not account for large plate buckling that would cause the gap to collapse. Nonetheless, we expect that when curvature is large ($\kappa > \kappa_{\mathrm{cr}}$) collapse is possible and this will significantly reduce the sensitivity of the sensor.

For the results in Figures 4.5(a-b), we observe reasonable agreement between theory and experiment. This indicates that the theoretical models are predictive, i.e. the relationship between κ and ΔR can be established from prescribed sensor geometries (w, L, h, H, g, s, t, λ) and conductor resistivity (ρ). For Figure 4.5(c), however, we find that the theory overestimates the sensitivity of the 1.3 mm PDMS sensor. One possibility is a slight misalignment between the strut and embedded

channel, which will reduce the pressure exerted on the channel. While misalignments can also arise in the 6 mm sensors, the feature sizes are larger and so there will be less relative impact on performance. This may explain why the 6 mm sensors exhibit greater agreement with the theoretical and computational predictions.

4.5 Integrated Geometries for Joint Angle Proprioception

In this section, the functionality of the sensor will be demonstrated through testing on a finger joint. The film is wrapped around a finger with the sensing element positioned on top of the knuckle. Finger bending both stretches the elastomer and exerts pressure on the sensing element, leading to an enhanced change in the electrical resistance. Because the sensor is soft (elastic modulus $E \sim 1$ MPa) and stretchable (>350%), it conforms to the host bending without interfering with the natural mechanics of motion. This mechanically passive functionality is particularly important for fingers and end effectors that perform delicate tasks and are sensitive to motion constraints. As illustrated in Fig. 4.6, such sensors may be incorporated into a glove to monitor hand motion or used to measure joint angles for a robotic manipulator. This sensor represents the first use of liquid-embedded elastomer electronics to monitor human or robotic motion.

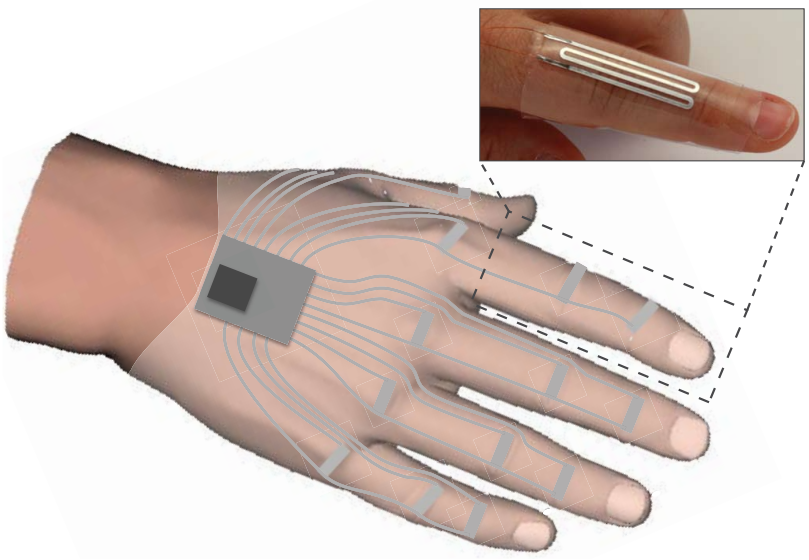

(a)

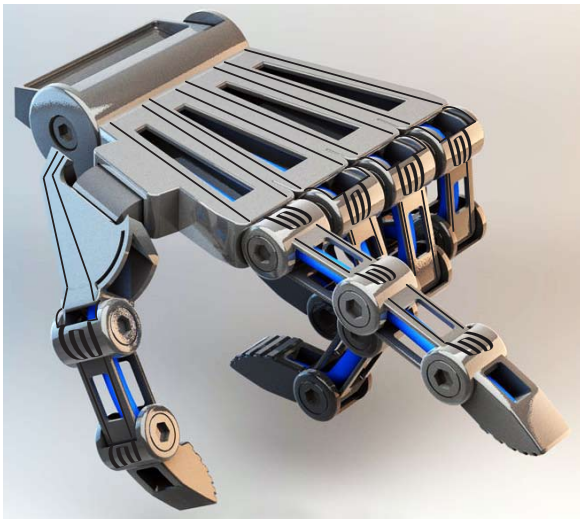

(b)

Figure 4.6: Elastomer-based curvature sensors allow mechanically non-invasive measurement of human body motion and robot kinematics. (a) An illustration of a human hand covered with curvature sensors at every joint. Inset: An actual sensor mounted on a host finger. The sensor consists of a 300 μm thick elastomer sheet embedded with a microchannel filled with a conductive fluid. (b) A concept robotic manipulator mounted with curvature sensors at the joints.

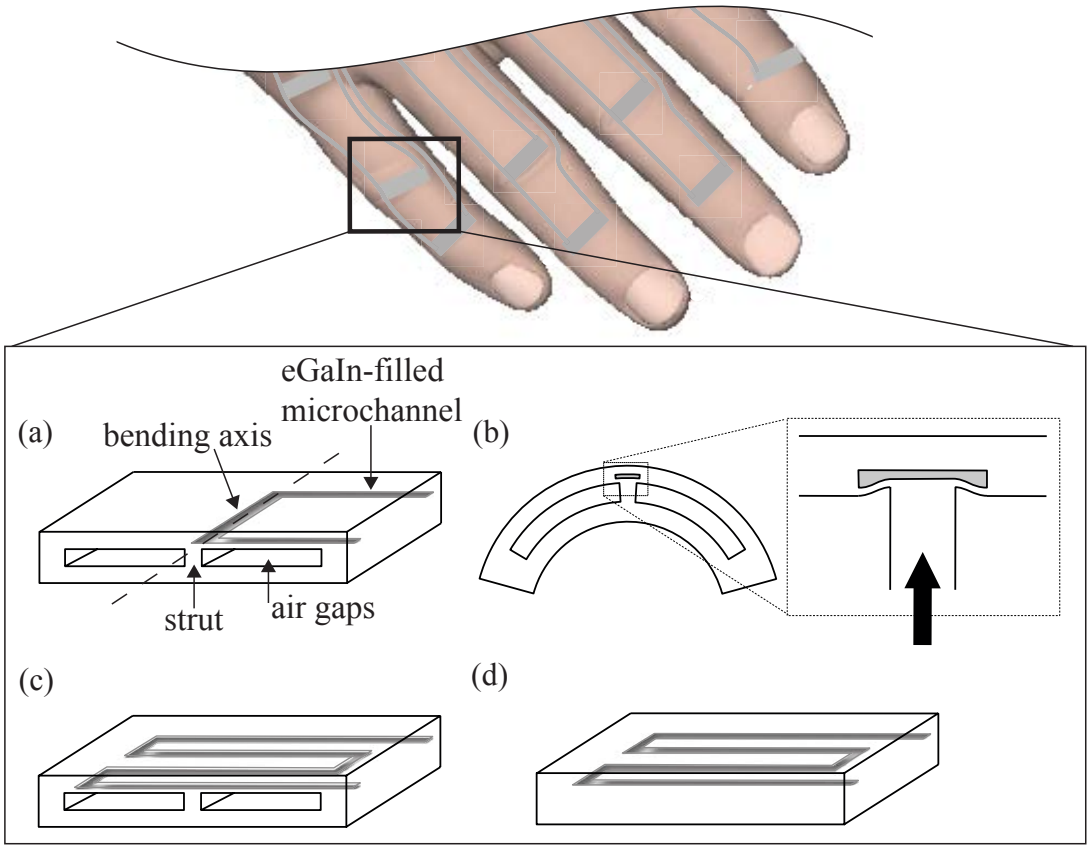

Figure 4.7: Bend sensor geometries. (a) The pure curvature sensing geometry, composed of two elastomer sheets that are attached at opposite edges and at the center by a strut. A straight microchannel of conductive liquid is embedded parallel to the strut. When the sensor is bent about the axis of the strut, a compressive force is induced in the strut and applied to the embedded microchannel. As shown in (b), the cross-section of the microchannel is deformed due to the applied pressure and electrical resistance across the channel increases. (c) A serpentine channel and a perpendicular strut. When the sensor bends, the microchannel is deformed at locations where it intersects the strut. The serpentine geometry of the channel allows for simultaneous curvature and strain sensitivity. (d) An embedded serpentine microchannel. This geometry is sensitive only to strain.

4.5.1 Previous Work on Angle Sensors

Curvature and joint angle sensors allow real-time kinematic feedback in robotic manipulation, which is necessary for a system to react intelligently to its environment. Existing solutions for joint angle sensing rely on thin-films and fibers that are flexible but not soft or stretchable. Existing commercial products include Bi-Flex Sensors™ (Images Scientific Instruments), Bend Sensor® (Flexpoint Sensor Systems), and Flexiforce® Sensors (Tekscan, Inc.). Other examples include an angular displacement sensor containing a thin-metal-film strain gage, which operates with 100-750 Ω resistance and is accurate to within 10° [98]. A capacitive finger angle position sensor has also been developed, which features a high resolution of 0.02° over the absolute measurement range of 180° [99].

Finger joint angles are also measured using fiber Bragg grating (FBG) strain sensors [100]. In [101], a superstructure fiber Bragg grating is used to simultaneously measure strain and curvature. Other Bragg grating sensors have demonstrated evolving levels of sophistication, such as the capability to determine bend direction [102, 103, 104], integration of flexible materials such as elastomers [105] and polymer optical fiber [106], self-alignment [107], simultaneous temperature measurement [108] and general increased sensitivity [109].

Despite high bend sensitivity, fiber Bragg gratings exhibit several disadvantages as curvature sensors, including measurement in reflection only or transmission only (for long-period gratings), broad resonant wavelengths that limit measurement accuracy, and strain-induced failure due to non-compliant materials. Strain or curvature sensors which are entirely soft would allow seamless integration into existing robotic

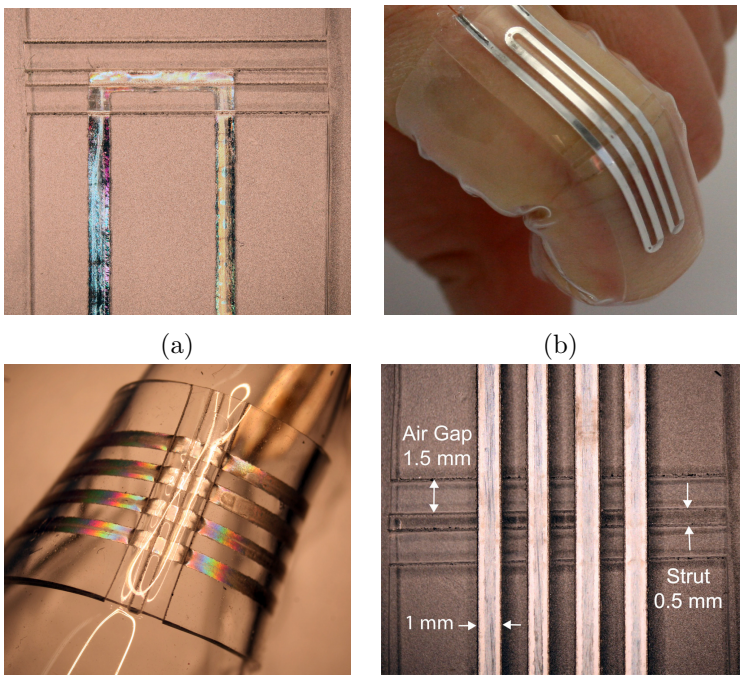

Figure 4.8: Bend sensors for determining joint angles. (a) The pure curvature sensing geometry. (b) The combined strain-curvature sensor, made from a strain-sensing serpentine channel and including an integrated strut/gap layer. This device is further detailed in (c) and (d).

manipulators, providing proprioceptive feedback with little or no interference to the motion of the system.

Existing bend sensors have been central in the development of data gloves for monitoring hand motion. An extensive review of glove-based motion acquisition is presented in [110]. Despite the enormous progress in this field, important challenges remain, including compliance matching with natural hand motion and active response for tactile feedback and motor assistance.

4.5.2 System Description

We combine stretch and curvature sensing to introduce a family of wearable soft sensors that detect bending and joint position and that are composed of all-compliant elastomer and liquid materials. Three geometries are explored in detail to distinguish the mechanics of curvature sensing, strain sensing, and combined strain-curvature sensing. The curvature sensor, shown in Figure 4.7(a), measures direct curvature but is insensitive to strain. The strain sensor, seen in Figure 4.7(d), measures differential strain but does not measure direct curvature. However, during finger bending, a sensor that is roughly adhered to the skin will both stretch around the knuckle as well as bend. Furthermore, the knuckle itself may apply pressure to the sensor's embedded microchannel during bending, hence increasing the measured change in resistance. We therefore test a third combined strain-curvature sensor, shown in Figure 4.7(c). These sensors are composed of sub-millimeter thick films of PDMS rubber embedded with 50 μm deep channels of eGaIn conductive liquid.

In this particular study, the sensors are wrapped around a finger joint with the embedded sensing element positioned above the middle (second from the fingertip) knuckle. Bending the finger causes the knuckle to stretch the elastomer and exert a pressure on the sensing element. The combination of stretching, pressure, and curvature leads to a change ΔR in the electrical resistance of the sensor. Finger bending is detected when the relative change in resistance $r = \Delta R/R_0$ exceeds a critical threshold. The joint angle may also be estimated from the change in resistance, although this requires sensor calibration.

4.5.3 Fabrication

Device Fabrication

Curvature sensors are produced through a soft microfluidics manufacturing process. Microchannel molds are fabricated using the method described in §3.2.4, and the devices are completed using the replica molding process previously described in §3.2.5.

The devices shown in Figure 4.8 are composed of a 200 μm film of patterned PDMS bonded to a 100 μm film of unpatterned PDMS. The strut is fabricated by patterning two layers of 127 μm thick adhesive-backed kapton film on glass. In this work, the strut is laser-cut to be 0.5 mm in width and the gaps on either side of the strut are 1.5 mm in width. The strut is approximately 260 μm in height, and the final plate thickness is 300 μm. This structure is 560 μm in total thickness. The total thickness of the strain sensor is 300 μm, and the total thickness of the sensors with struts is 860 μm.

The parameters defined by Figure 4.2(a-b) are given as: h = 300 μm, g = 260 μm, L = 3.5 mm, λ = 7 mm, w = 1 mm, H = 50 μm, t = 100 μm, s = 0.5 mm. Dimensioning is consistent across the sensor geometries, with only the microchannel pattern varying.

Flexible Circuit Connections

Motion of the wires that connect the liquid microchannels with the multimeter tend to cause considerable scatter during experimental testing, due to the low resistivity of eGaIn. Therefore, an alternative technique has been developed in which a

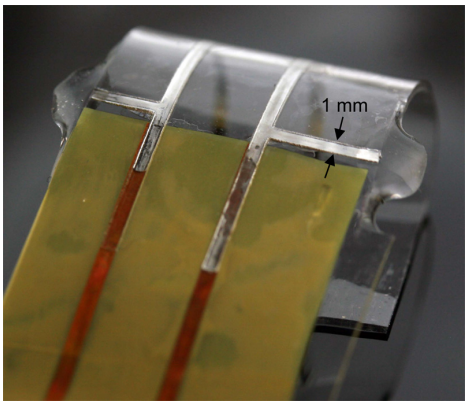

(a)

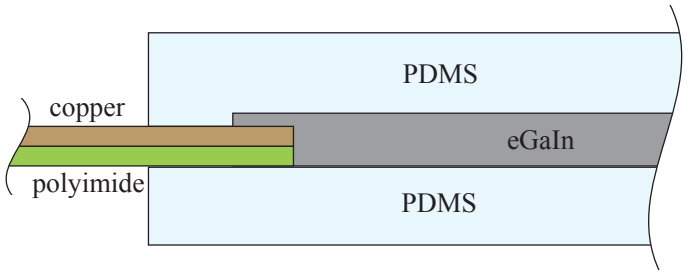

(b)

Figure 4.9: (a) A patterned copper-polyimide film is bonded directly to one edge of a curvature sensor. The eGaIn-filled microchannel partially overlaps copper leads, which continue out of the microchannel and may be connected to external circuitry. (b) A cross-sectional view of the flexible circuit connection.

flexible circuit is bonded directly to one edge of the device, as shown in Figure 4.9.

Flexible circuits are made from polyimide/copper laminate (DuPont). Circuit traces are achieved by patterning the copper via a photolithography process followed by a ferric chloride etch. Flexible circuits are bonded to PDMS films through an amino-epoxy chemical bonding method [111, 112]. First, an unpatterned PDMS surface is exposed to oxygen plasma (65 watts for 30 sec) and immediately coated in 5% (v/v) (3-Aminopropyl)triethoxysilane (99% Sigma Aldrich). The flexible circuit (polyimide film) is also treated with plasma, and the entire film is submerged in 5% (v/v) (3-Glycidyloxypropyl)trimethoxysilane (98% Sigma Aldrich). After at least 20

minutes, excess silane is discarded, the surfaces are rinsed with deionized water, and the films are placed on a hot plate or in an oven at 60°C to dry. The unpatterned surface of the polyimide may then be bonded to the PDMS with light pressure. The same process is then repeated between the composite surface and a third layer of patterned PDMS. Placing the contacted surfaces in an oven at 60°C for several hours finalizes the chemical bond. In this final process, the copper leads of the flexible circuit must be carefully aligned with the inlet and outlet of the microchannel when bringing the surfaces into contact.

The contact resistance of the sensors does not noticeably change as a result of this electrical connection method.

4.5.4 Calibration of Soft Angle Sensors

As discussed in §4.4, a very thin (sub-millimeter) curvature sensor will encounter enhanced boundary effects, plate buckling, and exaggerated effects due to misalignment that cannot be accounted for in the predictive model. In this work, predictive models are not sufficiently accurate due to the scale and materials of the sensors. We therefore calibrate the sensor geometries to establish range and sensitivity.

Idealized Calibration

Curvature sensors were calibrated both on and off of a finger. Pure bending of the sensors was induced off of a finger by adhering the faces to rigid blocks and positioning the blocks at various angles, defined by an 'angle wheel' (Figure 4.10). The edges of the blocks were carefully aligned with the edges of the curvature sensor

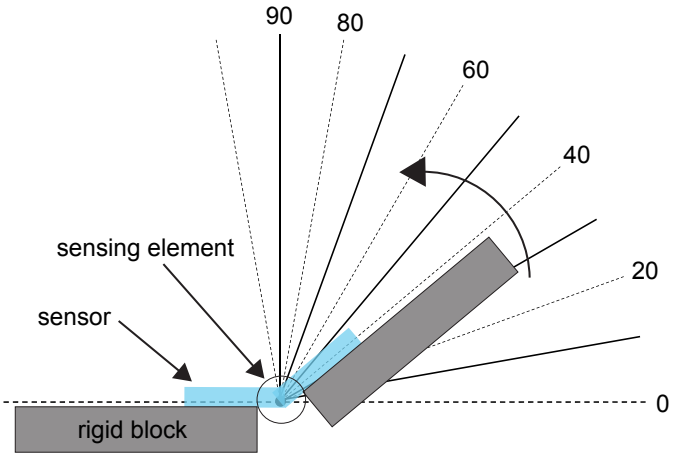

Figure 4.10: Idealized calibration schematic.

gaps, separated by a distance $L = 3.5$ mm, such that all bending was concentrated at the location of the sensing element. When testing the strain sensor, the distance between the blocks remained consistent. The use of rigid blocks increases positioning accuracy, reduces twisting or stretching of the sensor and maintains the radius of curvature throughout testing.

The rigid blocks were oriented from 0° to 100°, at 10° increments, and the change in electrical resistance was measured with a precision multimeter (Agilent 34401A). Curvature measurements were repeated eight times for each sensor geometry, and are shown in Fig. 4.11(a). As expected, the change in electrical resistance ΔR increases as a function of bending angle θ. Green markers represent the strain sensor, black markers correspond to the pure curvature sensor, and red markers indicate the integrated geometry.

In this experimental setup, the pure curvature sensor demonstrates the greatest relative change in resistance during bending, which is expected given the pure bend-

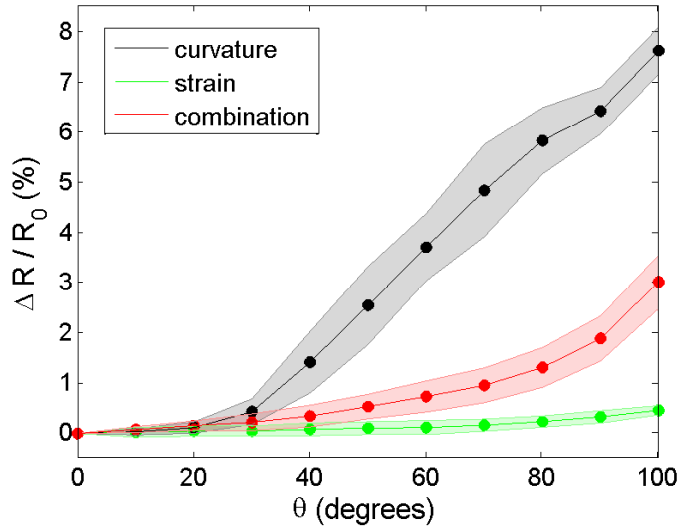

(a)

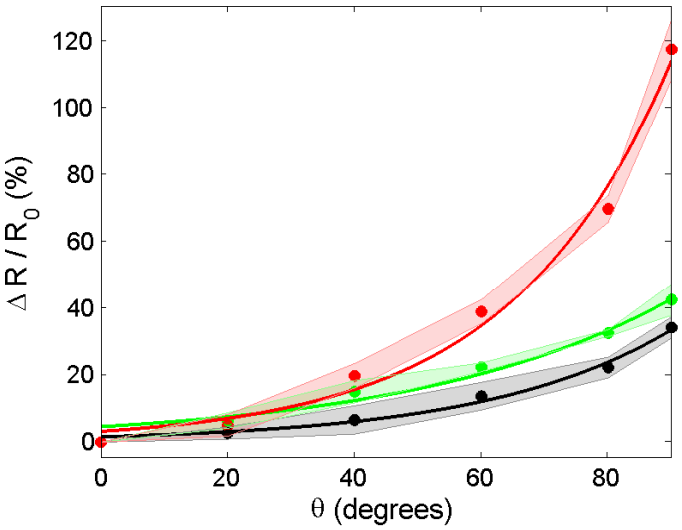

(b)

Figure 4.11: Calibration curves for three sensor geometries taken (a) independently of a host and (b) when mounted on a host finger. Green, black and red markers correspond to the strain sensor, curvature sensor and integrated geometry, respectively. Shaded error bars represent one standard deviation of the data. On-finger calibrations were conducted only in the configuration for which the layer containing the microchannel is in contact with the finger. Percent change in resistance is calculated based on the R_0 values given in Table 4.1 and is a function of channel geometry.

ing condition. Between 0° and 90° the sensor's resistance increases on average by about 8% (0.82 Ω to 0.885 Ω, nominally), while the integrated strain-curvature sensor increases by about 3% (1.1 Ω to 1.14 Ω, nominally). This is intuitive, given that the length of the channel deformed in the curvature sensor is greater than the cumulative length of the channel deformed in the combined strain-curvature sensor. In the combined geometry sensor, the strut is 0.5 mm in width and intersects the 1 mm wide channel at four discrete locations, resulting in an area of intersection between the strut and channel of 2 mm^2. In the pure curvature sensor, the strut intersects the entire length of the channel that it is aligned with, which in this case is 7 mm in length. Hence, the area of intersection for this sensor is 3.5 mm^2. The pure curvature sensor is therefore more sensitive under the given testing condition. Predictably, the pure strain sensor does not display a notable change in resistance. As the sensor is only 300 μm in thickness, differential strain is minimal in this condition.

Finger-Mounted Calibration

Each sensor geometry was also calibrated and tested on a host finger. The sensor was wrapped around the index finger with the sensing element placed above the middle knuckle. Sensors with struts were worn such that the film containing the microchannel was in contact with the skin. The base electrical resistance was determined by keeping the finger straight. The finger was then positioned at bending angles between 0° and 90°, and the change in resistance was recorded. The finger joint was orientated using the same calibration setup (angle wheel) as in the idealized case, shown in Figure 4.10. Lines of the 'angle wheel' were aligned with the top surface

of the finger. Finger-mounted curvature measurements were repeated five times for each sensor geometry, and are shown in Figure 4.11(b). The base resistance and the magnitude of the resistance change appear to be consistent for each sample tested. It is important to note that the exact relative change in resistance is not significant, as it should differ due to differences in the topology of the host manipulator or human finger. However, this analysis is useful in capturing general trends.

Interestingly, the combined strain-curvature sensor exhibits significantly enhanced sensitivity, especially as θ approaches 90°. The pure curvature sensor appears to be the least sensitive when integrated with a host finger, while the strain sensor seems to be slightly more sensitive than the curvature sensor. It is not immediately intuitive that the strain sensor should demonstrate this level of sensitivity. We hypothesize that the change in resistance observed is not due to differential strain, but rather that the knuckle exerts a pressure on the channels during bending, such that the channels are deformed locally around the knuckle as θ increases despite the absence of a strut. Thus, resistance across the channel increases exponentially with θ as increasing pressure is applied to the sensor. This effect applies to each of the geometries, and is supported by the order-of-magnitude increase in the scale of ΔR in Figures 4.11(a-b).

Exponential curves were fit to the data collected and are plotted in Figure 4.11(b). Data fitting was achieved using the MATLAB Curve Fitting Tool (*cftool*). Because it is known that ΔR is zero when θ is zero, the curves are manually adjusted to intersect the origin. That is, for a curve fitted in the form $\Delta R = Ae^{b\theta}$, the y-intercept is known to be A and the final fit is taken to be $\Delta R = A(e^{b\theta} - 1)$. Therefore, we find that:

$$\theta = \frac{1}{b} log \left(\frac{\Delta R + A}{A} \right). \tag{4.7}$$

This manual adjustment is necessary to avoid the term within the logarithm of Equation (4.7) evaluating to less than 1, resulting in negative finger joint angle values.

4.5.5 Experimental Setup

The electrical response of the wearable sensors is measured with a precision multimeter (Fluke 8845A) and recorded through a software interface (Flukeview Forms Basic). Video capture of finger movement is simultaneously recorded. During testing, a finger-cot (Qualatex XC) is worn over the host finger and sensor to maintain a close fit. Small markers (MoCap Solutions) are placed strategically on the side of the finger at the knuckle and each end of the bending joint. Video is subsequently analyzed with ProAnalyst (XCITEX motion analysis software), which tracks the three markers. Finally, relative marker positions are used to calculate finger joint angle throughout the testing period.

In each test, the finger bends to 90°, stays at 90° for a few seconds, and then straightens to 0°. Measurements are also taken for a rapid succession of bending and straightening, as well as partial bending (to approximately 45°). For sensor geometries containing a strut, the sensors are tested both with the layer containing the microchannel in contact with the finger and with the strut between the channel and finger.

4.5.6 Results and Discussion

A plot of actual angle and predicted angle is presented in Figure 4.12 for a series of finger bending motions. The actual joint angle is calculated based on motion analysis of video capture, and predicted joint angle is calculated based on the calibration curves derived from Figure 4.11(b) and Equation (4.7). From the top, the plots correspond to (a) a serpentine channel, (b) a straight channel with a strut on top (the layer containing the microchannel is in contact with the finger), and (c) a serpentine channel with a strut on top. The cases for which the layer containing the strut is in contact with the finger were also tested, but the results are omitted here due to decreased sensitivity of these configurations (discussed below).

As seen in Figure 4.12, predicted joint angles for the strain sensor tend to be over-estimated, while predicted joint angles for both the curvature and combined strain-curvature sensors appear to be roughly consistent with actual joint position. Table 4.1 displays the average (taken as root mean square) deviation of $\theta_{predicted}$ from θ_{actual} over the periods of motion shown in Fig. 4.12, as well as average error given as a percent of the full-scale output of 90°. Accuracy of the sensors is highly dependent on care taken during calibration. It should be noted that slight differences in the calibration curve may lead to drastic changes in joint angle prediction, predominately due to the nonlinear dependence of ΔR on θ. Error may also be induced by the y-intercept adjustment to the exponential curve during calibration curve fitting. Further explanation for discrepancies between actual and predicted angles may include error during motion tracking and analysis, as well as fluidic or viscoelastic changes in the sensor itself.

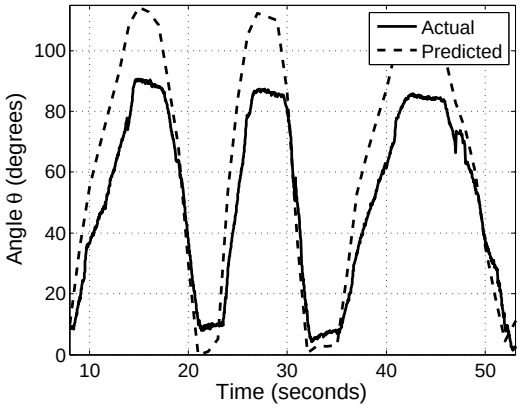

(a) - Strain Sensor

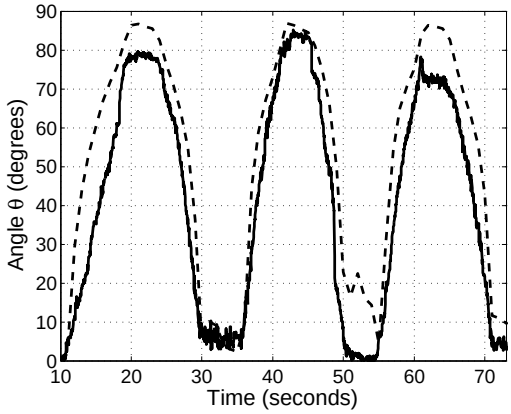

(b) - Curvature Sensor

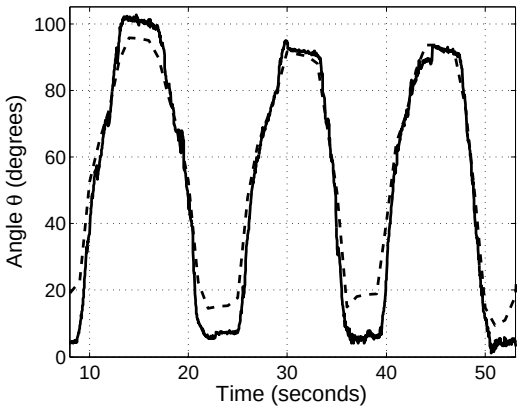

(c) - Combined Strain/Curvature Sensor

Figure 4.12: Actual angle and predicted angle for a series of finger bending motions. From top: (a) Strain sensor geometry. (b) Pure curvature sensor. The layer containing the microchannel is in contact with the finger. (c) Combined strain-curvature sensor. The layer containing the microchannel is in contact with the finger. Finger joint angles are predicted by the calibration curves derived in Fig. 4.11(b) and Equation (4.7).

Table 4.1: Summary of sensor performance.

	R_0 (Ω)	$R_0 + \Delta R$ @ 90° bend (Ω)	$r = \Delta R/R_0$	RMS $\theta_{actual} - \theta_{predicted}$	RMS % error
Strain Sensor	1.1	1.8	64%	18.79°	20.87%
Curvature Sensor (eGaIn-side down)	0.82	1.15	40%	13.75°	15.28%
Combined Sensor (eGaIn-side down)	1.1	2.5	127%	7.94°	8.82%
Curvature Sensor (eGaIn-side up)	0.82	0.9	10%	—	—
Combined Sensor (eGaIn-side up)	1.1	1.4	27%	—	—

Raw resistance data can be used to analyze the various sensor geometries and their relative sensitivities. In all cases, the relative change in electrical resistance $r = \Delta R/R_0$ is significant as the joint goes from straight to 90° bending. In one set of tests, the serpentine channel (absent of a strut) increases from approximately 1.1 to 1.8 Ω. This corresponds to a relative increase of approximately $r = 64\%$. A relative change of $r = 40\%$ (0.82 to 1.15 Ω) is observed for a sensor composed of two films, a strut, and a straight channel when the film containing the channel is in contact with the skin. Interestingly, the sensor is less sensitive when the film containing the sensor is on the outside. In this case, the resistance increases from 0.82 to 0.9 Ω, and so r is only 10%.

The greatest sensitivity is measured with a sensor that contains both the strut and serpentine geometry, which is consistent with the calibration results. When the film containing the microchannel is in contact with the skin, the resistance increases from 1.1 to 2.5 Ω and $r = 127\%$. When the film containing the channel is on the outside, the resistance only increases to 1.4 Ω and $r = 27\%$. These results are summarized in Table 4.1.

According to these measurements, the strut only appears to be effective when it is above the microchannel (i.e. the film containing the microchannel is in contact with the skin). Because the channel is small relative to the size of the strut, its position should have no influence on the compressive force exerted by the strut during bending. The only factor that changes is the way that this compressive force is distributed around the embedded channel. As demonstrated by the finite element analysis (COMSOL 4.0) presented in Figure 4.13, the stress on the outer film is concentrated at the corners of the junction and away from the center of the junction. In contrast, the stress on the inner film is distributed uniformly throughout the junction, including at the center where the microchannel would be embedded. In this analysis, the inner film has a thicker backing in order to simulate contact with the finger.

Alternatively, the sensors may be implemented as a binary switch, for which joint bending is detected when the relative change in resistance $r = \Delta R/R_0$ exceeds a critical threshold. This application eliminates the necessity for extensive sensor calibration.

4.6 Conclusions and Implications

This chapter presents a hyperelastic, soft microfluidic film that measures bending curvature using a novel non-differential mechanism. In contrast to conventional curvature sensors that use a strain sensor offset from the neutral axis, this elastomer-based solution allows for curvature sensing directly on the bending plane. Bending curvature κ is determined by measuring the change in electrical resistance ΔR of an embedded microchannel of conductive liquid. A closed-form algebraic estimate for the

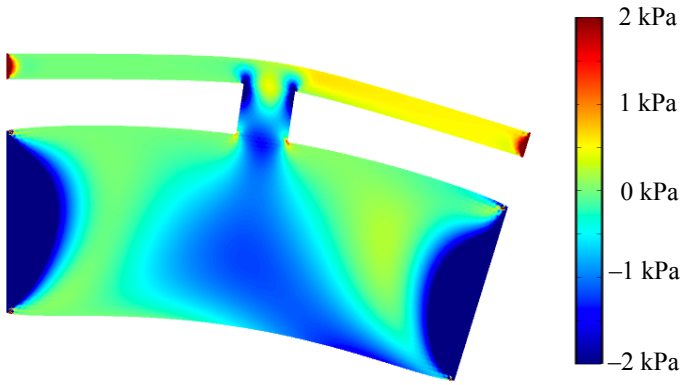

Figure 4.13: Finite element analysis (COMSOL) of pressure distribution in the curvature sensing device when loaded onto a finger. The inner film has a thicker backing in order to simulate contact with the finger. In this simulation, the sensor has an elastic modulus of 167 kPa, a Poisson's ratio of 0.45, a strut width of 2 mm, a gap height of 2 mm, and inner and outer plate thicknesses of 7 mm and 1 mm, respectively. The stress on the outer (thinner) film is concentrated at the corners of the junction and away from the center of the junction. The stress on the inner (thicker) film is distributed uniformly throughout the junction, including at the center where the microchannel would be embedded. This is consistent with results demonstrating increased sensor sensitivity when the film containing the microchannel is in contact with the finger.

relationship between ΔR and κ is derived from elastic plate theory. The theoretical predictions are in reasonable agreement with experimental measurements obtained for a variety of sensor geometries and materials.

As a demonstration, the elastomer sensor is wrapped around a finger with the sensing element positioned on top of the knuckle. When the finger bends, the knuckle both stretches the elastomer and exerts pressure on the embedded microchannel, and deformation of the cross-section of the microchannel leads to a change in electrical resistance. In addition, an embedded pressure-exerting strut, which operates on principles of plate bending, enhances the resistance change and sensitivity of the sensor. The sensor is soft (elastic modulus $E \sim 1$ MPa) and stretchable (>350%) without

losing functionality, and thus conforms to finger bending without restriction to the host. This sensor represents a flexible, stretchable and all-compliant solution for sensing bending angles, in contrast to many state-of-the-art technologies that feature rigid and motion restricting components. More classical rigid sensors may yield more accurate angle predictions, but at the expense of interference with the host.

Curvature sensing represents just one capability necessary to completely map the shape and deformation of an elastic body. Complete shape mapping can be accomplished by combining curvature sensors with strain [82] and pressure sensing (as discussed in Chapter 3). Since all of the sensing elements scale differently with stretch, curvature, and pressure, it is possible to decouple these values by comparing each sensor measurement ΔR. This may be done mathematically from the algebraic expressions for ΔR or graphically from the sensor response curves. The compliant sensors and fabrication technology used in this study may serve many functions in robotic electronics and sensing. For example, the sensors presented here may be applied to robotic hands for both monitoring hand movements and tactile sensing for object manipulation.

Chapter 5

Liquid-Embedded Elastomers as Stretchable Power Circuits

This chapter introduces liquid-embedded elastomers as stretchable power circuits, with integrated circuits and sensors fabricated in parallel. While high-resistance stretchable circuits may be acceptable for some applications, such as digital communication, they would not be appropriate for high current applications.

As a demonstration of liquid-embedded elastomer electronics, an integrated circuit is employed in a two-tile origami module (which requires stretchable electronics at the folding axis) actuated by a shape memory alloy (SMA) actuator [113] (which requires relatively large currents). To see how the liquid-embedded elastomer circuit compares to a conventional stretchable electronics approach, it is compared directly to meshed copper traces. Both circuit designs maintain conductivity even at large strains (during stretching) and curvatures (during folding).

5.1 Related Work in Flexible Electronics and Circuits

Previous chapters in this thesis have discussed the stretchable electronics work done by Rogers' group, which use patterned thin silicon nanoribbons and membranes to introduce flexibility in a silicon substrate or thin metal film [114, 115]. However, since these techniques rely on integrated circuit fabrication, scaling up beyond a few tens of centimeters may be challenging.

In addition, there has been work with printable electronics using carbon nanotubes and various nanowires made of semiconductors. Printable circuits on flexible polymers and materials, such as paper, have also been presented [116]. However, the impact of wire diameter, doping level, surface treatment, contact metal, and substrate material is vital to the design and operation of devices and may limit the scope of applications [117]. Also, in comparison to metals, semiconductors are far less conductive (electrical resistivity differing by nine orders of magnitude). For transistors and memory chips, the lower conductivity of semiconductors is not critical; but for a circuit path that requires high current densities, this could limit the applicability.

5.2 Two Stretchable Circuit Designs

Two flexible circuit designs are employed here to power SMA actuated modules. These circuit designs do not require a clean room nor extensive fabrication processes, yet display high electrical conductivity while undergoing high strains. Each technique results in a circuit a with low profile (sub-millimeter) that may be "printed" as an

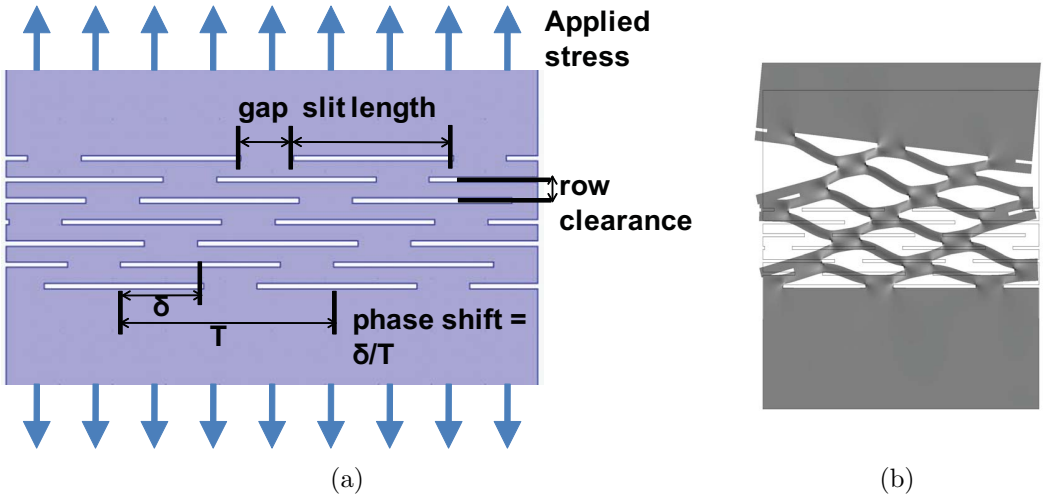

Figure 5.1: Description of slit design parameters (a), COMSOL model of a deformed slit (b). Figures contributed by Professor Jamie Paik.

independent circuit layer onto the substrate.

5.2.1 Copper-Mesh Circuit

A conventional approach to stretchable electronics involves creating a transversely deformable pattern in a metal trace. We begin with a copper/polyimide composite (40 μm thick copper and 30 μm thick polyimide) used for conventional flex-circuit fabrication. A mesh pattern is introduced to the sections of the traces that experience strain. This pattern is made of slits orthogonal to the long axis of the trace, and stacked with variable overlap along the trace direction (Figure 5.1(a)).

A finite element model in COMSOL was used to optimize the copper mesh geometry for high strains. Figure 5.1(b) shows a representation of a deformed shape. Based on this model, a geometry with a slit pattern with a 75% phase shift, 40 μm row clearance, 100 μm gap, and 300 μm slit, was chosen for experiments.

Copper mesh circuits are fabricated from a polyimide/copper laminate (DuPont).

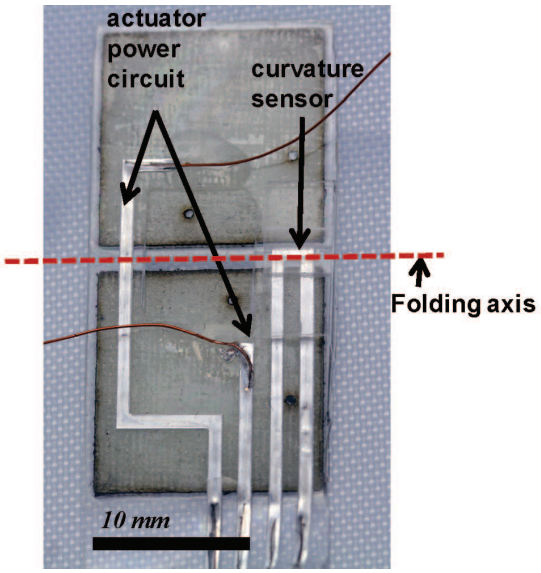

Figure 5.2: Fully integrated stretchable electronics on a origami tile module: eGaIn-filled circuitry and a curvature sensor.

Circuit traces are achieved by patterning the copper via a photolithography process followed by a ferric chloride etch. The circuit is then laser machined (diode-pumped solid state (DPSS) laser) to ablate polyimide in mesh-sections of the traces that will experience axial strain. Note that this section includes work contributed by Professor Jamie Paik.

5.2.2 Liquid-Embedded Elastomer Circuit

Liquid-embedded elastomer circuits are composed of thin sheets of polydimethylsiloxane (PDMS) silicone rubber embedded with conductive liquid microchannels of non-toxic eutectic gallium-indium (eGaIn). The circuits are made using the mold-fabrication process given in §3.2.4 and the replica molding process previously described in §3.2.5.

The flexible eGaIn circuit shown in Figure 5.2 is approximately 300 μm in total

thickness. The elasticity of the circuit may be tuned by choice of material. For example, PDMS has an elastic modulus of 1-2 MPa, while EcoFlex® silicon rubber (0030, SmoothOn) is considerably more elastic with a Young's modulus close to 125 kPa.

5.3 Module Integration

Square tiles are made of resin cured glass-fiber that is layered to have a cured thickness of 300 μm. The copper-mesh circuit is adhered to the tile module via encapsulation in a thermoplastic polyurethane (76 μm American Polyfilm 70 shore A, polyether polyurethane)(140°C for 30 min), which also encases the copper mesh and simultaneously introduces an elastic material between the tiles. The surfaces of the liquid-embedded elastomer circuits and the s-glass tiles are bonded together through an amino-epoxy chemical bonding method previously given in §4.5.3. Integration of the actuator module and completed tiles is accomplished mechanically using miniature bolts with a thread diameter of 0.5 mm. The excess length of the bolt is trimmed and thread-locked using cyanoacrylate (Loctite 416). The electrical connection of the ends are soldered to either to the electrode pads of the copper circuit (exposed sections in the polyurethane) or to the wire outlets of the eGaIn circuit.

Figure 5.3 shows the completely integrated stretchable circuits of both copper-mesh design and liquid-embedded elastomer design. For the liquid-embedded elastomer circuit, note the soft curvature sensor alongside the actuator.

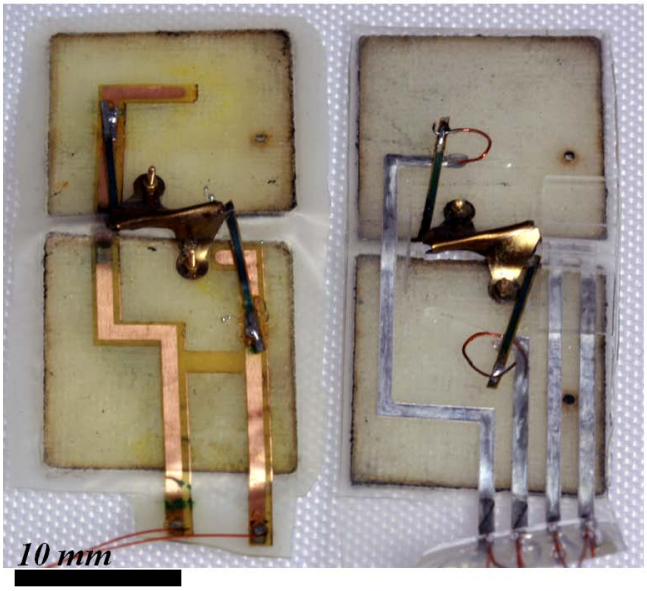

Figure 5.3: Two flexible circuits integrated with origami tile modules. The left shows the copper-mesh circuit and the right is the eGaIn circuit. Both circuits have trace widths of $1mm$. For the eGaIn circuit, the curvature sensor is embedded to the right of the actuator. The copper-mesh circuit was constructed by Professor Jamie Paik.

5.4 Power Circuit Performance Metrics

The prototyped stretchable circuits were tested for maximum operating strain and the ability to transfer power to the actuators during folding of the tiles.

Circuit traces were strained with an Instron Materials Testing System (model 5544A) in tensile extension mode while observing both electrical and mechanical failure (see Figure 5.4). Five samples of each circuit design were wired to a multimeter to measure conductivity and electrical resistance while being stretched to failure. Copper-mesh samples (traces 1 mm wide, 0.075 mm thick) failed on average under 56% strain at a corresponding 3.02 N load. When the copper-mesh trace width changed to 1.5 mm, the strain at failure increased to 100%. The liquid-embedded elastomer samples with traces 1 mm wide had an average of 162% strain-at-failure

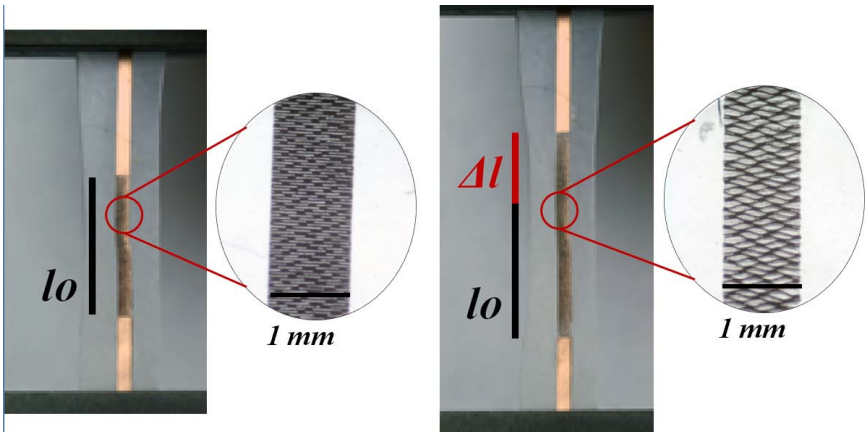

Figure 5.4: A sample of the polyurethane covered copper-mesh circuit placed in an Instron Material Testing system. The insets show the magnified views of the mesh that is in the neutral position (left image), and elongated to the point of failure (right image). Figure contributed by Professor Jamie Paik.

under 17.6 N loading. Here, failure is defined as either mechanical fracture or electrical open circuit. Both stretchable circuit types displayed continuous conductivity until mechanical fracture. The copper-mesh circuit failed when the meshing broke completely within the polyurethane covering; with a finer mesh design or a wider section, the copper-mesh circuit could potentially endure greater strains. The eGaIn circuit maintained conductivity until the PDMS structure and channel failed (ruptured) mechanically. The copper-mesh circuit maintained a relatively constant electrical resistivity during elongation (from 0.22Ω to 0.24Ω) while the liquid-embedded elastomer circuit experiences a greater resistance change before it fails (from 0.67Ω to 1.08Ω).

To evaluate the functionality of both trace types for actuator power circuits, the devices shown in Figure 5.3 were actuated while observing folding range, time to fold, and power consumption. Both the copper-mesh circuit and the liquid-embedded elastomer circuit displayed similar responses to folding actuation, but the liquid-

Table 5.1: Performance Comparison for Copper-mesh and eGaIn Circuits.

	Copper-mesh circuit	eGaIn circuit
Range of motion	0-180°	0-180°
Mass (without tiles)	0.063 g	0.065 g
Actuation time constant	$\approx$ 1 s	$\approx$ 1 s
Power consumption (no load)	0.092 W	0.187 W
Strain to failure	56%	162%
Trace resistivity change	0.22Ω - 0.24Ω	0.67Ω - 1.08Ω

embedded elastomer circuit required more power (see Table 5.1). This larger power consumption is due to the more resistive circuit path. The copper and eGaIn-filled circuits have similar dimensions (i.e. same channel width, with 40 μm thick copper and 50 μm deep eGaIn channel). However, because copper is 20 times more conductive than eGaIn [85], higher I^2R losses are present in the eGaIn circuit path. Also, due to the flexible nature of the channel material, the channel geometry changes increase the circuit resistance when stretched. This property is exploited for strain, pressure, and curvature sensing (as discussed previously in Chapters 3 & 4).

5.5 Integrated Electronics: Power Circuits and Sensors

A compliant curvature sensor similar to that described in Chapter 4 is integrated with the folding module to measure deflection angle when actuated by the SMA actuator. Characterization and calibration of the sensor is necessary and conducted prior to use. To calibrate, pure bending of the sensor is induced by positioning the two s-glass tiles at specific angles. During testing, the tiles are attached to rigid

Figure 5.5: Folding sequence of the origami module powered with the eGaIn circuit. The integrated soft curvature sensor measures the angular deflection by detecting the change in resistance, given in Ohms.

blocks to increase positioning accuracy and eliminate any twisting or stretching of the sensor. The tiles are manually oriented from 0° to 170°, and the change in electrical resistance is measured with a precision multimeter (Fluke 8845A). As expected, the change in electrical resistance ΔR increases exponentially as a function of bending angle θ. Curvature measurements are repeated 5 times, and the data is averaged and fitted to an exponential curve.

A comparison between actual angle and sensor-measured angle during actuation of the joint for a typical folding sequence is shown in Figure 5.6. Actual angle is determined via motion tracking using ProAnalyst (XCITEX) software. The predicted angle is determined by calibration and the exponential curve fit to this particular sensor. The data in Figure 5.6 was collected over five folding sequences and the shaded error bar represents one standard deviation of the data. The average standard deviation of the data is 4.41°. The quadratic mean difference between actual and predicted angle is 15.36°. The average error of the sensor is 8.53%, as given as a

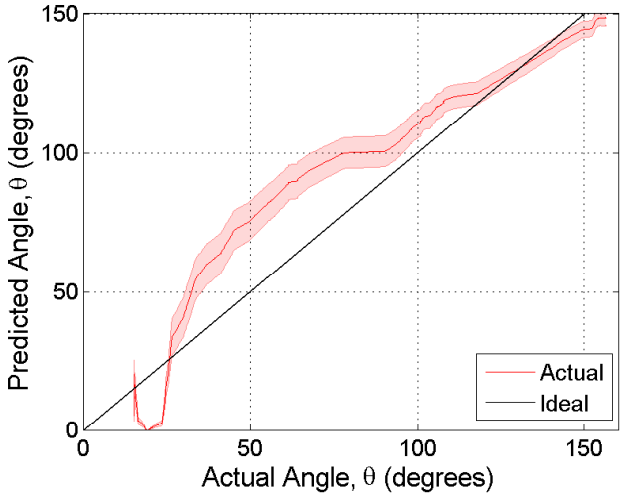

Figure 5.6: A comparison between actual angle and predicted angle, based on compliant curvature sensor measurements taken over five folding sequences. The shaded error bar represents one standard deviation of the data.

percent of the full-scale output of 180°.

For moderate to low bending angles, there appears to be some discrepancy. This is somewhat expected, due to the non-linear relationship between change in resistance and bending angle. Small changes in resistance may therefore translate into large fluctuations in predicted angle. However, small variations in resistance may be induced by factors other than bending, such as motion of the wires that connect the liquid microchannels to the multimeter.

Chapter 6

Selective Wetting of Gallium-Indium Alloys for Liquid-Embedded Elastomer Electronics

The use of liquid-embedded elastomers in soft sensing technologies as been discussed (soft pressure sensors in Chapter 3, soft curvature and angle sensors in Chapter 4). Liquid-embedded elastomers have also been investigated as power circuits (Chapter 5). This chapter now looks to the future of liquid-embedded elastomer electronics, which will require new fabrication techniques for miniaturized and integrated electronics.

6.1 Soft Electronics for the Future

The development of soft and stretchable electronic devices parallels with the natural evolution and miniaturization of electronics. Beginning in the 1950's with the invention of the integrated circuit [118], each succeeding decade has presented a new host of challenges to accommodate the changing demands for complex deformation and adaptability of machines. The 1970's brought about new understanding of semiconductor microelectronics processing [119], while the 1980's marked the advent of MEMS and positioned silicon as the primary material [120]. Development of bulk [119] and surface [121] micromachining processes allowed progress toward the production of dynamic micromechanical structures [122] for MEMS devices and electronics. In the late 1990's, the idea of microfluidics was first introduced, with the assumption that photolithography and associated technologies that had found success in silicon microelectronics development would be directly transferable to microfluidic device fabrication. At the onset of the millennium, traditional materials such as silicon and glass were displaced by polymers, particularly PDMS (poly(dimethylsiloxane)) for microfluidics [123, 124, 94]. Now that microelectronics and soft microfluidics are well established, soft and stretchable microelectronics represent the next stage in the technological evolution towards soft active materials.

Recent interest in highly deformable mechanical systems, such as soft robots [2, 3], has provided motivation for highly deformable electronic components, such as flexible and stretchable sensors and circuits. There are established fabrication techniques for flexible circuits, such as printed circuit boards (PCB) based on thin dielectric films (polyester, polyimide, polyethylene naphthalate, and polyetherimide [125]). However,

existing PCBs and flexible sensors (such as Bi-Flex Sensors™, Bend Sensor®, and Flexiforce® Sensors) are flexible, but not soft or stretchable.

The grand challenge, therefore, lies in engineering soft and stretchable conductors that remain conductive over large strains (>100%) and with feature sizes and densities comparable to PCB techniques (minimum trace width and edge-to-edge trace separation is about 50 μm, but typical manufacturers of PCBs use a trace width between 100-200 μm [126]). Thus far, there have been two main approaches to this problem: (1) Patterning of waves and nets into conductive thin films on stretchable substrates, and (2) embedding conductive liquid in stretchable materials.

In the first case, thin films of brittle materials can be fabricated into wavy layouts, where the amplitudes and wavelengths of conductive leads can change in response to applied loads [115, 63, 127, 128]. Similarly, conductive paths may be machined to create mesh shaped ribbons, which also allows for passive compensation when the substrate is being strained (as in §5.2.1). Though typically limited to 50-100% strains, this versatile approach allows stretchable functionality with a broad range of thin-film metals, semiconductors, and polymers.

Liquid-embedded-elastomer electronics (LE3) have presented a promising solution to the need for all-soft (no rigid elements), flexible, and stretchable (100-1000%) electronics. Liquid-embedded-elastomer devices have been employed in applications such as pressure sensitive artificial skin (§3.5), proprioceptive motion feedback (§4.5), and electronics (§5.2.2). Because the sensors and electronics are soft and stretchable, they may conform to a host without interfering with the natural mechanics of motion. In addition, maximum strains in these devices are defined by the elastomer material

properties, rather than the patterned geometry of brittle elements. For example, compatible elastomers such as PDMS (Dow Corning) and Ecoflex (Smooth-On) may achieve strains of 200% and 1000%, respectively.

Throughout this thesis, LE3 technologies have been fabricated using microfluidic techniques and manual steps including molding, plasma bonding, and filling microchannels with syringe dispensers. Molds are generally produced using standard photolithography or 3D printed parts. However, these fabrication methods introduce limitations to both the design (features sizes and densities) and overall dimensions of devices. Now that simple sensor networks have been demonstrated, it is necessary to move towards more complex sensors and skins that require new batch microfabrication processes.

In this chapter, the first results from a new fabrication approach for liquid-embedded elastomer devices are presented. This fabrication technique, which is based on selective wetting of gallium-indium alloys, yields the ability to pattern highly conductive liquid metals within elastomer films without the need for molding, manual bonding, or manual injection of liquid. This processing technique exploits wetting properties and phase change of gallium-indium alloys, and culminates in the production of a liquid-embedded elastomer with isolated features smaller than 200 μm and edge-to-edge feature separations as small as 25 μm.

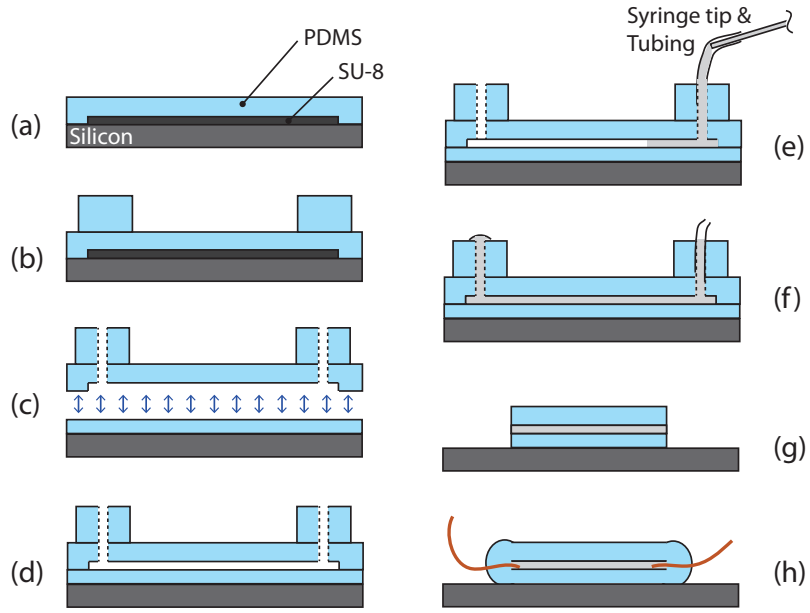

Figure 6.1: Process flow for liquid-embedded elastomers fabricated by standard soft lithography. (a) Elastomer is spin-coated and heat-cured on an SU-8/silicon mold. (b) Blocks of PDMS must be adhered to the inlet and outlet locations. (c-d) Holes are introduced at the inlet and outlet locations, and the patterned elastomer layer is oxygen plasma bonded to an unpatterned layer to form embedded microchannels. (e-f) Microchannels are filled manually with conductive fluid with tubing and syringes. (g) Inlet and outlets are manually cut off. (h) Wires are inserted into the channel ends and sealed with a droplet of uncured elastomer.

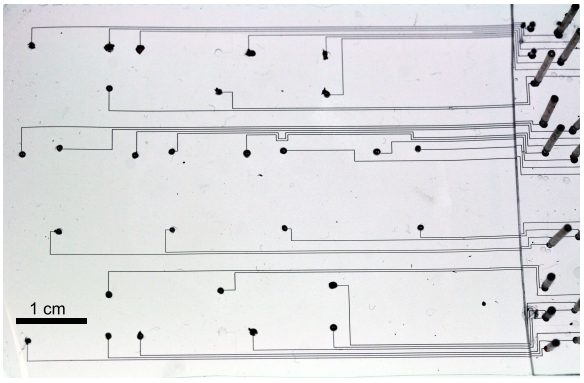

Figure 6.2: A liquid-embedded-elastomer circuit produced by the traditional fabrication method. Inlet and outlets for manual filling of pre-patterned microchannels can be easily identified. Channel traces are 50 μm in width and spaced 250 μm apart (edge-to-edge).

6.2 Fabrication

6.2.1 Previous Fabrication Methods

Previous fabrication efforts towards liquid-embedded-elastomer devices have been outlined throughout this thesis (see §3.2, §3.5.1), and are summarized in Figure 6.1. Generally, layers of elastomer are patterned via casting and curing on molds and subsequently bonded together using oxygen plasma. Embedded microchannels are manually filled with conductive liquid using tubing and syringes, by either applying positive pressure at the inlet or negative pressure at the outlet, and the microchannels are sealed by application of uncured elastomer.

Previous fabrication methods limit the geometries and scale achievable for liquid-embedded-elastomer electronics. Due to the high surface tension and viscosity of gallium-indium alloys (see Table 6.1), the pressure required to manually inject the conductive liquid into a microchannel may easily exceed the bond strength between layers of elastomer, resulting in de-lamination and failure in device fabrication. This is compounded by the significant variability in oxygen plasma bond strength, reported to range between 180 kPa - 715 kPa, and averaging around 300 kPa [129]. Intuitively, the smaller the microchannels, the more pressure that is required to fill the microchannels, and thus the greater the risk for fabrication failure. Trace density may also impact this process, as densely-packed traces means less area contact between the bonded layers, resulting in a lower overall bond strength between the layers. Manual filling of relatively small microchannels has been achieved, for example 50 μm $\times$ 20 μm as shown in Figure 6.2 or 20 μm $\times$ 40 μm as shown in [85]. However, we feel that

this method of fabrication is unreliable, with low production yield (<50%) and with many opportunities for human error. The nature of the fabrication method itself discourages miniaturization of traces and edge-to-edge feature separations. In addition, this method requires a discrete inlet and outlet location for each conductive trace, eliminating potential devices that require isolated features, such as electromagnets.

6.2.2 Patterning by Selective Wetting

The new fabrication technique exploits the surface free energy of various materials, chemistry and texture to control the interfacial free energy at the liquid metal-elastomer interface, and phase change of the liquid metal to control feature cross-section during encapsulation. The process ultimately generates an all-soft liquid-embedded-elastomer.

Fabrication of liquid-embedded-elastomer devices begins with vapor deposition of a hydrophobic monolayer on a flat substrate. In this work, we use clean glass slides (Electron Microscopy Sciences). The glass slides are placed in an evacuated chamber (∼20 mTorr) with an open vessel containing a few drops of Trichloro(1H,1H,2H,2H-perfluorooctyl)silane (Sigma Aldrich) for ≥3 hours. Subsequently, a layer of elastomer is spin-coated in liquid form onto the glass slide, yielding a thin film of tunable thickness. Here, we use PDMS (Sylgard 184, Dow Corning; 10:1 mass ratio of elastomer base to curing agent), however, subsequent steps in the process hold no dependency on the specific properties of PDMS and any thus any elastomer may be used.

After curing the elastomer layer, a 20 μm thick film of tin foil (Sigma Aldrich, product nu. 14511, pure) is rolled over the elastomer. The inherent tackiness of

PDMS allows for good adhesion between the elastomer and foil layers. In cases where a less tacky elastomer is used, adhesion between the layers may be achieved using the amino-epoxy chemical bonding method given in §4.5.3.

The foil is fully cleaned with acetone, IPA, and deionized water, and subsequently baked on a hotplate at 85°C for 5 minutes to evaporate liquids. A superhydrophobic photosensitive nanocomposite film is then spin-coated onto the surface. The superhydrophobic photoresist incorporates PTFE nanoparticles (Microdispers-200, Polysciences) into a positive photoresist matrix (1:15 ratio by weight, well-mixed with a centrifugal mixer). Experiments were completed using Photoposit SP24 (Shipley), which is a positive working resist generally used within the printed circuit board industry. Photoposit SP24 is also known to be a flexible photoresist, thus it is particularly well-suited to flexible circuit applications. In addition, we chose this resist due to its associated fine line resolution (1:1 resist thickness to resist geometries can be achieved, and etched dimensions of 1 mil can be produced). As no specific sensitivity chart was available from the resist manufacturer, we adapted the i-line compatible exposure process initiated by Corbett, et al in [130]. Photoresist is spun onto the tin foil at 800 RPM for 20 seconds. After spin coating, the sample is soft-baked on a hotplate at 85°C for 10 min. The photoresist is then exposed under a mask with a collimated UV source with an exposure energy of 2140 mJ/cm^2. The sample is then developed in an aqueous solution of (0.2N) sodium hydroxide at room temperature. Post-development, exposed tin is chemically etched in a heated ferric chloride bath, where the photoresist masks the desired tin pattern from removal. Residual ferric chloride is removed by rinsing the sample in deionized water, and the remaining tin

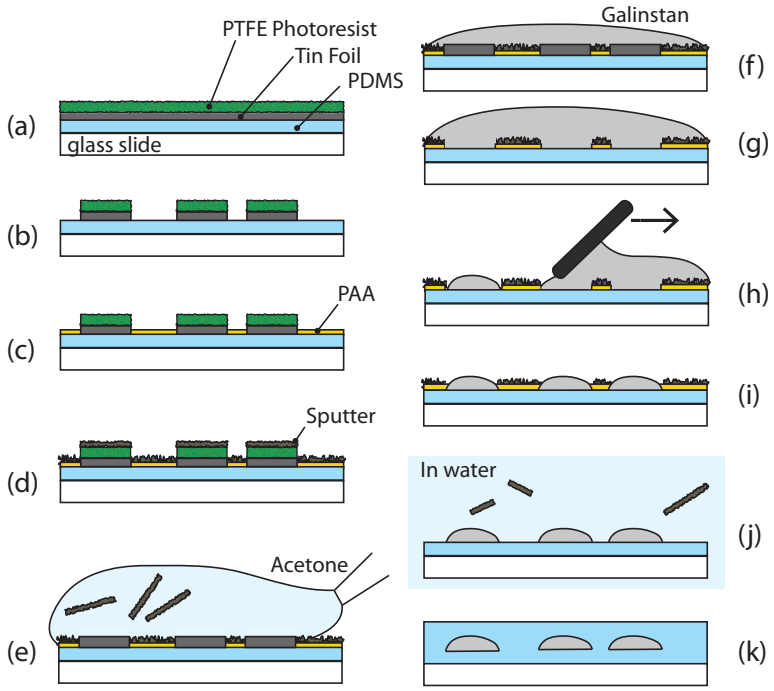

Figure 6.3: Process flow for liquid-embedded elastomers fabricated by selective wetting of gallium-indium alloys. (a-b) Tin foil is patterned on a PDMS surface with photolithography. (c) A PAA release layer is spin-coated onto the elastomer surface, and does not coat the super-hydrophobic photoresist. (d-e) The surface is sputter-coated, but the tin foil is protected by the photoresist. Lift-off is achieved by rinsing the surface with acetone. (f-g) The surface is flooded with Galinstan, which reactively wets to the tin foil. (h-i) Excess Galinstan is removed by wiping the surface with a thin-film applicator. (j) Remaining sputter is removed from the surface in water, using the PAA as a release layer. (k) The liquid features are encapsulated in a sheet of elastomer.

foil pattern acts as a seed layer for liquid metal deposition in later steps.

The sample surface is then exposed to oxygen plasma (65 watts for 30 sec). Silicon-based elastomers, such as PDMS, that have recently been exposed to an oxygen plasma are rendered hydrophilic by the formation of hydroxyl groups on the surface. Yet, the plasma exposure has no notable effect on the PTFE/photoresist surface, which is hydrophobic. Hence, a solution of poly(acrylic acid) (PAA) (Polysciences, Cat nu. 00627) diluted in deionized water (10% PAA by volume) is applied to the

entire surface, wherein the solution selectively wets the elastomer. The PAA solution is spin-coated at 800 RPM for 30 seconds to yield a thin liquid film on the elastomer surface. It should be noted that the PAA solution must be spin coated to a thickness that is less than the seed tin layer thickness to ensure good contact between the liquid metal and the seed layer in subsequent steps, due to the liquid metal's high surface tension. The sample is then baked on a hotplate at 85°C for several minutes, to evaporate solvents in the PAA solution. Finally, the sample is sputter coated with indium for 2 minutes. The sputtered indium layer acts as a repellent layer for the subsequent deposition of eutectic liquid metal, the details of which are addressed in the next section of this chapter.

Next, the sample is rinsed with acetone to lift off the photoresist layer and corresponding sputter-coated indium, thus exposing the underlying tin foil. The tin-patterned surface is then coated in galinstan, a eutectic liquid metal composed of 68.5% gallium, 21.5% indium, 10% tin, and trace amounts of copper. The sample is then kept in a nitrogen environment chamber for at least 24 hours, while the galinstan reactively wets to the tin foil substrate. The nitrogen environment prevents the galinstan from heavily oxidizing, while the patterned sputter-coated indium behaves as a mask, preventing non-uniform wetting of the elastomer surface.

When the sample is removed from the nitrogen environment chamber, galinstan that is not wetted to the surface is removed using a thin-film applicator (Elcometer 4340 Automatic Film Applicator). The thin-film applicator allows for definition of the liquid height, thus enabling some control over the cross-section of the liquid-embedded pattern. Any residual liquid metal is striped by placing the entire sample

in a deionized water bath, where the poly(acrylic acid) on the surface of the elastomer will be etched and result in lift-off of the corresponding sputter-coated layer and undesired liquid metal from the surface.

Finally, the sample is placed on a hotplate for several minutes to evaporate remaining solvents, and then placed into a freezer with an operating temperature below the melting temperature of galinstan ($-19\,^{\circ}\mathrm{C}$), which will cause the galinstan to harden and hold its form. This phase-change enables the cross-section of the liquid pattern to remain in tact during the subsequent encapsulation step. The liquid patterns are embedded into an elastomeric matrix by spin coating a final layer of elastomer over the entire surface of the device, followed by a cure step. The liquid-embedded-elastomer device may then be released from the glass slide substrate. The fabrication process flow is outlined in Figure 6.3.

6.3 Wetting Behavior of Gallium-Indium Droplets

The success of the proposed fabrication process relies heavily on the ability to selectively pattern conductive liquid metals, and thus is directly dependent on the surface free energy of various materials. In this study, two liquid metals were investigated: eutectic gallium-indium (eGaIn) and galinstan. These eutectic liquids were chosen for their low melting temperatures and high conductivities [131, 85, 132] in comparison with other conductive liquids, such as ionic liquids (for example, 1-ethyl-3methylimizodalium ethyl sulfate has an electrical resistivity of 2.51 Ωm [72]). Table 6.1 provides a summary of selected properties pertaining to these materials.

In this work, we tested the interfacial free energy between various surfaces and

Table 6.1: Summary of Eutectic Liquid Metal Properties.

	Eutectic Gallium-Indium	Galinstan
Composition	75% Ga, 25% In	68.5% Ga, 21.5% In, 10% Sn
Melting Point	15.5 °C	−19 °C
Bulk Viscosity	$1.99 \times 10^{-3} Pa \cdot s$	$2.4 \times 10^{-3} Pa \cdot s$
Electrical Resistivity	$2.94 \times 10^{-7} \Omega m$	$2.89 \times 10^{-7} \Omega m$
Surface Tension	624 mN/m	718 mN/m

the eutectic liquid metals by measuring the contact angle of a liquid metal droplet as a function of time. Because there is a large number of material combinations and processes to alter the surface energy of materials, we focused on materials and processes common to soft microfluidics, as well as materials present in the eutectic liquid metals, such as indium and tin. We chose to experiment with indium and tin substrates because it is intuitive that a liquid metal would have an affinity for wetting to materials present within itself.

Throughout the experimental phase of this work, it became clear that wetting between the liquid metals and a surface demonstrates one of four distinct outcomes: (1) a high contact angle with no wetting (2) a high contact angle, but the ability to non-uniformly stain a surface, (3) inert wetting, and (4) reactive wetting. To clarify, we will define inert wetting as a dynamic response that leaves the solid-liquid interface materially and morphologically unchanged. However, during reactive wetting, the solid-liquid interface undergoes complex material and morphological changes. Examples of several of these outcomes are shown in Figure 6.4.

Firstly, we found that both gallium-indium alloys tested did not wet to a PDMS (silicon-based elastomer) surface, but rather non-uniformly stained the surface with a contact angle of $\approx 130\,°$. This is consistent with other reports of non-wetting between

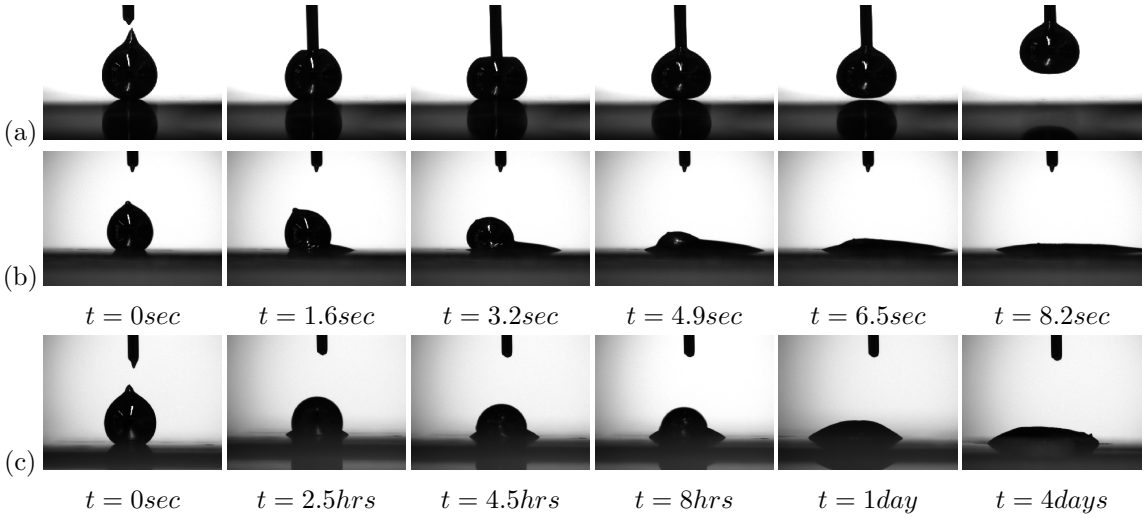

Figure 6.4: (a) A eutectic gallium-indium droplet on a surface of indium foil (100 μm thick) that has been sputter coated with indium for 2 minutes. The droplet does not wet to the surface at all. (b) A eutectic gallium-indium droplet on a surface of indium foil (100 μm thick). The droplet wets the surface within seconds and immediately upon contact, demonstrating inert wetting. (c) A galinstan droplet on a surface of tin foil (20 μm thick). The droplet wets the surface slowly over a period of days, demonstrating reactive wetting.

gallium-indium alloys and PDMS [85]. For completeness, we also tested contact angle between the alloys and a PDMS substrate with recent exposure to oxygen plasma. Unlike for water-based liquids, this surface treatment did not notably the change the wettability of the substrate for gallium-indium alloys (contact angle $\approx 125\,^{\circ}$).

Interestingly, the wetting response was highly variable across metallic surfaces as a function of both material and texture. As seen in Figure 6.4(b), inert wetting occurs between eutectic gallium-indium and indium foil (Sigma Aldrich, product no. 357308, 99.999% pure). However, sputter coating the foil with additional indium renders the surface repellent to eutectic gallium-indium (sputter target from American Elements, 99.999% pure), as seen in Figure 6.4(a). Similarly, galinstan wets reactively to tin foil (Sigma Aldrich, product nu. 14511, pure) (Figure 6.4(c)), but is repelled by sputter

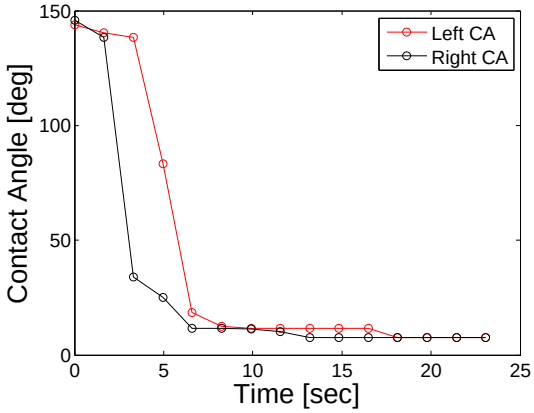

(a)

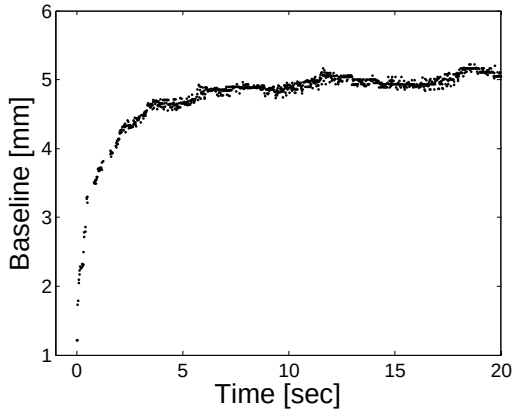

(b)

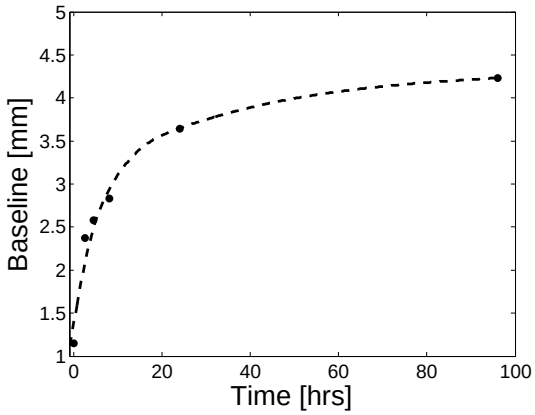

(c)

Figure 6.5: (a) Dynamic contact angle and (b) baseline length of eutectic gallium-indium as it wets to an indium foil substrate in a typical experiment (shown in Figure 6.4(b)). The droplet comes into contact with the foil surface at time = 0. (c) Baseline length of galinstan reactively wetting to tin foil in a typical experiment (shown in Figure 6.4(c)).

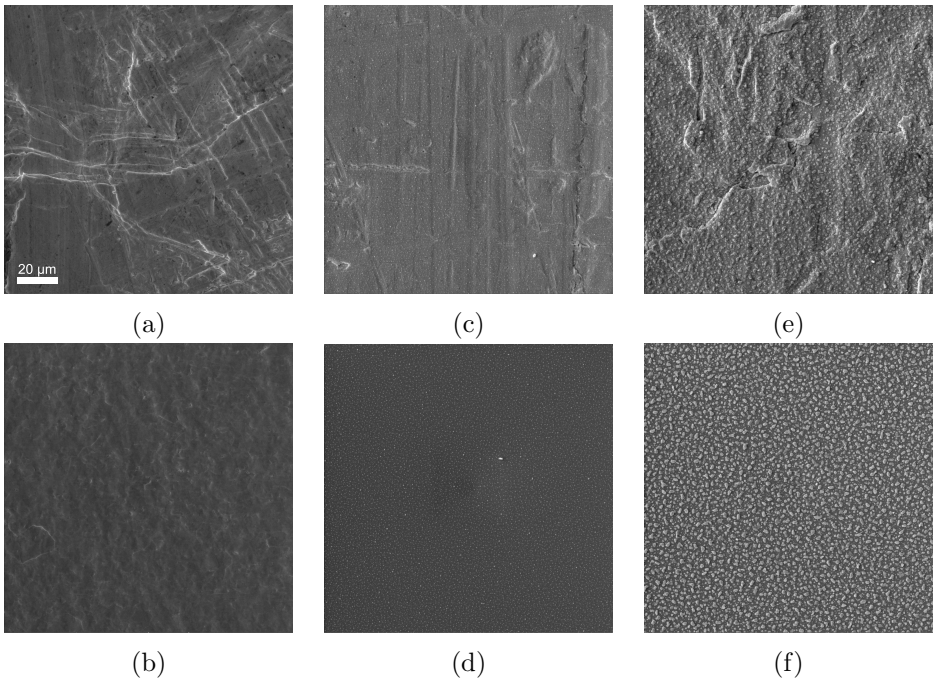

Figure 6.6: SEM images of indium and tin surfaces under various manufacturing conditions. (a) Indium foil, 100 μm thick. (b) Tin foil, 20 μm thick. (c) Indium foil (100 μm thick) sputtered with Indium for 2 minutes. (d) A silicon wafer sputtered with indium for 2 minutes. (e) Indium foil (100 μm thick) sputtered with indium for 10 minutes. (d) A silicon wafer sputtered with indium for 10 minutes.

coated films of tin (sputter target from American Elements, 99.999% pure).

As the materials appear to be identical in purity, variations in wetting properties may be a result of differences in texture between the substrate materials. Scanning Electron Microscope images yield some insight into the surface differences. The following surfaces are shown in Figure 6.6: 100 μm thick indium foil, 20 μm thick tin foil, 100 μm thick indium foil sputtered with indium for 2 minutes, 100 μm thick indium foil sputtered with indium for 10 minutes, and indium sputtered on a silicon wafer for 2 and 10 minutes.

We begin by discussing the behavior of eutectic gallium-indium (eGaIn) on these substrates. As previously revealed, eGaIn inertly wets to thick (100 μm) indium foil.

In addition, eGaIn reactively wets to relatively thick (127 μm) tin foil. Interestingly, eGaIn stains, but does not wet, thin (20 μm) tin foil. Additionally, eGaIn is entirely repelled from both indium and tin sputter coated surfaces. It may be inferred that the surface free energies of rolled indium foils and eGaIn are a desirable combination to achieve inert wetting. However, over a long period of time ($\geq$3 hrs), the liquid diffuses into the foil and initiates stress fractures at the grain boundaries, a phenomenon called constitutional liquation that results in many small, brittle chunks of indium, as shown in Figure 6.7. Hence, it should be noted that wetting of eGaIn on indium foil is a two step process in which the liquid first wets inertly (t $<$ 30 sec), than diffuses the foil at the grain boundaries (30 sec $<$ t $<$ 3 hrs).

In addition, although eGaIn is a stable eutectic liquid, it is not surprising that when brought into contact with a tin substrate the materials may react to form an alloy of a composition similar to galinstan. However, over a long time period ($\sim$hrs), we once again see the results of constitutional liquation, wherein the foil is fractured at the grain boundaries and broken into brittle chunks. The importance of this outcome lies in the eventual liquid-embedded-elastomer device functionality; that is, the embedded seed layer for selective wetting of conductive liquid must impart negligible stiffness to the final device and must not introduce any rigid components that may inhibit stretchability.

Given the reaction between eGaIn and foils of indium and tin, it is not intuitive that thin sputter coated films should repel the eutectic liquid. As seen in Figure 6.6, deposition by sputtering yields a film with relatively high surface roughness, and this effect appears to be exacerbated with longer sputter times. One possible explanation

is that sputtering introduces a surface texture that results in the repellent behavior, as many studies have shown that texturing a surface may render the surface hydrophobic [133]. It was briefly considered that a surface oxide may be preventing inert or reactive wetting with sputtered layers, however it is unlikely that indium will oxidize at low temperatures (sputtering occurred in an argon environment), and sputtered samples did not show the characteristic yellow hue of indium oxide. To be thorough, we conducted several experiments wherein any potential oxide was removed with a flux cleaning agent, which was found to have no effect on eGaIn's wettability to the sputtered surfaces.

We now discuss the behavior of galinstan on similar substrates. Unlike eGaIn, galinstan will stain, but not wet, thick foils of both indium and tin. However, galinstan will reactively wet to thin (20 μm) tin foil. It remains unclear as to why galinstan will reactively wet to a thin tin foil but not a thick tin foil, similarly to how eGaIn will reactively wet a thick tin foil but not a thin tin foil. However, an in-depth study of the molecular reactions and surface energies in these cases is beyond the scope of this work, and it can be induced that both material composition and texture of the substrate play a large role in the wettability of gallium-indium alloys.

The important result in this study is the long-term state of galinstan after reactive wetting on a thin tin foil substrate: in this case, over a long period of time ($\sim$days), the materials react together to become a single eutectic liquid metal, as seen in Figure 6.8. This denotes that a stable alloy of a new composition is developed. The new alloy was analyzed using elemental mapping in a scanning electron microscope over five samples, with the average composition (percentage by weight) being 57.63% $\pm$0.24%

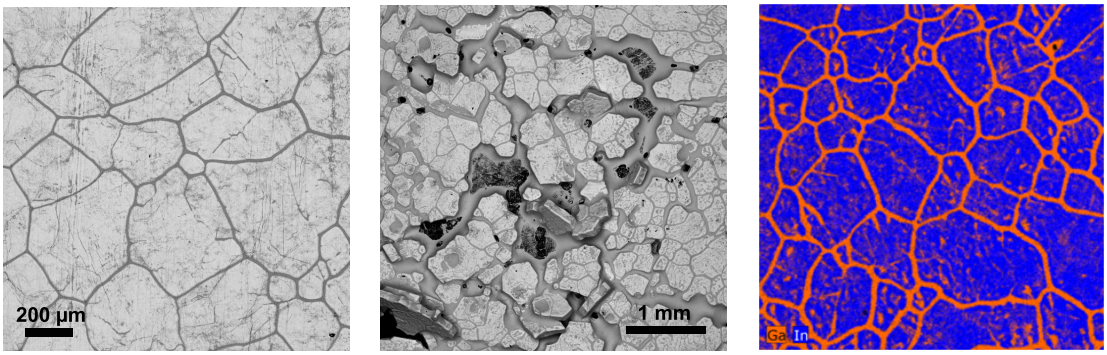

(a) (b) (c)

Figure 6.7: Indium foil (100 μm thick) that has been wetted by eutectic gallium-indium. The alloy diffuses through the indium foil at the grain boundaries. Grain size for this foil appears to be on the order of 100's of microns. (a) An SEM image of the indium grains diffused by gallium-indium alloy. (b) An SEM image similar to (a), but with some manual disturbance with forceps. After diffusing the foil, the gallium-indium alloy disperses underneath the indium grains. (d) An elemental map, confirming that the grains are indium chunks, and the alloy is resting in the grain boundaries (eGaIn is 75% gallium).

gallium, 22.69% ±0.09% indium, and 19.68% ±0.20% tin. This increased percentage of tin is consistent with the assumption that the underlying tin foil is absorbed into the initial alloy to create this new composition. As the system self-removes any rigid component, this combination of materials is ideal for the application of liquid-embedded-elastomer devices and was therefore chosen for the fabrication process.

Table 6.2 provides a summary of the characteristic contact angle between eutectic liquid metals and various surfaces tested in this study. Contact angle values were obtained through experiments on an Attension Theta Lite instrument and image analysis with Attension software set to 'polynomial' mode. For each solid−liquid combination the experiment was repeated at least three times, and contact angles were evaluated for at least 50 images per experiment. For dynamic experiments, contact angle was analyzed as a function of time.

Table 6.2: Summary of Characteristic Contact Angles between Eutectic Liquid Metals and Various Surfaces.
* No wetting, substrate repels the liquid material.
** The liquid material 'stains' the substrate, but does not wet.
† Results in "constitutional liquation".

	Contact Angle	
	eGaIn	**Galinstan**
Sputtered (In/Sn) for 2 minutes on Silicon	CA $> 160\,^{\circ}_{*}$	
Sputtered (In/Sn) for 10 minutes on Silicon	CA $> 160\,^{\circ}_{*}$	
Sputtered (In/Sn) for 2 minutes on (In/Sn) Foil	CA $> 160\,^{\circ}_{*}$	
PDMS	CA $\approx 130\,^{\circ}_{**}$	
Oxygen Plasma-Treated PDMS	CA $\approx 125\,^{\circ}_{**}$	
100 μm thick Indium Foil	Inert Wetting, CA $< 10\,^{\circ}_{\dagger}$	CA $\approx 145\,^{\circ}_{**}$
127 μm thick Tin Foil	Reactive Wetting, CA $< 10\,^{\circ}_{\dagger}$	CA $\approx 135\,^{\circ}_{**}$
20 μm thick Tin Foil	CA $\approx 135\,^{\circ}_{**}$	Reactive Wetting, CA $< 10\,^{\circ}$

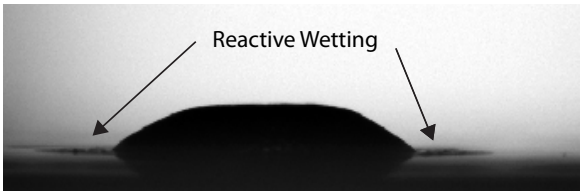

Figure 6.8: (a) Liquid galinstan that has been in contact with a Tin foil surface (20 μm thick) for over 4 days. Reactive wetting can be inferred not only by the slow spreading of the liquid on the surface, but also the signature of the surface material changes occurring around the perimeter of the droplet.

6.4 Lithography-Based Deposition Results

The results of the interfacial process experiments with gallium-indium alloys were employed in a fabrication process that exploits the wetting, or non-wetting, properties between the alloys and surfaces of various composition and texture. Figure 6.9 displays a test pattern used to demonstrate the possible trace widths and feature densities of the fabrication process. The test pattern included traces with widths of 1 mm, 500 μm, 200 μm, 100 μm, 50 μm, 25 μm, and 10 μm. Square features were spaced with edge-to-edge separations of the same dimensions listed above. As seen in Figure 6.9, the minimum trace width that the fabrication process produced is 200 μm. Upon further inspection, it is also apparent that the trace patterned to be 200 μm in width is only about half that width in actuality, with the conductive liquid forming a trace that is approximately 100 μm in width. This discrepancy between intended trace width and actual trace width is due to the aggressive ferric chloride etch, which likely over-etched the smaller traces and completely removed the traces less than 200 μm in width. Hence, the seed layer for the gallium-indium alloy was altered prior to the liquid deposition on the surface.

Figure 6.9 also demonstrates the ability to pattern densely-packed features with

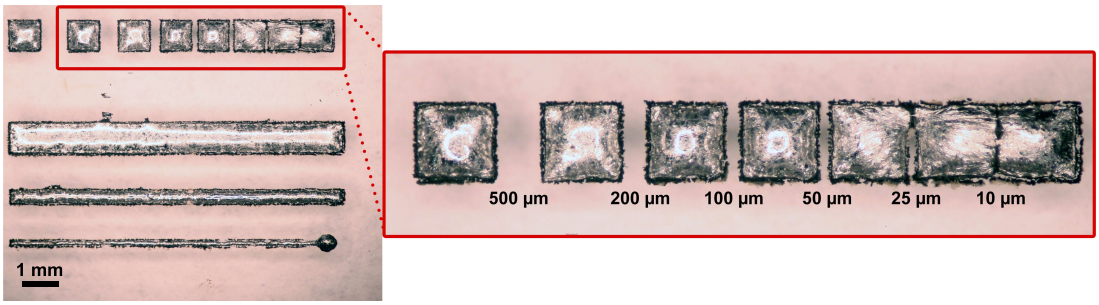

Figure 6.9: A liquid-embedded-elastomer, wherein the elastomer is embedded with a test pattern, displaying possible feature sizes and densities given by the proposed fabrication process.

the proposed liquid-embedded-elastomer fabrication process. Isolated features (squares with a feature length of 1 mm in this case) are shown to be reliably patterned with an edge-to-edge separation as small as 25 μm.

Figure 6.10(c) shows the cross-sectional area of both a 1 mm wide conductive liquid trace and a 1 mm^2 square conductive liquid feature embedded in an elastomer sheet. The cross-section of these features was found using a 3D laser confocal microscope (Olympus, LEXT OLS4000), and is seen to be rounded in shape. Color maps denoting the 3D cross-section for the 1 mm trace and the 1 mm^2 square are shown in Figure 6.10(a-b). The peak heights of the 1 mm channel and 1 mm^2 square are approximately 100 μm and 85 μm, respectively.

Future investigations will include further experimental fabrication techniques to continue to reduce the minimum trace width and increase feature densities. For example, gaining more control over the trace and feature heights may inherently allow for smaller edge-to-edge separation. A different approach to deposition and patterning of the seed layer may allow for smaller trace widths. Increased control over the cross-sectional area of liquid features may allow for thinner devices (the

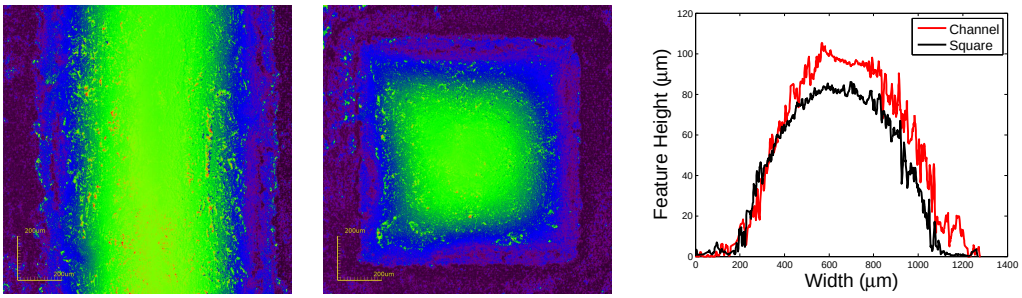

(a) (b) (c)

Figure 6.10: Color maps of the shape of (a) a 1 mm wide conductive liquid trace and (b) a 1 mm^2 square conductive liquid feature embedded in an elastomer sheet. (c) The cross-sectional area of both the 1 mm channel and the 1 mm^2 square. The peak heights of the 1 mm channel and 1 mm^2 square are approximately 100 μm and 85 μm, respectively.

elastomer sheet shown in Figure 6.9 is approximately 300 μm thick with the features between 85 - 100 μm in height). Further optimization of the process will allow for innovation in new hyperelastic electrical devices, and perhaps multi-layer devices.

6.5 Conclusion

In this chapter, we present a new process that allows for manufacturing of liquid-embedded-elastomer devices in a reliable and printable approach. This fabrication technique yields the ability to pattern highly conductive liquid metals within elastomer films without the need for molding, bonding, or manual steps. This process incorporates techniques from printed circuit board manufacturing and photolithography, as well as exploits wetting properties and phase change of conductive liquid metal. Ultimately, liquid-embedded elastomer devices with features smaller than 200 μm and edge-to-edge separations as small as 25 μm are produced.

Chapter 7

Conclusions and Future Work

Soft materials can be made active in that they can greatly change shape, volume or property in response to diverse stimuli, requiring innovations in design, materials, and fabrication methods. This work describes several approaches to soft robotic components using soft active materials. While Chapter 2 introduces a humidity-triggered hydrogel unimorph as one possible design for soft actuation, the majority of this thesis explores liquid-embedded elastomers and their application to pressure sensing, curvature and angle sensing, power electronics, and integrated circuits.

An elastomer sheet with embedded microchannels filled with conductive liquid may be responsive to various mechanical stimuli, such as strain, pressure, and curvature. Applying these mechanical stimuli to the elastomer will deform the cross-section of the embedded microchannels, hence changing the electrical resistance across the channels. In this thesis, designs for strain, pressure and curvature sensors have been described, wherein the change in electrical resistance across microchannels is mapped to the elastic deformations. Predictive analytical solutions have been discussed, which

may be employed to adjust the sensitivity, functional range, and resolution of the sensors.

Several demonstrative devices have been fabricated, such as a hyperelastic tactile keypad (Chapter 3), a soft tactile sensor array for sub-millimeter contact localization and contact force measurement in micro-manipulation (Chapter 3), and curvature sensors for joint angle proprioception (Chapter 4). Liquid-embedded elastomers are also considered for applications in stretchable power electronics (Chapter 5). Future efforts may be focused on further integration of hyperelastic pressure sensors with soft robotics, artificial skin, soft orthotics, integrated circuitry, and shape-mapping elastomer sheets.

The principles and fabrication techniques presented here may also be used to explore other potential sensing modes and electronic functions. In Chapter 6, a new fabrication process was discussed, which allows for manufacturing of liquid-embedded-elastomer devices in a reliable and printable approach. The process incorporates techniques from printed circuit board manufacturing and photolithography, as well as exploits wetting properties and phase change of gallium-indium alloys, to fabricate conductive liquid traces smaller than 200 μm in width and with edge-to-edge separations as small as 25 μm.

It is expected that further optimization of the manufacturing process will yield the ability to create much smaller and densely packed features, and will be used to create novel devices such as soft resistors, inductors, capacitors, and active (gated) electronic components. New soft devices enabled by this process may include capacitive sensors, electromagnets (and magnetic valves), and liquid transistors. Future manufacturing

processes may allow for 3D liquid-embedded elastomer structures, which could translate to more sophisticated integration of sensory skins with surgical devices, such as endoscopy and neuro-endoscopy tools.

Bibliography

[1] James B. Wood. "octopus escapes through a 1 in hole." online video clip. youtube. url: http://www.youtube.com, July 2010.

[2] F. Ilievski, A.D. Mazzeo, R.F. Shepherd, X. Chen, and G.M. Whitesides. Soft robotics for chemists. *Angewandte Chemie*, 123(8):1930–1935, 2011.

[3] R.F. Shepherd, F. Ilievski, W. Choi, S.A. Morin, A.A. Stokes, A.D. Mazzeo, X. Chen, M. Wang, and G.M. Whitesides. Multigait soft robot. *Proceedings of the National Academy of Sciences*, 108(51):20400–20403, 2011.

[4] H.T. Lin, G.G. Leisk, and B. Trimmer. Goqbot: a caterpillar-inspired soft-bodied rolling robot. *Bioinspiration & Biomimetics*, 6:026007, 2011.

[5] P. Walters and D. McGoran. Digital fabrication of smart structures and mechanism: Creative applications in art and design. *Proc. of International Conference on Digital Printing Technologies and Digital Fabrication 2011*, 27:185–188, 2011.

[6] R. Pelrine, R. Kornbluh, Q. Pei, S. Stanford, S. Oh, J. Eckerle, and K. Meijer. Dielectric elastomer artificial muscle actuators: Toward biomimetic motion. In *Proc. SPIE*, volume 4695, pages 126–137, 2002.

[7] A. Mozeika, E. Steltz, and H.M. Jaeger. The first steps of a robot based on jamming skin enabled locomotion. In *Intelligent Robots and Systems, 2009. IROS 2009. IEEE/RSJ International Conference on*, pages 408–409. IEEE, 2009.

[8] Y. Bar-Cohen. *Electroactive polymer (EAP) actuators as artificial muscles: reality, potential, and challenges*. Society of Photo Optical, 2004.

[9] P.G.A. Madden, J.D.W. Madden, P.A. Anquetil, N.A. Vandesteeg, and I.W. Hunter. The relation of conducting polymer actuator material properties to performance. *Oceanic Engineering, IEEE Journal of*, 29(3):696–705, 2004.

[10] Y. Osada, H. Okuzaki, and H. Hori. A polymer gel with electrically driven motility. *Nature*, 355:242–244, 1992.

[11] K. Takei, T. Takahashi, J.C. Ho, H. Ko, A.G. Gillies, P.W. Leu, R.S. Fearing, and A. Javey. Nanowire active-matrix circuitry for low-voltage macroscale artificial skin. *Nature materials*, 9(10):821–826, 2010.

[12] M. Inaba, Y. Hoshino, K. Nagasaka, T. Ninomiya, S. Kagami, and H. Inoue. A full-body tactile sensor suit using electrically conductive fabric and strings. In *Intelligent Robots and Systems' 96, IROS 96, Proceedings of the 1996 IEEE/RSJ International Conference on*, volume 2, pages 450–457. IEEE, 1996.

[13] M.A. Lacasse, V. Duchaine, and C. Gosselin. Characterization of the electrical resistance of carbon-black-filled silicone: Application to a flexible and stretchable robot skin. In *Robotics and Automation (ICRA), 2010 IEEE International Conference on*, pages 4842–4848. IEEE, 2010.

[14] J. A. Rogers and Y. Huang. A curvy, stretchy future for electronics. *Proc. Nat. Acad. Sci. U.S.A.*, 106(27):10875–10876, 2009.

[15] S.P. Lacour, D. Chan, S. Wagner, T. Li, and Z. Suo. Mechanisms of reversible stretchability of thin metal films on elastomeric substrates. *Applied Physics Letters*, 88:204103, 2006.

[16] W.T.S. Huck. Responsive polymers for nanoscale actuation. *Materials Today*, 11(7-8):24–32, 2008.

[17] A. Mozeika, E. Steltz, and H.M. Jaeger. The First Steps of a Robot Based on Jamming Skin Enabled Locomotion. In *Intelligent Robots and Systems, IROS 2009. IEEE/RSJ International Conference on*, pages 408–409. IEEE, 2009.

[18] O.C. Jeong and S. Konishi. All PDMS pneumatic microfinger with bidirectional motion and its application. *Microelectromechanical Systems, Journal of*, 15(4):896–903, 2006.

[19] S. Konishi, F. Kawai, and P. Cusin. Thin flexible end-effector using pneumatic balloon actuator. *Sensors & Actuators: A. Physical*, 89(1-2):28–35, 2001.

[20] Y. Osada and A. Matsuda. Shape memory in hydrogels. *Nature*, 376(6537):219, 1995.

[21] K. Otsuka and C.M. Wayman. *Shape memory materials*. Cambridge University Press, Cambridge, UK, 1999.

[22] T.F. Otero and J.M. Sansieña. Soft and wet conducting polymers for artificial muscles. *Advanced Materials*, 10(6):491–494, 1998.

[23] R Pelrine, R Kornbluh, and G Kofod. High-Strain Actuator Materials Based on Dielectric Elastomers. *Advanced Materials*, 12(16):1223, 2000.

[24] A. Sidorenko, T. Krupenkin, A. Taylor, P. Fratzl, and J. Aizenberg. Reversible switching of hydrogel-actuated nanostructures into complex micropatterns. *Science*, 315(5811):487, 2007.

[25] E.C. Cho, J.W. Kim, A. Fernández-Nieves, and D.A. Weitz. Highly responsive hydrogel scaffolds formed by three-dimensional organization of microgel nanoparticles. *Nano Lett*, 8(1):168–172, 2008.

[26] Z. Hu, X. Zhang, and Y. Li. Synthesis and application of modulated polymer gels. *Science*, 269(5223):525, 1995.

[27] A. Matsuda, J. Sato, H. Yasunaga, and Y. Osada. Order-disorder transition of a hydrogel containing an n-alkyl acrylate. *Macromolecules*, 27(26):7695–7698, 1994.

[28] B. Samel, P. Griss, and G. Stemme. A thermally responsive PDMS composite and its microfluidic applications. *Microelectromechanical Systems, Journal of*, 16(1):50–57, 2007.

[29] J. Wang, Z. Chen, M. Mauk, K.S. Hong, M. Li, S. Yang, and H.H. Bau. Self-actuated, thermo-responsive hydrogel valves for lab on a chip. *Biomedical Microdevices*, 7(4):313–322, 2005.

[30] A. Lendlein, H. Jiang, O. Junger, and R. Langer. Light-induced shape-memory polymers. *Nature*, 434(7035):879–882, 2005.

[31] A. Baldi, Y. Gu, PE Loftness, RA Siegel, and B. Ziaie. A hydrogel-actuated environmentally sensitive microvalve for active flow control. *Microelectromechanical Systems, Journal of*, 12(5):613–621, 2003.

[32] D.J. Beebe, J.S. Moore, J.M. Bauer, Q. Yu, R.H. Liu, C. Devadoss, and B.H. Jo. Functional hydrogel structures for autonomous flowcontrol inside microfluidic channels. *Nature*, 404:588–590, 2000.

[33] RH Liu, Q. Yu, and DJ Beebe. Fabrication and characterization of hydrogel-based microvalves. *Microelectromechanical Systems, Journal of*, 11(1):45–53, 2002.

[34] B. Zhao and J.S. Moore. Fast pH-and ionic strength-responsive hydrogels in microchannels. *Langmuir*, 17(16):4758–4763, 2001.

[35] M.J. Bassetti, A.N. Chatterjee, NR Aluru, and D.J. Beebe. Development and modeling of electrically triggered hydrogels for microfluidic applications. *Journal of Microelectromechanical Systems*, 14(5):1198, 2005.

[36] Z. Liu and P. Calvert. Multilayer hydrogels as muscle-like actuators. *Advanced Materials*, 12(4):288–291, 2000.

[37] D.T. Eddington and D.J. Beebe. A valved responsive hydrogel microdispensing device with integrated pressure source. *Journal of Microelectromechanical Systems*, 13(4), 2004.

[38] F. Chiellini, R. Bizzarri, C.K. Ober, D. Schmaljohann, T. Yu, R. Solaro, and E. Chiellini. Patterning of polymeric hydrogels for biomedical applications. *Macromolecular Rapid Communications*, 22(15):1284–1287, 2001.

[39] P. Kim, L.D. Zarzar, X. Zhao, A. Sidorenko, and J. Aizenberg. Polymer Microbristle in Gels: Toward All-Soft Reconfigurable Hybrid Surfaces. *Soft Matter*, 2009.

[40] K.W. Oh and C.H. Ahn. A review of microvalves. *Journal of Micromechanics and Microengineering*, 16(5):13, 2006.

[41] L. Dong, A.K. Agarwal, D.J. Beebe, and H. Jiang. Adaptive liquid microlenses activated by stimuli-responsive hydrogels. *Nature*, 442(7102):551, 2006.

[42] T. Tanaka, L.O. Hocker, and G.B. Benedek. Spectrum of light scattered from a viscoelastic gel. *The Journal of Chemical Physics*, 59:5151, 1973.

[43] A. Pelah and T.M. Jovin. Polymeric Actuators for Biological Applications. *ChemPhysChem*, 8(12):1757–1760, 2007.

[44] L.D. Landau and E.M. Lifshitz. *Theory of elasticity*. Addison-Wesley, 1959.

[45] S.P. Timoshenko and J.N. Goodier. *Theory of elasticity*. McGraw Hill, 1970.

[46] M.H. Sadd. *Elasticity: Theory, Applications, and Numerics*. Academic Press, 2009.

[47] T. Tanaka and D.J. Fillmore. Kinetics of swelling of gels. *The Journal of Chemical Physics*, 70:1214, 1979.

[48] Y. Li and T. Tanaka. Kinetics of swelling and shrinking of gels. *The Journal of Chemical Physics*, 92:1365, 1990.

[49] A. Onuki. Paradox in phase transitions with volume change. *Physical Review A*, 38(4):2192–2195, 1988.

[50] C. Wang, Y. Li, and Z. Hu. Swelling kinetics of polymer gels. *Macromolecules*, 30(16):4727–4732, 1997.

[51] A. Peters and SJ Candau. Kinetics of swelling of spherical and cylindrical gels. *Macromolecules*, 21(7):2278–2282, 1988.

[52] A. Onuki. Theory of pattern formation in gels: Surface folding in highly compressible elastic bodies. *Physical Review A*, 39(11):5932–5948, 1989.

[53] O. Tari and O. Pekcan. Swelling activation energy of k-carrageenan in its gel state: A fluorescence study. *Journal of Applied Polymer Science*, 106(6):4164–4168, 2007.

[54] E. Birgersson, H. Li, and S. Wu. Transient analysis of temperature-sensitive neutral hydrogels. *Journal of the Mechanics and Physics of Solids*, 56(2):444–466, 2008.

[55] V. Sharma, M. Dhayal, SM Shivaprasad, and SC Jain. Surface characterization of plasma-treated and PEG-grafted PDMS for micro fluidic applications. *Vacuum*, 81(9):1094–1100, 2007.

[56] M. Iza, G. Stoianovici, L. Viora, JL Grossiord, and G. Couarraze. Hydrogels of poly (ethylene glycol): mechanical characterization and release of a model drug. *Journal of Controlled Release*, 52(1-2):41–51, 1998.

[57] J.N. Lee, C. Park, and G.M. Whitesides. Solvent compatibility of poly (dimethylsiloxane)-based microfluidic devices. *Analytical Chemistry (ACS Publications)*, 75(23):6544–6554, 2003.

[58] J. Bunsow, J. Petri, and D. Johannsmann. Preparation of Hydrogel-Silica Composite Films by Electrochemically Triggered Deposition. *Advanced Functional Materials*, 18:23, 2009.

[59] M. Mohammed, J. Major, Z. Zhang, D. Faghri, D. Meyer, and A. Fadl. PDMS Surface Modification for Applications on Thermally Responsive Hydrogel Microvalves. *Proceedings of the Fifth International Conference on Nanochannels, Microchannels and Minichannels*, 2007.

[60] PJ Flory and J Rehner. Statistical Mechanics of Cross-Linked Polymer Networks II. Swelling. *Journal of Chemical Physics*, 11:512, 1943.

[61] J. Zhang, X. Zhao, Z. Suo, and H. Jiang. A finite element method for transient analysis of concurrent large deformation and mass transport in gels. *Journal of Applied Physics*, 105:093522, 2009.

[62] D. Marculescu, R. Marculescu, N. H. Zamora, P. Stanley-Marbell, P. K. Khosla, S. Park, S. Jayaraman, S. Jung, C. Lauterbach, W. Weber, T. Kirstein, D. Cottet, J. Grzyb, G. Troster, M. Jones, T. Martin, and Z. Nakad. Electronic textiles: A platform for pervasive computing. *Proc. IEEE*, 91(12):1995–2018, 2003.

[63] D.H. Kim, Y.S. Kim, J. Wu, Z. Liu, J. Song, H.S. Kim, Y.Y. Huang, K.C. Hwang, and J.A. Rogers. Ultrathin Silicon Circuits With Strain-Isolation Layers and Mesh Layouts for High-Performance Electronics on Fabric, Vinyl, Leather, and Paper. *Advanced Materials*, 21(36):3703–3707, 2009.

[64] T. Hoshi and H. Shinoda. Robot skin based on touch-area-sensitive tactile element. In *Proc. IEEE International Conference on Robotics and Automation (ICRA '06)*, pages 3463–3468, Orlando, Florida, May 2006.

[65] H. Chigusa, Y. Makino, and H. Shinoda. Large area sensor skin based on two-dimensional signal transmission technology. In *Proc. IEEE EuroHaptics Conference and Symposium on Haptic Interfaces for Virtual Environment and Teleoperator Systems (WHC '07)*, pages 151–156, Tsukaba, Japan, March 2007.

[66] T. Yoshikai, H. Fukushima, M. Hayashi, and M. Inaba. Development of soft stretchable knit sensor for humanoids' whole-body tactile sensibility. In *Proc. IEEE-RAS International Conference on Humanoid Robots (ICHR '09)*, pages 624–631, Paris, France, December 2009.

[67] D. Cotton, I. M. Graz, and S. P. Lacour. A multifunctional capacitive sensor for stretchable electronic skins. *IEEE Sensors Journal*, 9(12):2008–2009, 2009.

[68] Y. Tada, M. Inoue, T. Kawasaki, Y. Kawahito, H. Ishiguro, and K. Suganuma. A flexible and stretchable tactile sensor utilizing static electricity. In *Proc. IEEE/RSJ International Conference on Intelligent Robots and Systems (IROS '07)*, pages 684–689, San Diego, California, October 2007.

[69] H. Alirezaei, A. Nagakubo, and Y. Kuniyoshi. A highly stretchable tactile distribution sensor for smooth surfaced humanoids. In *Proc. IEEE-RAS International Conference on Humanoid Robots (ICHR '07)*, pages 167–173, Pittsburgh, Pennsylvania, November 2007.

[70] L. Ventrelli, L. Beccai, V. Mattoli, A. Menciassi, and P. Dario. Development of a stretchable skin-like tactile sensor based on polymeric composites. In *Proc. IEEE International Conference on Robotics and Biomimetics (ROBIO '09)*, pages 123–128, Guilin, China, December 2009.

[71] M.-A. Lacasse, V. Duchaine, and C. Gosselin. Characterization of the electrical resistance of carbon-black-filled silicone: Application to a flexible and

stretchable robot skin. In *Proc. IEEE International Conference on Robotics and Automation (ICRA '10)*, pages 4842–4848, Anchorage, Alaska, May 2010.

[72] K. Noda, E. Iwase, K. Matsumoto, and I. Shimoyama. Stretchable liquid tactile sensor for robot-joints. In *Robotics and Automation (ICRA), 2010 IEEE International Conference on*, pages 4212–4217. IEEE, 2010.

[73] D.-Y. Khang, H. Jiang, Y. Huang, and J. A. Rogers. A stretchable form of single-crystal silicon for high-performance electronics on rubber substrates. *Science*, 311:208–212, 2006.

[74] D.-H. Kim, J.-H. Ahn, W. M. Choi, Kim H.-S., T.-H. Kim, J. Song, Y. Y. Huang, Z. Liu, C. Lu, and J. A. Rogers. Stretchable and foldable silicon integrated circuits. *Science*, 320:507–511, 2008.

[75] Y. Sun, W.M. Choi, H. Jiang, Y.Y. Huang, and J.A. Rogers. Controlled buckling of semiconductor nanoribbons for stretchable electronics. *Nature nanotechnology*, 1(3):201–207, 2006.

[76] D.H. Kim, J. Song, W.M. Choi, H.S. Kim, R.H. Kim, Z. Liu, Y.Y. Huang, K.C. Hwang, Y. Zhang, and J.A. Rogers. Materials and noncoplanar mesh designs for integrated circuits with linear elastic responses to extreme mechanical deformations. *Proceedings of the National Academy of Sciences*, 105(48):18675, 2008.

[77] S.P. Lacour, S. Wagner, Z. Huang, and Z. Suo. Stretchable gold conductors on elastomeric substrates. *Applied physics letters*, 82:2404, 2003.

[78] S.P. Lacour, J. Jones, S. Wagner, T. Li, and Z. Suo. Stretchable interconnects for elastic electronic surfaces. *Proceedings of the IEEE*, 93(8):1459–1467, 2005.

[79] K.S. Kim, Y. Zhao, H. Jang, S.Y. Lee, J.M. Kim, K.S. Kim, J.H. Ahn, P. Kim, J.Y. Choi, and B.H. Hong. Large-scale pattern growth of graphene films for stretchable transparent electrodes. *Nature*, 457(7230):706–710, 2009.

[80] T. Sekitani, H. Nakajima, H. Maeda, T. Fukushima, T. Aida, K. Hata, and T. Someya. Stretchable active-matrix organic light-emitting diode display using printable elastic conductors. *Nature Materials*, 8(6):494–499, 2009.

[81] J.H. So, J. Thelen, A. Qusba, G.J. Hayes, G. Lazzi, and M.D. Dickey. Reversibly deformable and mechanically tunable fluidic antennas. *Advanced Functional Materials*, 19(22):3632–3637, 2009.

[82] H.J. Kim, C. Son, and B. Ziaie. A multiaxial stretchable interconnect using liquid-alloy-filled elastomeric microchannels. *Applied Physics Letters*, 92(1):011904–011904, 2008.

[83] R. J. Whitney. The measurement of changes in human limb-volume by means of a mercury-in-rubber strain gauge. *Proc. Physiological Soc.*, 109:5–6, 1949.

[84] L. U. Rastrelli, E. L. Anderson, and J. D. Michie. Elastomeric strain gauge. *U.S. Patent*, 3,304,528, 1967.

[85] M.D. Dickey, R.C. Chiechi, R.J. Larsen, E.A. Weiss, D.A. Weitz, and G.M. Whitesides. Eutectic gallium-indium (egain): A liquid metal alloy for the formation of stable structures in microchannels at room temperature. *Advanced Functional Materials*, 18(7):1097–1104, 2008.

[86] A. Pique, D. B. Chrisey, J. M. Fitz-Gerald, R. A. McGill, R. C. Y. Auyeung, H. D. Wu, S. Lakeou, V. Nguyen, R. Chung, and M. Duignan. Direct writing of electronic and sensor materials using a laser transfer techniqu. *J. Mter. Res.*, 15:1872–1875, 1967.

[87] R. Menon, A. Patel, D. Gil, and H. I. Smith. Maskless lithography. *Materials Today*, 8(2):26–33, 2005.

[88] Y. Xia and G. M. Whitesides. Soft lithography. *Annu. Rev. Mater. Sci.*, 28:153–184, 1998.

[89] D. C. Duffy, J. C. McDonald, O. J. A. Schueller, and G. M. Whitesides. Rapid prototyping of microfluidic systems in poly(dimethylsiloxane). *Anal. Chem.*, 70(23):4974–4984, 1998.

[90] H. Tada, P. C. Paris, and G. R. Irwin. *The Stress Analysis of Cracks Handbook*. ASME Press, New York, USA, 3 edition, 2000.

[91] Y.L. Park, C. Majidi, R. Kramer, P. Bérard, and R.J. Wood. Hyperelastic pressure sensing with a liquid-embedded elastomer. *Journal of Micromechanics and Microengineering*, 20:125029, 2010.

[92] T. Starner. Human-powered wearable computing. *IBM systems Journal*, 35(3):618–629, 1996.

[93] Y. Xia, J.A. Rogers, K.E. Paul, G.M. Whitesides, et al. Unconventional methods for fabricating and patterning nanostructures. *Chemical Reviews-Columbus*, 99(7):1823–1848, 1999.

[94] S.R. Quake and A. Scherer. From micro-to nanofabrication with soft materials. *Science*, 290(5496):1536, 2000.

[95] S. Cheng and Z. Wu. A microfluidic, reversibly stretchable, large-area wireless strain sensor. *Advanced Functional Materials*, 2011.

[96] S. Cheng and Z. Wu. Microfluidic stretchable rf electronics. *Lab Chip*, 10(23):3227–3234, 2010.

[97] C. Majidi, R. Kramer, and R. J. Wood. Non-Differential Elastomer Curvature Sensor for Softer-than-Skin Electronics. *Smart Materials & Structures (under review)*, 2011.

[98] E. Jesperson and M.R. Neuman. A thin film strain gauge angular displacement sensor for measuring finger joint angles. In *Engineering in Medicine and Biology Society, 1988. Proceedings of the Annual International Conference of the IEEE*, pages 807–vol. IEEE, 2006.

[99] G. Brasseur. A capacitive finger-type angular-position and angular-speed sensor. In *Instrumentation and Measurement Technology Conference, 1998. IMTC/98. Conference Proceedings. IEEE*, volume 2, pages 967–972. IEEE, 1998.

[100] Y. Liu, L. Zhang, JAR Williams, and I. Bennion. Long-period fibre grating bend sensor based on measurement of resonance mode splitting. In *Lasers and Electro-Optics, 2000.(CLEO 2000). Conference on*, pages 306–307. IEEE, 2000.

[101] BAL Gwandu, XW Shu, Y. Liu, W. Zhang, L. Zhang, and I. Bennion. Simultaneous measurement of strain and curvature using superstructure fibre Bragg gratings. *Sensors and Actuators A: Physical*, 96(2-3):133–139, 2002.

[102] Y.P. Wang and Y.J. Rao. A novel long period fiber grating sensor measuring curvature and determining bend-direction simultaneously. *Sensors Journal, IEEE*, 5(5):839–843, 2005.

[103] L.Y. Shao, L. Xiong, C. Chen, A. Laronche, and J. Albert. Directional Bend Sensor Based on Re-Grown Tilted Fiber Bragg Grating. *Lightwave Technology, Journal of*, 28(18):2681–2687, 2010.

[104] T.D. Allsop, M. Dubov, A. Martinez, F. Floreani, I. Khrushchev, D.J. Webb, and I. Bennion. Directional bend sensor based on an asymmetric modification of the fiber cladding by femtosecond laser. In *Conference on Lasers and Electro-Optics*. Optical Society of America, 2005.

[105] G.T. Kanellos, G. Papaioannou, D. Tsiokos, C. Mitrogiannis, G. Nianios, and N. Pleros. Two dimensional polymer-embedded quasi-distributed FBG pressure sensor for biomedical applications. *Opt. Express*, 18:179–186, 2010.

[106] X. Chen, C. Zhang, D.J. Webb, K. Kalli, and G.D. Peng. Highly Sensitive Bend Sensor Based on Bragg Grating in Eccentric Core Polymer Fiber. *Photonics Technology Letters, IEEE*, 22(11):850–852, 2010.

[107] HJ Patrick. Self-aligning bipolar bend transducer based on long period grating written in eccentric core fibre. *Electronics Letters*, 36(21):1763–1764, 2000.

[108] CC Ye, SW James, and RP Tatam. Simultaneous temperature and bend sensing with long-period fiber gratings. *Optics Letters*, 25(14):1007–1009, 2000.

[109] D. Zhao, K. Zhou, X. Chen, L. Zhang, I. Bennion, G. Flockhart, W.N. MacPherson, J.S. Barton, and J.D.C. Jones. Implementation of vectorial bend sensors using long-period gratings UV-inscribed in special shape fibres. *Measurement Science and Technology*, 15:1647, 2004.

[110] L. Dipietro, A.M. Sabatini, and P. Dario. A survey of glove-based systems and their applications. *Systems, Man, and Cybernetics, Part C: Applications and Reviews, IEEE Transactions on*, 38(4):461–482, 2008.

[111] ME Vlachopoulou, A. Tserepi, P. Pavli, P. Argitis, M. Sanopoulou, and K. Misiakos. A low temperature surface modification assisted method for bonding plastic substrates. *Journal of Micromechanics and Microengineering*, 19:015007, 2009.

[112] L. Tang and N.Y. Lee. A facile route for irreversible bonding of plastic-PDMS hybrid microdevices at room temperature. *Lab Chip*, 10(10):1274–1280, 2010.

[113] J.K. Paik, E. Hawkes, and R.J. Wood. A novel low-profile shape memory alloy torsional actuator. *Smart Materials and Structures*, 19:125014, 2010.

[114] J.A. Rogers and Y. Huang. A curvy, stretchy future for electronics. *Proceedings of the National Academy of Sciences*, 106(27):10875–10876, 2009.

[115] D.H. Kim and J.A. Rogers. Stretchable electronics: Materials strategies and devices. *Advanced Materials*, 20(24):4887–4892, 2008.

[116] Z. Fan, J.C. Ho, T. Takahashi, R. Yerushalmi, K. Takei, A.C. Ford, Y.L. Chueh, and A. Javey. Toward the development of printable nanowire electronics and sensors. *Advanced Materials*, 21(37):3730–3743, 2009.

[117] SRC Vivekchand, K.C. Kam, G. Gundiah, A. Govindaraj, AK Cheetham, and CNR Rao. Electrical properties of inorganic nanowire–polymer composites. *J. Mater. Chem.*, 15(46):4922–4927, 2005.

[118] Texas Instruments. "the chip that jack built." url: http://www.ti.com/corp/docs/kilbyctr/jackbuilt.shtml, 2012.

[119] K.E. Bean. Anisotropic etching of silicon. *Electron Devices, IEEE Transactions on*, 25(10):1185–1193, 1978.

[120] K.E. Petersen. Silicon as a mechanical material. *Proceedings of the IEEE*, 70(5):420–457, 1982.

[121] J.M. Bustillo, R.T. Howe, and R.S. Muller. Surface micromachining for microelectromechanical systems. *Proceedings of the IEEE*, 86(8):1552–1574, 1998.

[122] L.S. Fan, Y.C. Tai, and R.S. Muller. Integrated movable micromechanical structures for sensors and actuators. *Electron Devices, IEEE Transactions on*, 35(6):724–730, 1988.

[123] G.M. Whitesides. The origins and the future of microfluidics. *Nature*, 442(7101):368–373, 2006.

[124] C. Liu. Recent developments in polymer mems. *Advanced Materials*, 19(22):3783–3790, 2007.

[125] Ken Gilleo. *Handbook of Flexible Circuits*. Springer, 1998.

[126] PCB Design and Fab. "pcb design guidelines". url: http://www.pcbdesignandfab.com/guidelines.htm.

[127] J.A. Rogers, T. Someya, and Y. Huang. Materials and mechanics for stretchable electronics. *Science*, 327(5973):1603, 2010.

[128] B. Huyghe, H. Rogier, J. Vanfleteren, and F. Axisa. Design and manufacturing of stretchable high-frequency interconnects. *Advanced Packaging, IEEE Transactions on*, 31(4):802–808, 2008.

[129] M.A. Eddings, M.A. Johnson, and B.K. Gale. Determining the optimal pdms–pdms bonding technique for microfluidic devices. *Journal of Micromechanics and Microengineering*, 18:067001, 2008.

[130] S. Corbett, J. Strole, K. Johnston, E.J. Swenson, and W. Lu. Laser direct exposure of photodefinable polymer masks using shaped-beam optics. *Electronics Packaging Manufacturing, IEEE Transactions on*, 28(4):312–321, 2005.

[131] C. Karcher, V. Kocourek, and D. Schulze. Experimental investigations of electromagnetic instabilities of free surfaces in a liquid metal drop. *Proceedings of Cerca con Google*, 2003.

[132] R.C. Chiechi, E.A. Weiss, M.D. Dickey, and G.M. Whitesides. Eutectic gallium–indium (egain): A moldable liquid metal for electrical characterization of self-assembled monolayers. *Angewandte Chemie*, 120(1):148–150, 2008.

[133] L. Mishchenko, B. Hatton, V. Bahadur, J.A. Taylor, T. Krupenkin, and J. Aizenberg. Design of ice-free nanostructured surfaces based on repulsion of impacting water droplets. *ACS nano*, 2010.